Characteristics of Buoyancy Driven Natural Ventilation through Horizontal Openings

PhD Thesis definded public at Aalborg University (101106)

Li, Zhigang

Publication date:
2007

Document Version
Publisher's PDF, also known as Version of record

Characteristics of Buoyancy Driven Natural Ventilation through Horizontal Openings

PhD Thesis
Defended public at Aalborg University
(101106)

Zhigang Li

ISSN 1901-7294
DCE Thesis No. 008

AALBORG UNIVERSITY
Department of Civil Engineering

Aalborg University
Department of Civil Engineering
Architectural Engineering

DCE Thesis No. 008

Characteristics of Buoyancy Driven Natural Ventilation through Horizontal Openings

PhD Thesis definded public at Aalborg University (101106)

by

Zhigang Li

August 2007

Preface

This thesis is submitted in accordance with the conditions for obtaining the Danish Ph.D. degree.

This thesis represents the end of my Ph.D. study at Aalborg University, Department of Civil Engineering with Professor Per Heiselberg and Professor Peter V. Nielsen as supervisors.

I wish to express my gratitude to Professor Per Heiselberg and Professor Peter V. Nielsen for their guidance and support, and for giving me the opportunity to fulfil this work.

My thanks also extend to Carl Erik Hyldgård and Torben Christensen for assistance in the laboratory. I would also like to express my thanks to all colleagues and members for their valuable assistance during the study.

Finally, I want to thank my family for their patience and support.

Zhigang Li

September 2006

Abstract

Air flow through horizontal openings is an important issue of mass and energy transfer between different zones in buildings. This kind of mass and energy transfer have important implications regarding energy saving, thermal comfort, control of contaminants, micro-organisms and spread of fire and smoke. Air flow through vertical openings has been widely investigated but little is known about the flow in the horizontal openings, especially when they are driven by buoyancy. A literature survey shows that the brine-water system and the scale model are normally used for the research work of air flow through horizontal openings.

Two cases of full-scale measurements of buoyancy driven natural ventilation through horizontal openings are performed: one horizontal opening and one horizontal opening combined with one vertical opening. For the case of one horizontal opening, the measurements are made for opening ratios *L/D* range from 0.027 to 4.455. The basic nature of air flow through the openings, including air flow rate, air velocity, temperature difference between the rooms and the dimensions of the horizontal openings, are measured. Smoke visualizations show that the air flow patterns are highly transient, unstable and complex, and the air flow rates oscillate with time. Correlations between the Froude number *Fr* and the opening ratio *L/D* are obtained, which is reasonable agreement with Epstein's formula derived from brine-water measurements, but the obtained *Fr* values show considerable deviations for a range of *L/D* ratios. Thus, the developed formulas are established. Meanwhile, the correlation between the Archimedes number *Ar* and the opening ratio $L/\sqrt{A}$ are also determined.

For the case of one horizontal opening combined one vertical opening, the measurements are made for opening ratios A_T/A_B in the range from 0.11 to 25. The smoke visualizations show that three flow modes can be identified depending on the different A_T/A_B value: bidirectional flow through the bottom opening, unidirectional flow through the two openings and bidirectional flow through the top opening. The bidirectional flow through the horizontal opening shows that the flow patterns are highly transient and unstable. A new empirical model for calculation of the air flow rate is developed by introducing a new opening area ratio factor.

Computational fluid dynamics (CFD) are used to study these two air flow cases. The air flow rate and air flow pattern are predicted and compared with the full-scale

measurements. The measurement data are used to compare two CFD models: standard k- ε model and large eddy simulation (LES) model. The cases calculated by the LES model agree well with the measured data, however, the cases simulated by the k-ε model are inaccurate compared to the measured data. For the highly transient and unstable flow, the LES model is a suitable tool to predict detailed and accurate air flow.

This work is important and quite useful in relation to natural ventilation systems. The measurement results can be used in both simple calculation tools to give a rough estimate of the capacity for design of a ventilation system, but also be implemented in more detailed models, especially multi-zone models, for simulation of the performance of natural ventilation systems.

Contents

Nomenclature

Symbol

A	Area [m^2]
Ar	Archimedes number
B	Buoyancy parameter
C	Concentration [ppm]
C_d	Discharge coefficient
C_P	Pressure coefficient
D	Diameter of the opening [m]
Fr	Froude number
g	Gravitational acceleration [m/s^2]
Gr	Grashof number
H	Height [m]
k	Turbulent kinetic energy [J/kg]
L	Length (height) of horizontal opening [m]
Nu	Nusselt number
P	Pressure [Pa]
Pr	Prandtl number
q	Volume flow rate [m^3/s]
Ra	Rayleigh number
Re	Reynolds number
S	Side length of opening [m]
t	Time [s]
T	Temperature [K]
v	Velocity [m/s]

Greek letters

α	Thermal diffusivity [m^2/s]
β	Thermal expansion coefficient [1/K]
ρ	Density [kg/m^3]
Δ	Difference
ε	Rate of dissipation of turbulent kinetic energy [J/kgs]
μ_t	Turbulent viscosity [kg/ms]

Subscripts

0	Reference level or neutral plane
B	Bottom
C	Critical
i	Internal
l	Lower
t	Temperature
T	Top
u	External or upper
w	Wind

1 Introduction

1.1 Natural ventilation

Ventilation is the process by which clean air is intentionally provided to a space and stale air is removed. It is essential for meeting the metabolic needs of occupants and for diluting and removing pollutants emitted by indoor sources, such as human bioeffluents, building materials, furnishings and even ventilation plants. The mainly produced contamination includes tobacco smoke, formaldehyde, volatile organic compounds (VOCs), radon, ozone and aerosols. In addition, odours, carbon dioxide and moisture also have significant effects on indoor air quality. In today's technological society, people spend more than 90% of their time in an indoor environment (i.e. room, office, factory, transport vehicles, recreational buildings, etc.) [1]. Therefore, they have become more aware of the effect of the indoor environment on health as a result of media publicity surrounding building related sickness (BRS) and the sick building syndrome (SBS). Thus, ventilation has become an essential role in the building design processes as building occupants expect good standards of indoor air quality and thermal comfort.

The purpose of a ventilation system is to provide acceptable microclimate in the space being ventilated. The thermal environment and air quality must be considered in the design of a ventilation system for a room or a building, which are fundamental to the comfort of the occupants. Basically, the designers and operators of ventilation systems should be familiar with the ventilation mechanisms, comfort requirements and the air quality necessary to achieve acceptable indoor climate.

Natural ventilation and mechanical ventilation operate under complete different principles. Each of them has its own set of advantages, disadvantages and applications, depending on local climate conditions, building type, and Building Regulations. Both in the design of new buildings and the retrofit of existing buildings, an integrated approach is normally used not only for thermal insulation, air tightness and heat recovery, but also for optimal utilization of sustainable technologies such as passive solar gains, passive and natural cooling, day lighting and natural ventilation. Since natural ventilation is a sustainable, energy-efficient and clean technology that is well accepted by occupants, natural ventilation techniques have been performed by both international and national energy policies as a key component of sustainable building. The successful application of natural ventilation techniques and the

effectiveness of natural ventilation are determined by the prevailing outdoor conditions and microclimate as well as by building design and building use [2].

1.2 Driving forces in natural ventilation

For a given configuration of openings, the rate of natural ventilation varies according to the naturally occurring pressure differences. The pressure differences are produced by the action of thermally (stack) generated pressures or wind.

1.2.1 Buoyancy-induced ventilation

Natural ventilation by thermal buoyancy is the air exchange between two or more zones with different air densities due to difference in temperatures and/or moisture content, where the last effect usually is of minor importance. Ventilation by air exchange implies openings between the zones and the opening arrangement can either be separate small openings in different levels or it can be a single large vertical or horizontal opening. The temperature difference can occur due to heating one or more of the zones.

The external and internal pressure distribution can be described as:

$$P = P_0 - \rho_0 g H$$

Where P is the external or internal pressure [Pa]
P_0 is the pressure at a reference level (floor) [Pa]
ρ_0 is the external or internal air density at a reference level [kg/m^3]
g is gravitational acceleration [m/s^2]
H is height above the reference level [m]

Thus, the buoyancy-induced pressure difference ΔP_t across an opening at height H can be calculated as:

$$\Delta p_t = P_{u0} - P_{i0} - gH(\rho_u - \rho_i)$$

If the air is regarded as incompressible and temperature difference is not large, according to the perfect gas law, the temperature and density differences are approximately related by:

$$\frac{\rho_u - \rho_i}{\rho_i} \cong \frac{T_i - T_u}{T_u}$$

Where ρ_u is the external air density [kg/m^3]
ρ_i is the internal air density [kg/m^3]
T_u is the external air temperature [K]
T_i is the internal air temperature [K]

Whether the air enters or exits a building at a certain height depends on the position of the opening compared to the neutral plane in the building, see Figure 1.1. At the neutral height above the floor, H_o, the pressure difference ΔP_t=0, then:

$$\Delta p_t = P_{u0} - P_{i0} - gH_0(\rho_u - \rho_i) = 0$$
$$P_{u0} - P_{i0} = gH_0(\rho_u - \rho_i)$$
$$P_{u0} - P_{i0} = \rho_i g H_0 \frac{T_i - T_u}{T_u}$$

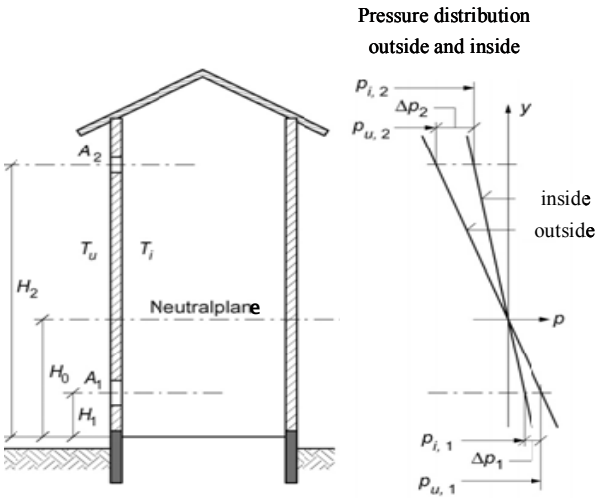

Figure 1.1: Pressure difference around the neutral plane in a building ventilated only by thermal buoyancy.

Similarly, the pressure difference for an opening of height H_1 is:

$$\Delta p_1 = P_{u0} - P_{i0} - \rho_i g H_1 \frac{T_i - T_u}{T_u}$$

$$\Delta P_1 = \rho_i g H_0 \frac{T_i - T_u}{T_u} - \rho_i g H_1 \frac{T_i - T_u}{T_u}$$

$$= \rho_i g \frac{T_i - T_u}{T_u}(H_0 - H_1)$$

1.2.2 Wind-induced ventilation

The wind-induced air flow into a building is affected by the pressure distribution around the building and more specifically at the openings in the building structure. The wind will make an overpressure at the windward side of the building and an underpressure at the leeward side and the parallel sides of the building, see Figure 1.2.

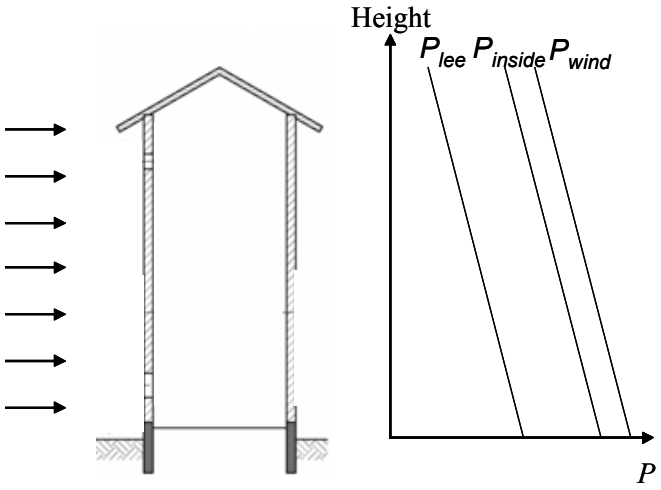

Figure 1.2: Pressure difference created by wind on a building.

The pressure due to wind flow into or away from a surface is proportional to the dynamic pressure and is calculated by:

$$P_w = C_P \frac{1}{2} \rho_u v_{ref}^2$$

Where P_w is the wind induced pressure [Pa]
C_P is the pressure coefficient
ρ_u is the external air density [kg/m^3]
v_{ref} is the wind speed at a reference height [m/s]

The dimensionless pressure coefficient C_P is an empirically derived parameter. The value of C_P at a point on the building surface is determined by the building geometry, the wind velocity (i.e. speed and direction) relative to the building, and the exposure of the building (i.e. its location relative to other buildings and the topography and roughness of the terrain in the wind direction.

Therefore, the pressure difference across an opening can be calculated as:

$$\Delta P_w = P_w - P_i$$
$$= \frac{1}{2} C_P \rho_u v_{ref}^2 - P_i$$

Where P_i is the internal pressure in the building [Pa]

And the pressure difference across a building is:

$$\Delta P_w = \frac{1}{2} C_{P,w} \rho_u v_{ref}^2 - \frac{1}{2} C_{P,l} \rho_u v_{ref}^2$$
$$= \frac{1}{2} \Delta C_P \rho_u v_{ref}^2$$

Where $C_{P,w}$ is the pressure coefficient on the windward side
$C_{P,l}$ is the pressure coefficient on the leeward side

1.2.3 Combined buoyancy and wind ventilation

When stack and wind pressure act simultaneously on a building, their combination will determine the air flow through building openings. The total driving force ΔP is the sum of the driving forces induced by buoyancy and wind:

$$\Delta P = \Delta P_t + \Delta P_w$$

1.3 Buoyancy driven natural ventilation through horizontal openings

The important issue of mass and energy transfer between different zones in buildings has attracted increasing international interest and research effort. Air flow through vertical openings between building zones has been widely researched but little information is available regarding flow in horizontal openings, especially that driven

by buoyancy [3]. Horizontal openings occur in staircases, stairwells, ventilation shafts, service shafts and chimneys and so mass and energy transfer through them have important implications regarding energy saving, thermal comfort, control of contaminants and micro-organisms and spread of fire and smoke. The flows in such openings are difficult to model mathematically because the countercurrent flows often occur simultaneously in opposite directions through different parts of the opening.

The flow of air and combustion products across vents governs the growth and spread of fires in compartments and buildings. The rate of inflow of oxygen from the ambient determines the combustion process and the energy release rate in fires for many practical circumstances. Similarly, the spread of the fire to adjoining areas is strongly dependent on the resulting flow through vents. Horizontal vents are important in many situations, for example in multi-room compartments, ships and containment buildings.

1.4 Research methods

There are three methods usually used to study buoyancy driven natural ventilation: empirical models, experimental measurements and computational fluid dynamics (CFD) simulations. Most researchers use the scale model measurements and empirical models to study the natural ventilation driven by buoyancy force only. Although these models are simple, they can not completely understand the highly transient and complicated behaviour of the air flow through horizontal openings. Thus, the full-scale experimental investigation is quite important. Nevertheless, the experimental measurement is an expensive method in terms of operation time and equipment costs. CFD is an alternative approach to study natural ventilation in buildings. CFD is becoming popular due to its informative results and low labour and equipment costs.

Thus, the phenomena of air flow through horizontal openings are investigated by means of full-scale measurements and CFD numerical simulations. The measurements are performed in a laboratory of Hybrid Ventilation Center at Aalborg University. Two cases of the buoyancy driven natural ventilation are measured, shown in Figure 1.3:

Case A: Single-sided one horizontal opening, the opening ratios L/D range from 0.027 to 4.455, where L and D are the length and the diameter of the opening.

Case B: One horizontal opening combined with one vertical opening,

(a) The opening ratios A_T/A_B<<1, where A_T and A_B are the areas of top horizontal opening and bottom vertical opening.
(b) One horizontal opening combined with one vertical opening, A_T/A_B ~1.
(c) One horizontal opening combined with one vertical opening, A_T/A_B>>1.

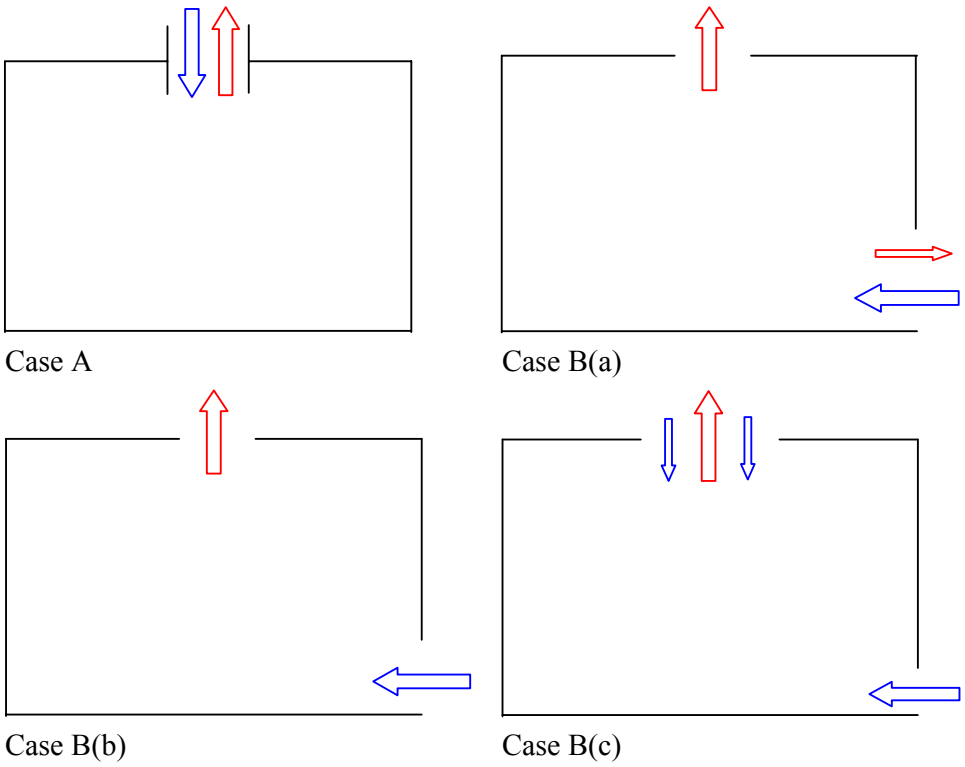

Figure 1.3: Measurement cases.

1.5 Research aims

This research work is focused on obtaining the air flow rate through the horizontal openings driven by buoyancy. The basic natures of air flow through horizontal openings are measured. Thus, this work is important and quite useful in relation to natural ventilation systems. The measurement results can be used in both simple calculation tools to give a rough estimate of the capacity for design of a ventilation system, but also be implemented in more detailed models, especially multi-zone models, for simulation of the performance of natural ventilation systems.

2 Literature review

2.1 Buoyancy driven natural ventilation through one horizontal opening

2.1.1 Measurement study

The earliest experimental work dealing with buoyancy driven flow through single opening in horizontal partitions was made by Brown [4]. Using air as the working fluid, it was shown that exchange flow rates increased with the vent aspect ratios *L/S* of opening length (or partition thickness) *L* to the side length of the square opening *S*, in the range of $0.0825 \leq L/S \leq 0.66$. Brown interpreted the countercurrent flow as a heat transfer phenomenon and expressed his results a correlation in terms of a Nusselt number *Nu*, versus Grashof number *Gr* and Prandtl number *Pr*:

$$Nu_L = 0.0546 Gr_L^{0.55} \Pr \left(\frac{S}{L} \right)^{\frac{1}{3}}$$

Mercer and Thompson [5], employing a brine solution and water as the working fluid pair, found that flow rates through inclined tubes decreased with the increasing of aspect ratios $3.5 \leq L/D \leq 18$, where *D* is the diameter of the opening. Those results indicated that a maximum value in the exchange rate exists at a certain intermediate *L/D* ratio. The 'purging' effectiveness implied a unidirectional flow through the vent from one region to the other, depending on the sign of ΔP, where

$$\Delta P = P_l - P_u$$

Here P_l and P_u are the hydrostatic pressures at the vent elevation in the lower and upper environments respectively. If $\Delta \left| P \right|$ exceeds some critical value $\Delta \left| P_C \right|$, then the flow becomes unidirectional.

The standard vent flow model based on Bernoulli's equation assumes unidirectional flow and breaks down if a bidirectional flow exchange occurs under the combined effects of buoyancy and pressure. This model predicts zero flow when $\Delta P = 0$. The volume flow rate q_u at the vent into the upper region from the lower region is taken as uniform and given by the model as:

$$q_u = C_d A \sqrt{\left| \frac{2\Delta P}{\rho_l} \right|}$$

Where C_d is the flow discharge coefficient.

If $\Delta P<0$, the flow q_u into the lower region is obtained. However, there is a flow across the vent due to the density difference $\Delta\rho$ due to the fluid in the upper region being heavier than that in the lower region. Therefore, it is important to determine the volume flow rate q at arbitrary values of $\Delta\rho$, ΔP and L/D. Copper [6] developed an analytical model, employing an exchange-flow component q_{ex}. Thus, q_{ex} becomes zero if the density distribution across the vent is stable, and also if $\Delta \left| P \right| > \Delta \left| P_C \right|$.

Epstein [7] has performed a detailed experimental study in a brine-water scale model for the exchange flow through a single horizontal opening in a large range of vent aspect ratios $0.01 \le L/D \le 10$. He defined correlations between the Froude number *Fr and L/D*. Epstein also identified four distinct flow regimes as a function of vent aspect ratio, which were named oscillatory exchange flow (Regime I, $L/D<0.15$), Bernoulli flow (Regime II, $0.15 \le L/D \le 0.4$), combined turbulent diffusion and Bernoulli flow (Regime III, $0.4 \le L/D \le 3.25$), and turbulent diffusion (Regime IV, $L/D>3.25$). At very small opening heights ($L/D<0.15$) the pressure level on both sides of the opening is essentially the same and an oscillatory exchange flow regime will be established (Regime I). For larger values of L/D the flow regime changes from countercurrent orifice flow regime (Regime II, $0.15 \le L/D \le 0.4$) to a turbulent diffusion flow regime for very large values (Regime IV, $L/D>3.25$). In the turbulent diffusion flow regime the air exchange was much slower and the countercurrent flow within the tube appeared to comprise of packets of warm and cold air with a chaotic and random motion. For intermediate values ($0.4 \le L/D \le 3.25$) the flow will be a combination of an orifice flow and turbulent diffusion flow regime (Regime III). According to the four flow regimes, Epstein gave the following relations of Froude numbers and L/D, see also in Figure 2.1:

$$Fr = \frac{q}{\sqrt{\frac{g(T_i - T_u)D^5}{T_i}}}$$

$$Fr = 0.055 \qquad \frac{L}{D} < 0.15$$

$$Fr = 0.147\left(\frac{L}{D}\right)^{\frac{1}{2}} \qquad 0.15 < \frac{L}{D} < 0.4$$

$$Fr = 0.093\frac{1}{\sqrt{1+0.084\left(\frac{L}{D}-0.4\right)^{3}}} \qquad 0.4 < \frac{L}{D} < 3.25$$

$$Fr = 0.32\left(\frac{L}{D}\right)^{-\frac{3}{2}} \qquad 3.25 < \frac{L}{D} < 10$$

Where q is the exchange air flow rate [m^3/s]
g is the gravitational acceleration [m/s^2]
T_i is the inside temperature [K]
T_u is the outside temperature [K]
L is the length (or height) of opening [m]
D is the diameter of the opening [m].

In Epstein's work, the results were consistent with the previous studies in which a peak was found in the flow exchange rate for aspect ratio near 0.6. The purely empirical correlation for the exchange flow rate was computed over the entire range of *L/D*:

$$Fr = \frac{q}{\left(D^5 g\frac{\Delta\rho}{\overline{\rho}}\right)^{\frac{1}{2}}} = \frac{0.055\left[1+400\left(\frac{L}{D}\right)^{3}\right]^{\frac{1}{6}}}{\left[1+0.00527\left(1+400\left(\frac{L}{D}\right)^{3}\right)^{\frac{1}{2}}\left(\left(\frac{L}{D}\right)^{6}+117\left(\frac{L}{D}\right)^{2}\right)^{\frac{3}{4}}\right]^{\frac{1}{3}}}$$

The volume flow rate q from the upper compartment to the lower compartment or vice versa in terms of rate of dilution of the brine can be shown as:

$$q = \frac{-V_u \dfrac{d\rho_u}{dt}}{\left(\rho_u - \rho_{l,0}\right) - \dfrac{V_u}{V_l}\left(\rho_{u,0} - \rho_u\right)}$$

Where V_u is the volume of the heavy liquid in the upper compartment
V_l is the volume of the less dense liquid in the lower compartment
ρ_u is the density of the brine solution at time t
$\rho_{l,0}$ is the densities of the water compartments at zero time
$\rho_{u,0}$ is the is the densities of the brine compartments at zero time

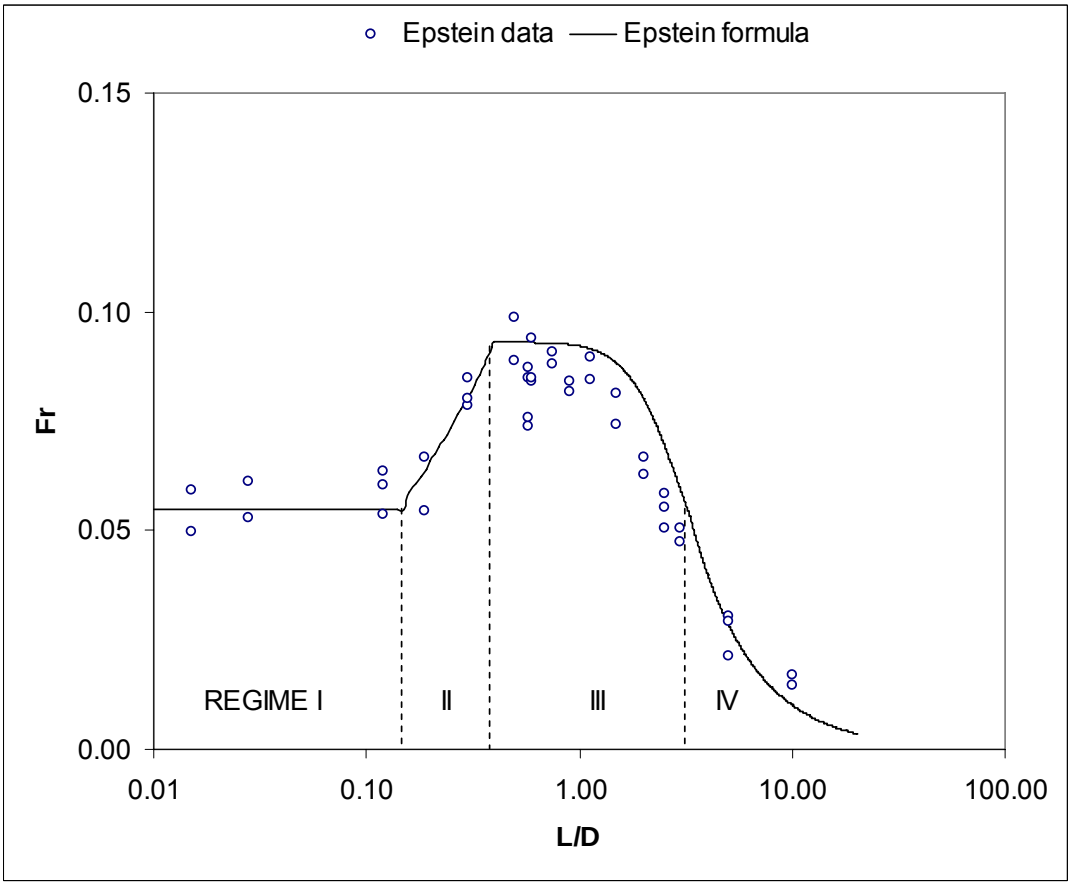

Figure 2.1: Experimental results for countercurrent exchange flow through a single horizontal opening, given by Epstein (1988).

Q. Tan and Y. Jaluria [8] studied the flow through a horizontal vent using fresh and saline water to simulate the density differences raised in fires due to temperature rise in the enclosure. In the absence of a pressure difference, a bidirectional flow arises

due to buoyancy effects. As the pressure increases and leakages are present, the flow gradually shifts to a unidirectional flow. The transport processes across the vent may be characterized in terms of the two dimensionless variables *L/D* and the buoyancy parameter *B*,

$$B = \frac{g\Delta\rho D}{\Delta P}$$

The flow rate at relatively large pressure differences can be obtained. For $0.25<L/D<6.08$ and $0.043<\Delta\rho/\overline{\rho}<0.13$, the correlating equations for q_o and q_u were obtained as

$$q_o = 2.313\times10^{-7}\left(\Delta P\right)^{0.914}\left(\Delta\rho\right)^{-0.157}\left(L/D\right)^{0.0369}$$
$$q_u = 5.048\times10^{-7}\left(\Delta P\right)^{0.8709}\left(\Delta\rho\right)^{-0.2394}\left(L/D\right)^{0.0301}$$

Where q_0 is the net upward flow rate [m^3/s]
q_u is the upward flow rate [m^3/s]

Y. Jaluria et al. [9] investigated the flow visualization on the flow transport across a horizontal vent in a compartment with nonzero pressure and density differences across the vent. They studied the vent flow for the aspect ratio range of 0.0144 to 6.0. The main focus was to find the critical pressure difference that distinguished the unidirectional flow regime from the bidirectional flow regime. The study also included flow visualization with shadowgraph for different pressure differences across the vent. Two different flow systems based on water/brine and air arrangements were considered in experiments. Though the basic trends in terms of average flow rates, purging pressure and transition from bidirectional to unidirectional flow as the pressure difference increases were similar in the two systems, strong differences were indicated by flow visualization in the transient effects that arise and in the resulting flow patterns. Transient effects were shown to be very important for the air system and the oscillatory nature of the transport processes was brought out.

The case of zero pressure difference across the vent also studied by Conover and Kumar [10], who used laser Doppler velocimetry (LDV) and densimetry to study the flow behaviour for aspect ratio close to 1. Their experimental results were in agreement with those obtained by Epstein. Conover et al. [11] also studied experimentally the buoyancy driven bidirectional pulsating exchange flow through a

vent in a horizontal partition using a brine-water system. The transient and pulsating exchange flows were studied by densimetric measurements, flow visualization and LDV measurements for three different vent ratios: 0.106, 0.0376 and 0.008. Flow visualization was used to understand the flow features contributing to the pulsating flow and to provide a quantitative measure of the major pulsation frequency. For higher values of *L/D*, a single dominant pulsation frequency was identified. However, for vents of very low aspect ratio (*L/D*=0.008) a second frequency existed, which was caused by secondary ripples that were observed through flow visualization studies in the circumferential direction along the brine-water interface.

Reynolds [12] and Reynolds et al. [13] made the experiments in a reduced scale model of a typical stairwell. The investigated configuration included the stairs and the air flow between the compartments occurred through an inclined channel with two different constructions of the ceiling. The circulating flow between the compartments was put into motion by convective current of a heater placed in the lower compartment. The air flows were computed from the velocity readings made at limited locations. Dimensional analysis suggested a relation between the Froude number and a ratio of the temperature difference to mean temperature, corrected by a function of the Renolds number required to characterise a particular stairwell configuration.

D. Blay and B. Gautier [14] carried out experiments for smaller aspect ratio of *L/D* in a water scale model. Flow visualizations pointed out the complexity and instability of the flow in the aperture where both cold and warm fluids fully interpenetrate each other. The flow appeared to look like two symmetrical plumes issuing from the partition aperture acting itself as a virtual reservoir maintained at the average temperature of both rooms. D. Blay and P. Le Quéré [15] carried out experiments and direct numerical simulations in the case of a 1m high air filled cavity partitioned into two compartments communicating through a square opening (Rayleigh number comprised between 10^9 and 4×10^9). These two works showed that, for small values of *L/D*, the flow was controlled by buoyancy effects rather than friction forces along the aperture walls, and the main governing parameter was the temperature difference and the room height but not the partition thickness as assumed by Brown and Epstein.

D. Blay et al. [16] carried out a full-scale experiment in order to get a better understanding of the natural thermosyphon flow between two rooms at different temperatures communicating through a horizontal aperture. The flow was governed by buoyancy forces and the flow structure corresponds to two symmetrical plumes

issuing from the aperture. Flow rate and heat transfer rate through the horizontal aperture were defined by Froude and Nusselt numbers.

C. Blomqvist and M. Sandberg [17] carried out experiments in a scale model with salt bath technique, in order to study the air movements in a horizontal opening with and without staircase below the opening. The results indicated that the flow resistance of the opening will decrease when the sloping plane is added below it, and the staircase will increase the fluid exchange through the opening slightly.

K. Klobut and K. Siren [18] and K. Klobut [19] carried out laboratory experiments to investigate the influence of several parameters on combined forced and density-driven air flow through large opening in a horizontal partition. Variable parameters included the direction and rate of the net flow, the temperature difference between the zones and the dimensions of the large opening. The term 'minor flow' was used referring to the flow from the zone with the exhaust opening to the zone with the supply opening. The term 'major flow' was used to be the sum of the minor flow and the net flow. The results showed the variable parameters effects on the minor flow and the major flow.

Takeyoshi Tanaka [20] investigated the behaviour of smoke in cavity like spaces. In the experiments the cavity had no opening at the bottom and the fire source was located at the centre on the floor. It was found that the temperature rise of plume at the cavity opening was well scaled by the dimensionless temperature.

Gary R. Hunt and Joanne M. Holford [21] measured the discharge coefficient C_d for the flow through a sharp-edged circular horizontal opening. The results showed that the discharge coefficient was dependant on the temperature difference across the opening and that the large contrasts in temperature may reduce the discharge coefficient significantly. A dimensionless parameter, the discharge parameter Γ_d, is characterised the extent of the contraction, Γ_d provides a measure of the relative importance of buoyancy and inertia at the opening. Highly buoyant, low velocity releases from large area openings give large values of Γ_d and large contractions.

J. Halldorsson et al. [22] made experiments to study a full scale solar chimney as a ventilation device. The results showed that by changing the chimney gap while maintaining all the other conditions, the airflow rate increased continuously with increasing chimney gap. Results also showed that the airflow rate reached a maximum at a chimney inclination angle of around 45º, which is about 45% higher than that for a vertical chimney. The reason for this flow rate increase is due to the relatively even

airspeed inside the chimney, which significantly reduces the pressure loss at the chimney inlet and outlet compared to the corresponding vertical chimney.

Andrew W. Woods [23] investigated the effect of a solar chimney on the effectiveness of natural ventilation in a large open building. The solar chimney was modelled as a stack which was subject to additional heat gains, which enhanced the buoyancy of the fluid and increased the natural ventilation flow. It was shown that in regimes of low internal heat load, the additional solar drive can lead to a much enhanced natural ventilation flow.

J. S. Kohal et al. [24] measured the natural convection through a large horizontal opening of different sizes and shapes located between two rooms in a building. Airflow rates between the two rooms were measured using a tracer gas decay technique. The discharge coefficient of the opening was found to be a function of the temperature difference between the two rooms. The study showed that the average discharge coefficient was in the range 0.29-0.43 for circular openings and 0.26-0.35 for square openings, while the dimensions of the opening were varied between 0.288 and 0.48m^2 and the thickness was 0.3m.

2.1.2 CFD study

L. Shao and S. B. Riffat [1] [25] simulated the buoyancy driven flow through horizontal openings using the CFD code FLUENT. The transient velocity field was predicted using a time dependent method. Good agreement between CFD predicted flow rate and that based on experimental measurement was obtained with a relative difference of 10.5%. The time dependent computation revealed that the flow patterns in the modelled zones as well as in the horizontal opening are highly transient and unstable and the dominant mode of air exchange through the opening is intermittent pulses. It was also found that the flow rate through the opening increases with the temperature difference between the zones and the area of the horizontal opening.

J. S. Kohal et al. [24] simulated the natural convection through a large horizontal opening between two rooms in a building using two-dimensional, time dependent CFD modelling. His CFD predictions agreed with analytical results that the exchange rate through the horizontal opening increases with increasing the size of opening, and the results showed that the buoyancy driven flow occurs in random pulses through the horizontal opening.

Robert E. Spall and Elgin A. Anderson [26] investigated the dynamics of buoyancy driven, pulsating exchange flow between compartments in a cylindrical tank separated by a thin, vented, horizontal partition. This work was studied by numerically integrating the unsteady, axisymmetric Navier-Stokes equations. The results for the computed flow coefficient were in agreement with Epstein's theoretical prediction. The flow coefficient was found to vary about 2% over the range 200s≤t≤1000s. For values t<200s, the coefficient was affected by flow field transients likely associated with the start-up phase. The results also indicated the presence of two dominant pulsation frequencies: one higher frequency that coincides with boundary layer shedding from the partition walls at the orifice opening, the other a lower multiple of this frequency associated with the evolution of complex vortical structures as they translate away from the orifice region.

2.1.3 Literature analysis of experiment study and CFD study

The literature survey shows that the brine-water system and the scale model are normally used for the research work of air flow through horizontal openings. The brine-water technique has some advantages compared to the experiment with air as the working fluid. There is no need to cover the test section with insulation as the density-driven flow is isothermal, and there is no long waiting time requirement for steady state to be reached. However, the major shortcoming of the brine-water technique is due to the essentially incompressible nature of water as compared to air. As a consequence, some differences may be expected in the highly transient behavior of the air flow through a single horizontal opening.

For some of the above references, the *Fr* data versus *L/D* through one horizontal opening are compared with the Epstein's data, shown in Figure 2.2. The measurement results from Conover et al. and Q. Tan are in good agreement with the Epstein's data; but the *Fr* value from D. Blay and J. S. Kohal shows much large difference with the Epstein's data. Thus, in order to find a valuable calculation formula to calculate the air flow rate through one horizontal opening driven by buoyancy in a natural ventilated building, it is important to investigate the complicated phenomenon by means of a full-scale air flow model measurement.

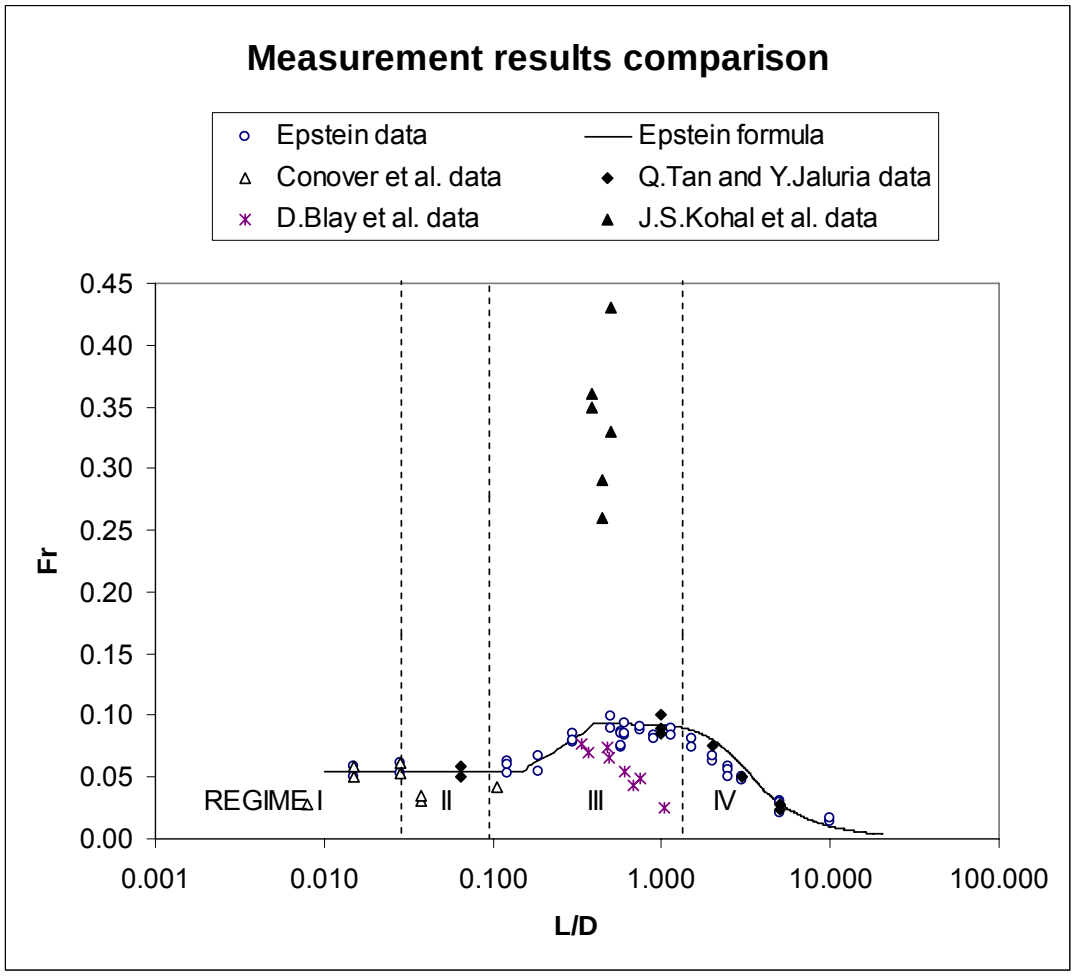

Figure 2.2: *Fr* number versus *L/D* comparison between different literatures.

In addition, very few literatures can be found to study this complicated, highly transient phenomenon using CFD modelling method, especially for LES simulations. It can be expected that some interesting conclusions will be obtained if different turbulence models are used.

2.2 Buoyancy driven natural ventilation through one horizontal opening combined with one vertical opening

When the air temperature and air density inside a room is different from the outside air temperature and density, buoyancy induced pressure gradients across any openings between the room and the exterior are produced. These will drive an exchange air flow which ventilates the room. For buoyancy driven natural ventilation with one high level opening and one low level opening, two main forms of ventilation has been identified: displacement ventilation and mixing ventilation [27]. Mixing ventilation

occurs when the incoming ambient air mixes with the air within the space, when the dense air enters at a high level inlet. In this case vertical stratification is weak. Displacement ventilation occurs when dense air enters at a low level opening and displaces the lighter air within the space out at a high level opening. A strong stable stratification develops in this case, and there is little mixing between the incoming air and that in the interior.

Several models have been used for explaining the mechanism of displacement ventilation by thermal buoyancy. The column and the fan model were used in the earliest research work. In the column model, the driving force was assumed to be the thermal buoyancy on a column of warm air immersed in colder surrounding air [28]. The fan model assumed the same driving force as the column model and this force creates the air movement in the openings and overcomes the friction losses. The pressure model, is commonly used in recent studies, is based on the indoor and outdoor barometric pressure distributions [29]. Linden et al. [27] investigated buoyancy driven natural ventilation through two-level openings using an emptying filling boxes model. Both mixing ventilation and displacement ventilation were studied theoretically and the results were compared with laboratory brine-water scale experiments. For displacement ventilation, they assumed two temperature zones in the enclosure, with the bottom zone air temperature same as the outdoor air temperature. Andersen [30] derived a solution for natural ventilation by thermal buoyancy in a room with two openings and with uniform temperature. Li [31] derived buoyancy driven ventilation airflow and thermal stratification solutions in a single-zone building with empty air filling box model. In all previous displacement ventilation models, the flow through the openings was assumed in only one direction. In reality, the air flow directions will be varied as function of the opening ratio.

When two openings are placed at high level and low level respectively, it is well known that for a given indoor air temperature T_i and an outdoor air temperature T_o, the buoyancy driven natural ventilation flow rate through these two openings can be calculated as [30][32]:

$$q = C_d A^* \sqrt{\frac{2gh(T_i - T_o)}{T_o}}$$

$$A^* = \frac{A_T \cdot A_B}{\sqrt{A_T^2 + A_B^2}}$$

Where q is the exchange air flow rate [m^3/s]
A^* is the effective opening area [m^2]
A_T is the area of the top opening [m^2]
A_B is the area of the bottom opening [m^2]
g is the gravitational acceleration [m/s^2]
T_i is the inside temperature [K]
T_o is the outside temperature [K]
h is the vertical distance between the two openings [m]
C_d is the discharge coefficient of the opening.

In the case of the two square sharp-edged openings, C_d is assumed to have the same value $C_d \approx 0.65$ [30].

In the development of this equation it is assumed that the air flow through the two openings is unidirectional. The opening area ratio A_T/A_B is not taken into account. Thus, the air flow pattern and the air flow rate calculation are not correlated with the opening ratio. In fact, the air flow pattern and the air flow rate will change when the opening area ratio reaches a certain level. The air distribution and the temperature gradient change as well inside the room. As the consequences, these situations will influence the thermal comfort and indoor air quality.

3 Measurement set-up

3.1 Measurement test rig layout

The experimental analysis of buoyancy driven natural ventilation through horizontal openings were performed in a laboratory of Architectural Engineering at Aalborg University. The experiments are carried out in a full-scale test cell which is divided into two rooms, namely the “thermostatic chamber” and the “test room”. The thermostatic chamber is 8m length, 6m width and 4.7m height; and the test room is 4.1m length, 3.2 m width and 2.7m height, respectively. The test room connects with the thermostatic chamber with either a horizontal opening, or a horizontal opening and a vertical opening with different sizes. One external door communicates the laboratory and the thermostatic chamber, and another external door connects the test room with the laboratory. Both doors are kept closed and sealed throughout the experiments. The thermostatic chamber and the test room layout are shown in Figure 3.1, as well as the parameters of them are shown in Table 3.1. Figure 3.2(A), (B) and (C) show the outside view and inside view of the full-scale test rig. Different cases are examined by varying the temperature differences of inside and outside of the test room and the opening cases.

One square horizontal hole of side length 1m is located on the roof center of the test room, and one square vertical hole of side length 0.6m is located on the bottom of one test room’s side wall. The thermostatic chamber simulates the environmental conditions controlled accurately by an air conditioner. The higher indoor temperature is produced by heating cables uniformly distributed on the floor inside the test room. CO_2 constant injection tracer gas system, thermocouples, anemometers and Laser Doppler Velocimetry (LDV) are used to measure the air flow rate, air temperatures and air velocities, respectively. Special attention is paid to ensure the pressure difference to be zero between the chamber and the laboratory hall in order to avoid unnecessary errors of infiltration and exfiltration. Different cases are examined by varying the temperature differences of inside and outside of the test room, the opening area and the opening ratios. The essential features of the experimental system are schematized in Figure 3.3.

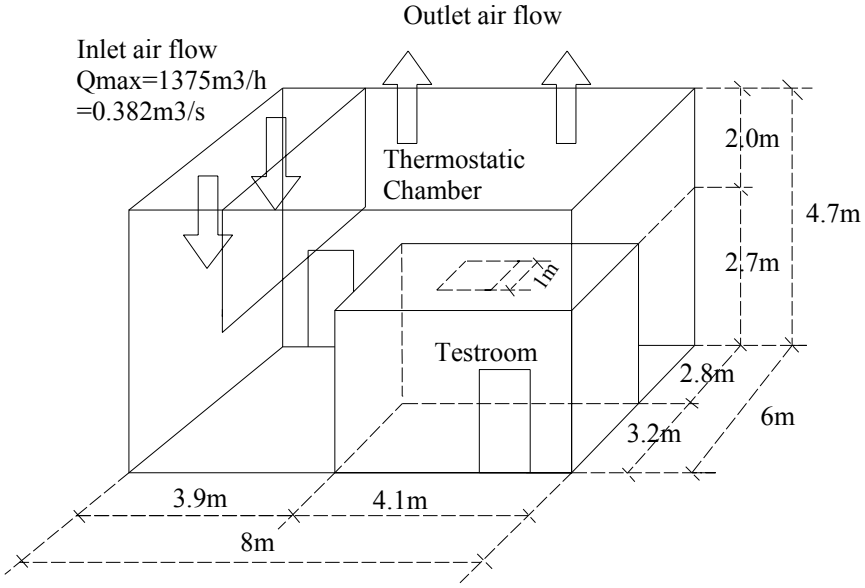

Figure 3.1: The experiment test cell layout.

Figure 3.2(A): The outside view of the full-scale test rig.

Figure 3.2(B): The upper part inside view of the test room.

Figure 3.2(C): The lower part inside view of the test room.

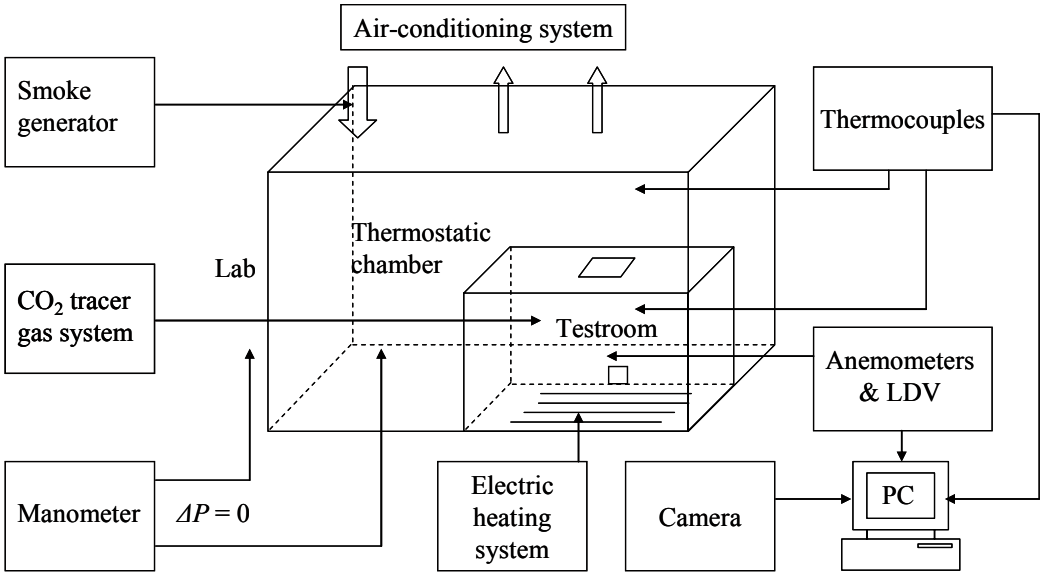

Figure 3.3: Schematic representation of system and measurement equipments.

	Thermostatic chamber	Test room
Length [m]	8.0	4.1
Width [m]	6.0	3.2
Height [m]	4.7	2.7
Floor area [m^2]	48.0	13.12
Volume [m^3]	220.8	35.42
Lateral wall surface area [m^2]	128.8	39.42
Glazed wall surface area [m^2]	28.8	12.57
Opaque wall surface area [m^2]	148.0	53.09
U-value of glazed wall [W/m^2K]	2.7	2.7
U-value of opaque wall [W/m^2K]	0.23	0.23
U-value of ceiling [W/m^2K]	0.23	0.23
U-value of floor [W/m^2K]	0.29	0.29
Max. Volume airflow rate of the air conditioner [m^3/h]	1375	-
Insulated wall thickness [m]	0.13	0.17
Insulated ceiling thickness [m]	0.13	0.133

Table 3.1: The parameters of the test rig.

3.2 Thermal field measurement

The thermal field measurements include indoor temperature (inside of the test room), outdoor temperature (outside of the test room, i.e. inside of the thermostatic chamber) and the laboratory's temperature. A total 52 of calibrated K-type thermocouples are used as thermal sensors (uncertainty ±0.15°C). The thermal experimental set-up consists of five vertical indoor columns of sensors (C1, C2, C3, C4 and C5, total of 26 sensors) to monitor the vertical temperature stratification; two vertical outdoor columns of sensors for chamber (C6 and C7, total 9 sensors); four groups of sensors for indoor walls (Tw6, Tw7, Tw8 and Tw9, total 12 sensors); one group of sensors for indoor ceiling (Tw10, total 3 sensors); one sensor for the inlet temperature from the air conditioner, and one sensor for the ice point of the FLUKE HELIOS. The temperature measurement set-up is shown in Figure 3.4(A) and (B). All of the sensors are connected to a FLUKE HELIOS Plus 2287A data logger and a PC. The output data is sampled at every ten seconds.

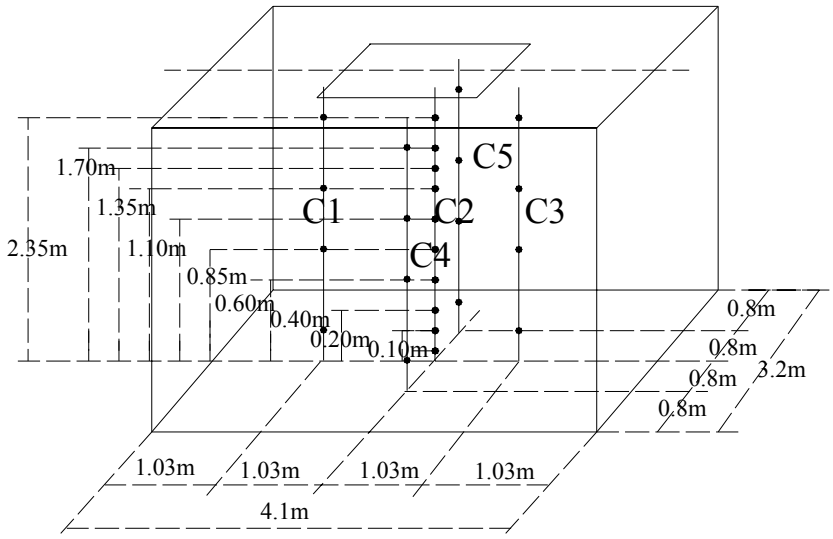

Figure 3.4(A): Thermal field measurement set-up, black dots are the locations of thermocouples.

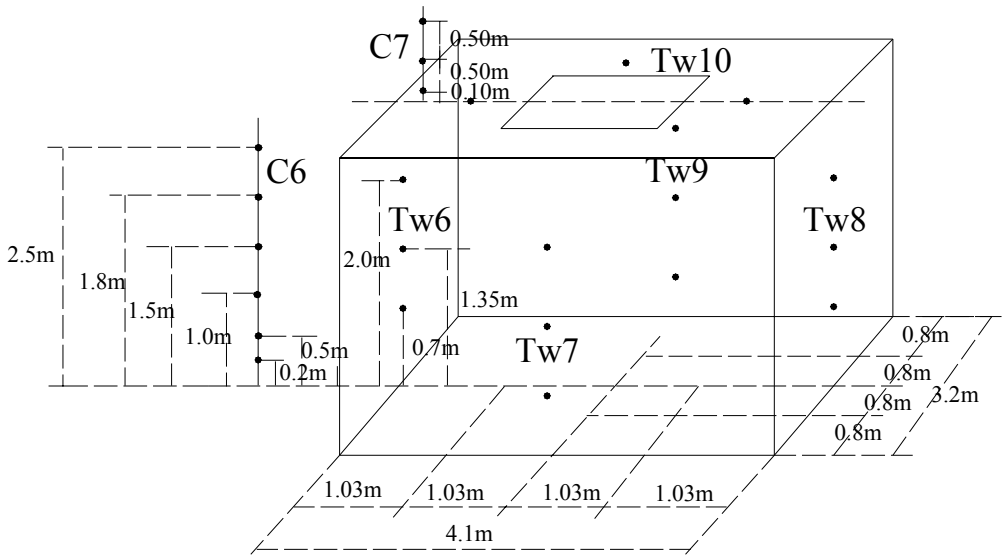

Figure 3.4(B): Thermal field measurement set-up, black dots are the locations of thermocouples.

The temperature difference is built up by indoor higher temperature and outdoor lower temperature. The indoor temperature is built up by a heating cable of total 2KW uniformly distributed on the floor of the test room. The output electrical power of the heating cable is controlled by a transformer in order to get different indoor temperature. At the same time the outdoor temperature keeps about 10°C controlled accurately by an air conditioner.

3.3 Velocity field measurement

3.3.1 DANTEC 54R10 measurement

During the indoor airflow velocity measurements the sensors should be fixed locations where the air velocity is much more interested. The velocity measurement results are produced by using a Dantec low velocity measurement system. The total of 21 calibrated hot sphere anemometers, DANTEC 54R10, are used to measure the indoor airflow velocity (uncertainty ±0.02m/s). The experimental set-up consists of one vertical and one horizontal indoor column of sensors under the center of the opening, which is shown in Figure 3.5. The sensors on the vertical column are located as the same places as the thermocouples on this column, and the sensors on the horizontal column are located just below the horizontal opening. The 54R10 is an omni-directional fully temperature-compensated sensor. A fast response time is essential for accurate estimation of turbulence in the airflow. Each sensor has two nickel-plated quartz spheres supplied with a small electrical current. The current heats

the spheres which in turn are cooled by passing airflow. Velocity is measured by regulating the electrical current to maintain the spheres at a constant temperature. All of the sensors are connected to a multi-channel flow analyzer, DANTEC 54N10, and the mean velocity data during the measure time is also output by a PC. The output is sampled at every two minutes. With this system one can present mean velocity, standard deviation (RMS), turbulence intensity, velocity histogram, air temperature measurement results. The probes are omni directional, and therefore they can not give the direction of the air flow.

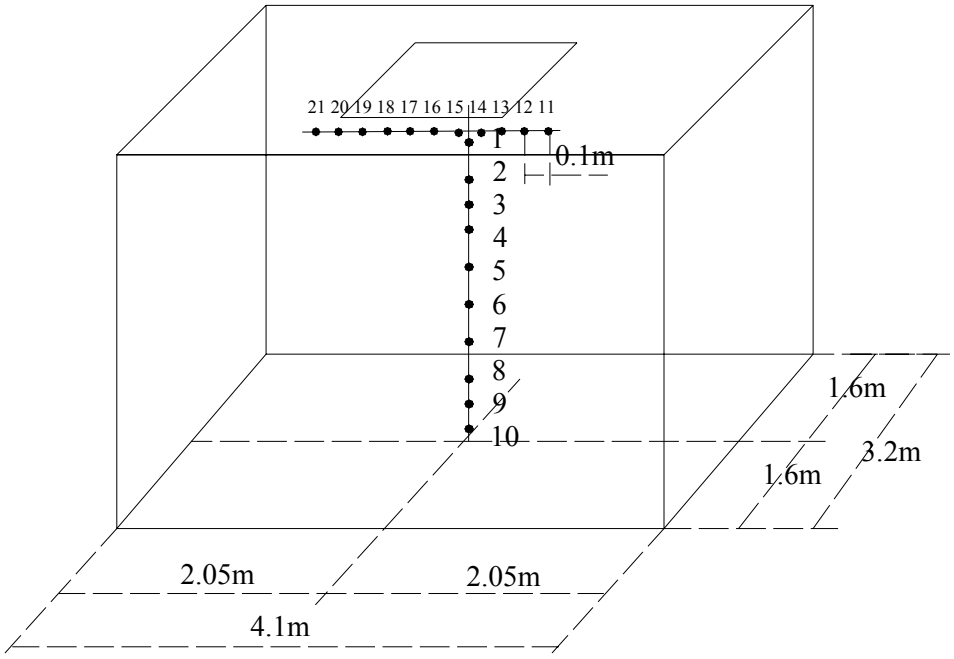

Figure 3.5: Velocity field measurement set-up, black dots are the locations of the hot spheres, and the numbers are the velocity sensors' number.

3.3.2 LDA measurement

In order to research the airflow velocity and turbulence through the horizontal opening, a Laser Doppler Anemometry (LDA) is utilized. LDA is non-contact optical instrument for investigating flow field. Velocity measurement is carried out by focusing a laser beam on to the measuring point and observing the frequency shift of the light scattered by moving particles. As a result, very rapid fluctuations in the fluid velocity can be accurately measured. Unlike the hot sphere measurement, the LDA system uses no probe at the measuring point and therefore no disturbance to the flow occurs.

In this measurement work, velocity is measured by the Dantec Flowlite laser-optics system, which is used for Dantec's Flow Velocity Analyzer signal processor (FVA enhanced 58N40). The uncertainty of velocity measurement is less than ±1%. FVA is controlled by Dantec's FLOware software, which runs on a personal computer. This laser instrument can only measure the velocity in one velocity component direction at one measuring point. Thus, the vertical velocity component is measured for the air flow through the horizontal opening.

3.4 Air flow rate measurement

Tracer gas techniques generally provide the direct measure of the total flow rate (including infiltration) of outdoor air into the room. In these techniques a readily detectable tracer is injected into the space and the concentration history in the room is recorded. All methods, except the constant concentration method, require that the building can be treated as a single well-mixed zone and it is therefore often necessary to employ artificial internal mixing.

Since the test cell is sealed well enough, the tracer gas constant injection technique can be used for evaluating the air flow rate through the opening. The used tracer gas is Carbon Dioxide (CO_2). The tracer gas system includes injection and distribution devices (a gas bottle, injection tubes, a reduction valve, a CO_2 flowmeter, a couple of small mixing fans) and tracer gas sampling apparatuses (a Binos 100 analyzer and a Uras analyzer). Binos analyzer is used to measure the CO_2 concentration at equilibrium state inside the test room, and Uras analyzer is used to monitor when the equilibrium state arrives. The concentration measurement of tracer gas system is calibrated to an uncertainty of ±2%.

The constant air flow rate at steady state can be obtained by the equilibrium concentration [33]

$$q = \frac{q_{tracer}}{C(\infty) - C(0)}$$

Where q is the air flow rate [m^3/s]
q_{tracer} is the tracer gas constant injection flow rate [m^3/s]
$C(\infty)$ is the equilibrium concentration of the CO_2 tracer gas [ppm]
$C(0)$ is the CO_2 concentration of the atmospheric air about 390 [ppm].

When the equilibrium steady state is reached, a couple of fans are used to maintain homogenous mixing of the gas in the room air after the opening is closed and tracer gas supply is stopped, and the Binos is used to measure the *C(∞)*. The concentrations of CO_2 are monitored by Uras at five points inside the test room and one point outside the test room, shown in Figure 3.6.

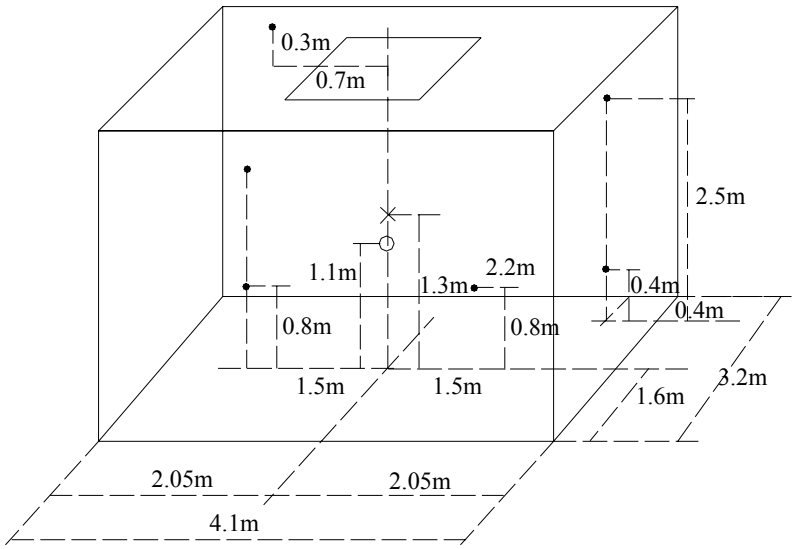

Figure 3.6: CO_2 concentration measurement set-up, '×' are the locations of the concentration sampling points measured by Binos, '•' are the locations monitored by Uras, 'o' is the location of injection point.

The volume flow rate of the tracer gas to be injected q_{tracer} is determined according to the following steps:

(1) Estimate the air flow rate q and convert it into q_{est} in the time units of $q_{tracer.}$

(2) Determine the target tracer gas concentration C_{target}=2000ppm that is over the mid-range in the detection limits of the gas analyzer Binos 100.

(3) Compute the following:

$$q_{tracer} = C_{target} \times q_{est}$$

This equation presents one method used to calculate a tracer gas flow rate in order to obtain a more rapid tracer gas concentration equilibrium.

3.5 Airflow visualization

Flow visualization in a room is important in ventilation studies not only to provide a qualitative assessment of the flow pattern but also in some cases it is used to yield quantitative information of the air motion. In this research work, smoke is used to highlight the flow pattern and turbulence which is photographed and recorded using a digital camera. The SAFEX Fog Generator is a powerful and small device. A white, dense fog which is non-irritant, non-flammable and non-hazardous is generated by evaporation and condensation of a water-based fog liquid.

3.6 Openings

3.6.1 One horizontal opening

In this case only one square horizontal opening is located on the roof center of the test room; see Figure 3.2(B) and Figure 3.7. The side lengths *S* of the single square opening are 0.2m, 0.4m, 0.6m, 0.8m and 1.0m respectively, so the opening areas vary from $0.04m^2$ to $1.0m^2$. The roof thickness of the test room is 0.133m, and the opening heights vary from 0.133m to 1.0m, thus the opening ratios *L/D* might vary in the range from 0.115 to 4.455. In order to measure very small *L/D* ratios, an insulated metal plate with thickness 0.012m and side length 1.0m is used and located on the test room roof center. A square hole is opened with different side length 0.1m, 0.2m, 0.3m and 0.4m, therefore *L/D* ratios from 0.027 to 0.106 may be obtained, see Figure 3.8(A) and Figure 3.8(B). Because the square opening side length is much smaller than the metal plate length, the flow influence of test room's roof thickness may be ignored.

For a square opening with a side length *S*, *D* should be viewed as the diameter of a round opening that has the same area as the square opening described by the following relation:

$$D = \sqrt{\frac{4}{\pi} S^2} = 1.128 \cdot S$$

If another opening ratio *L/S* is defined as the length of the opening *L* to the side length of the opening *S*, the *L/S* ratios range from 0.03 to 5.0.

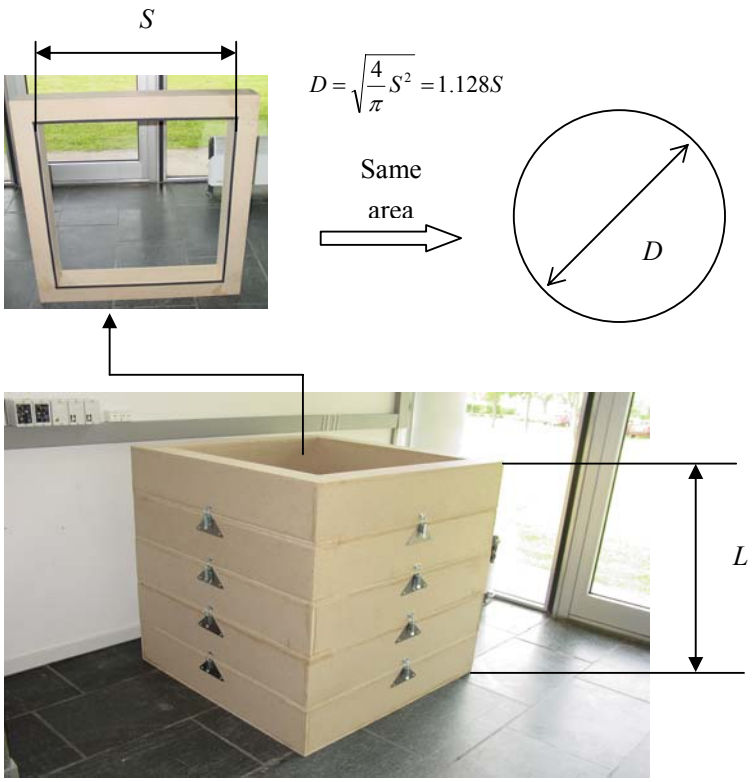

Figure 3.7: The horizontal opening.

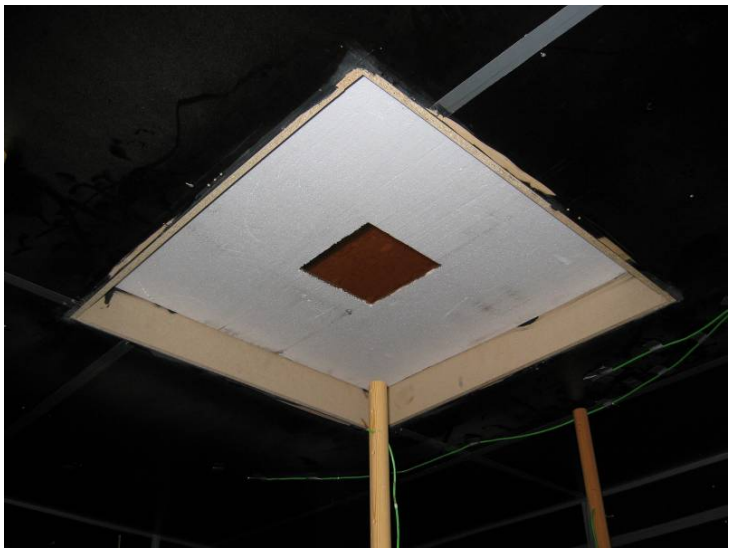

Figure 3.8(A): The metal plate with opening from inside view of the test room.

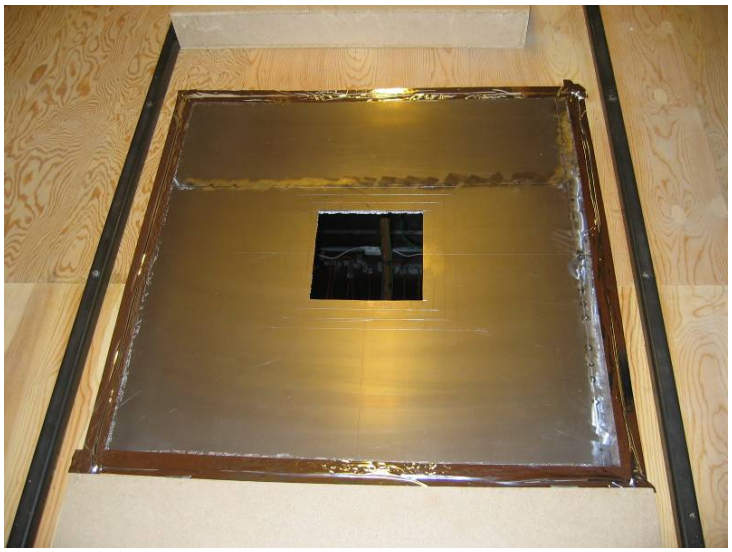

Figure 3.8(B): The metal plate with opening from outside view of the test room.

3.6.2 One horizontal opening combined with one vertical opening

The experimental study of the phenomenon of buoyancy driven natural ventilation through a high-level horizontal opening combined with a low-level vertical opening is performed. The measurements are made for opening ratios A_T/A_B in the range from 0.11 to 25, where A_T and A_B are the areas of the top horizontal opening and the bottom vertical opening. Different cases are examined by varying the temperature difference of inside and outside of the test room, the opening area and the opening ratio A_T/A_B. The measurements are carried out with the top horizontal opening of side length S_T from 0.2m to 1.0m, and the bottom vertical opening of side length S_B from 0.2m to 0.6m. Thus the opening ratios A_T/A_B vary in the range from 0.11 to 25, see the measurement set-up in Figure 3.9.

Figure 3.9: The inside view of the test room. The side length of top horizontal opening S_T=0.8m, the side length of bottom vertical opening S_B=0.3m, and the opening ratio A_T/A_B=7.11.

3.7 Experimental procedure

The experimental procedure can be divided into the following phases:

(1) Initial measurement period to reach steady state buoyancy driven air flow rates at a certain temperature difference with the horizontal opening opened;
(2) An injection period of CO_2 tracer gas at a constant flow rate q_{tracer} until steady state concentration levels are reached. The amount of tracer gas is controlled to reach an average CO_2 concentration of about 2000ppm;
(3) Recording period of temperatures, seven points' tracer gas concentrations and air velocities when steady state equilibrium has been reached;
(4) Final recording period of the average CO_2 concentration in the test room after closing the opening and the tracer gas injection simultaneously and turning on the mixing fans.

4 Computational Fluid Dynamics

4.1 Introduction

In the last thirty years the development of the Computational Fluid Dynamics (CFD) has made it possible to get a better understanding and to simulate the air flow which occurs in ventilated rooms and buildings. Only in recent years the three-dimensional geometrical models using a fine grid have made the models more accurate, due to increasing computational power and the theory of turbulence.

CFD computer programs can be used to predict the airflow. The majority of these CFD programs are based on the solution of the Navier-Stokes equations, the energy equation, the mass and concentration equations as well as the transport equations for turbulent viscosity and its scale. CFD tools give a detailed knowledge of the pattern of airflow and the distribution of air velocity and temperature within an enclosed space, so the application of CFD mathematical models have become popular due to its informative results and relatively low labour and equipment costs. The CFD work is performed by using the commercial software FLUENT version 6.1.18, which is a finite volume method (FVM) based code for fluid flow simulations.

The phenomenon of buoyancy driven flow through horizontal openings is an important issue of mass and energy transfer between different zones in buildings. The experimental measurements have been widely used to investigate this highly transient and unstable air flow. However, very few CFD studies have been reported, especially for LES simulations. This chapter will show CFD modelling using both k-ε and LES turbulence models, then the CFD results will be compared with the measurement data. This will be done in order to compare these two different turbulence models. Two ventilation cases are studied: buoyancy driven natural ventilation through a single horizontal opening and buoyancy driven natural ventilation through a large horizontal opening combined with a small vertical opening.

4.2 Turbulence

Air flow in buildings is turbulent. The turbulent flow is characterized by the following properties [34]:

- Turbulent flow is highly unsteady. A plot of the velocity as a function of time appears random of nature.

- Turbulent flow is three-dimensional. The time-averaged velocity may be a function of only two coordinates, but the instantaneous field appears essentially random.
- Turbulent flow contains a great deal of vorticity. Stretching of vortices is one of the principal mechanisms by which the intensity of the turbulence is increased.
- Turbulence increases the rate at which observed quantities are stirred. Stirring is a process in which parcels of fluid with differing concentrations of at least one of the conserved properties are brought into contact. The actual mixing is accomplished by diffusion and this behavior is often called diffusive.
- Turbulence brings fluids of differing momentum content into contact. The reduction of the velocity gradients due to the action of viscosity reduces the kinetic energy of the flow; in other words, mixing is a dissipative process. The lost energy is irreversibly converted into internal energy of the fluid.
- Turbulent flow contains coherent structures – repeatable and essentially deterministic events that are responsible for a large part of the mixing. However, the random part of turbulent flows causes these events to differ from each other in size, strength, and time interval between occurrences, making study of them very difficult.
- Turbulent flow fluctuates on a broad range of length and time scales. This property makes direct numerical simulation of most turbulent flows very difficult.

4.3 Turbulence models

Turbulent flows are characterized by fluctuating velocity fields. These fluctuations mix transported quantities such as momentum, energy, and species concentration, and cause the transported quantities to fluctuate as well. Since these fluctuations can be of small scale and high frequency, they are too computationally expensive to simulate directly in practical engineering calculations. Instead, the instantaneous governing equations can be time-averaged, ensemble-averaged, or otherwise manipulated to remove the small scales, resulting in a modified set of equations that are computationally less expensive to solve. However, the modified equations contain additional unknown variables, and turbulence models are needed to determine these variables in terms of known quantities.

A complete time-dependent solution of the exact Navier-Stokes equations for turbulent flows in complex geometries is unlikely to be attainable for some time to

come. Two alternative methods can be employed to transform the Navier-Stokes equations in such a way that the small-scale turbulent fluctuations do not have to be directly simulated: 'Reynolds averaging' and 'filtering'. Both methods introduce additional terms in the governing equations that need to be modeled in order to achieve 'closure'. Closure implies that there are a sufficient number of equations for all the unknowns.

Since the governing equations of fluid flow are well known and can be seen in many literatures, see [34] [35] [36], the mathematic equations are not described here in detail. However, the important issue in using CFD is the type of turbulence model, where a range of turbulence models can be chosen for varying complexity and accuracy. Thus, it is important to choose the suitable turbulence models for CFD quality control in order to get an understanding of the air flow patterns and turbulence characteristics in ventilated rooms such as air flow through horizontal openings.

4.3.1 Standard k-ε model

Turbulence is an eddying motion that exists at higher Reynolds numbers. Turbulence has a wide spectrum of eddy sizes with a corresponding spectrum of fluctuation frequencies. Turbulence has prevailing rotational motion that can be thought of as a tangle of vortex elements with highly unsteady vorticity vectors that are aligned in all directions. The largest eddies have sizes at the same magnitude as the flow domain, they have low frequencies, and are affected by the boundaries and the mean flow.

The Reynolds-averaged Navier-Stokes (RANS) equations represent transport equations for the mean flow quantities only, with all the scales of the turbulence being modeled. The approach of permitting a solution for the mean flow variables greatly reduces the computational effort. If the mean flow is steady, the governing equations will not contain time derivatives and a steady-state solution can be obtained economically. A computational advantage is seen even in transient situations, since the time step will be determined by the global unsteadiness in the mean flow rather than by the turbulence. The Reynolds-averaged approach is generally adopted for practical engineering calculations, and uses models such as k-ε and its variants, and the Reynolds stress model (RSM).

At present, the most used and popular turbulence model for the prediction of room air flow is the k-ε turbulence model based on time-averaging. The model is based on a transport equation for turbulent kinetic energy k and a transport equation for the dissipation of turbulent kinetic energy ε [37]. An important restriction for the use of k-

ε model is that the solution of the system of equations converges to a 'steady-state' result. Despite the well-known shortcomings of the k-ε model, these numerical solutions often give reasonably good prediction of the overall mean flow pattern. But many problems still occur to study some ventilation phenomena where the air flow situations of interest are transient or dynamic. This situation is a serious drawback for the use of k- ε model.

The standard k- ε model is a two-equation model based on both a transport equation for turbulent kinetic energy k and a transport equation for the dissipation of turbulent kinetic energy ε. The general formulations are shown as follows [38] [39]:

$$\frac{D}{Dt}(\rho k) = D_k + P_k + G_k - \rho\varepsilon$$

$$\frac{D}{Dt}(\rho\varepsilon) = D_\varepsilon + C_1 \frac{\varepsilon}{k}(P_k + G_k) - C_2 \rho \frac{\varepsilon^2}{k}$$

The turbulent viscosity μ_t is obtained from

$$\mu_t = \rho C_\mu \frac{k^2}{\varepsilon}$$

Where k is the turbulent kinetic energy [J/kg]
ε is the rate of dissipation of turbulent kinetic energy [J/kgs]
μ_t is the turbulent viscosity [kg/ms]
D_k is the diffusion term in the k equation
P_k is the production term in the k equation
G_k is the buoyancy term in the k equation
D_ε is the diffusion term in the ε equation
Constant: C_μ=0.09, C_1=1.44, C_2=1.92, σ_k=1.0, σ_ε=1.3

4.3.2 Large Eddy Simulation (LES) with Smagorinsky-Lilly model

Large Eddy Simulation (LES) involves the solution of fully time-dependent and three-dimensional flow fields. The LES flow solutions become physically unstable in the same manner as a real turbulent fluid. The large-scale turbulence is not modeled, and only eddies smaller than the mesh size need to be represented by a so-called subgrid scale model. Therefore, it is important that the grids are fine enough to allow a description of the small eddies. The mean flow quantities predicted from transient

calculations need sufficient time to obtain a steady averaged solution [39] [40]. Thus, the simulations contain the time-dependent evolution of eddies in three dimensions, and the statistics are generated which are difficult to be obtained from traditional methods of turbulence prediction such as *k-ε* model. One weakness of LES is that it is computationally more expensive since the equations have to be solved in time.

In LES model the large eddies are computed in a time-dependent simulation that uses a set of 'filtered' equations. Filtering is essentially a manipulation of the exact Navier-Stokes equations to remove only the eddies that are smaller than the size of the filter, which is usually taken as the mesh size. Like Reynolds averaging, the filtering process creates additional unknown terms that must be modeled in order to achieve closure. Statistics of the mean flow quantities, which are generally of most engineering interest, are gathered during the time-dependent simulation. The attraction of LES is that, by modeling less of the turbulence, the error induced by the turbulence model will be reduced.

With a spatial, inhomogeneous filter (denoted by a bar) applied to the incompressible Navier-Stokes equations, the momentum and continuity equations for the large scale motion can be obtained as:

$$\frac{\partial \bar{u}_i}{\partial t} + \frac{\partial}{\partial x_j}\left(\bar{u}_i \bar{u}_j\right) = -\frac{1}{\rho}\frac{\partial \bar{p}}{\partial x_i} + \mu \frac{\partial^2 \bar{u}_i}{\partial x_j \partial x_j} - \frac{\partial \tau_{ij}}{\partial x_j}$$

$$\frac{\partial \bar{u}_i}{\partial x_i} = 0$$

Where u_i and u_j are the velocity components in the x_i and x_j directions [m/s]
x_i and x_j are the coordinates in i and j directions [m]
t is time [s]
ρ is the density [kg/m^3]
p is the pressure [Pa]
μ is the kinematic viscosity [m^2/s]
τ_{ij} is the subgrid-scale Reynolds stresses [m^2/s^2]

Where the subgrid stresses are given by:

$$\tau_{ij} = \overline{u_i u_j} - \bar{u}_i \bar{u}_j$$

The subgrid-scale stresses resulting from the filtering operation are unknown, and require modeling. The majority of subgrid-scale models in use are eddy viscosity models of the following form:

$$\tau_{ij} - \frac{1}{3}\delta_{ij}\tau_{kk} = -2\mu_t \overline{S}_{ij}$$

Where δ_{ij} is the Kronecker delta, which is defined as having the value 1 when $i=j$, and 0 when $i \neq j$

μ_t is the subgrid-scale turbulent viscosity [m^2/s]

$\overline{S}_{ij}$ is the rate-of-strain tensor for the resolved scale [1/s]

Where $\overline{S}_{ij}$ defined by

$$\overline{S}_{ij} = \frac{1}{2}\left(\frac{\partial \overline{u}_i}{\partial x_j} + \frac{\partial \overline{u}_j}{\partial x_i} \right)$$

The most basic of subgrid-scale models was proposed by Smagorinsky [41] and further developed by Lilly [42]. In the Smagorinsky-Lilly model, the eddy viscosity is modeled by

$$\mu_t = (C_S \Delta)^2 \sqrt{2\overline{S}_{ij}\overline{S}_{ij}}$$

Where C_S is the Smagorinsky constant

Δ is the grid filter width [m]

The filter-width Δ is taken as the local grid size:

$$\Delta = \left(\Delta_{x,i}\Delta_{y,j}\Delta_{z,k}\right)^{1/3} = \left(\Delta V_{ijk}\right)^{1/3}$$

Where indices i, j, k are cell-index in the three coordinate directions

ΔV_{ijk} is the volume of the computational cell i, j, k

In the literature, the constant is found to vary in the range from C_S=0.065 [43] to C_S=0.25 [44]. Lilly derived a value of 0.23 for C_S from homogeneous isotropic turbulence in the inertial subrange. However, this value is found to cause excessive

damping of large-scale fluctuations in the presence of mean shear or in transitional flows. C_S=0.1 has been found to yield the best results for a wide range of flows, and is the default value in FLUENT.

4.4 Modeling

4.4.1 Introduction

Two cases of the buoyancy driven natural ventilation are simulated: (A) single-sided one horizontal opening and (B) a large horizontal opening combined with a small vertical opening. In the case A, a square horizontal opening is placed at the roof center of the test room. In the case B, a square horizontal opening is placed at the roof center of the test room, and another square vertical opening is located at the center of the bottom of a test room's side wall.

Two three-dimensional turbulence models of standard k-ε model and LES model are utilized. Only a part of the geometry, including the entire test room and a part of the thermostatic chamber adjacent to the test room, is simulated in order to get much fine grid in the numerical model. Figure 4.1 shows the CFD geometry with one horizontal opening, and Figure 4.2 shows the CFD geometry with one horizontal opening combined with one vertical opening. The wall in blue colour represents the inlet of cool air from ventilation system, the two openings in red colour represent the outlets of the ventilation system, and the square openings in black colour represent the openings investigated.

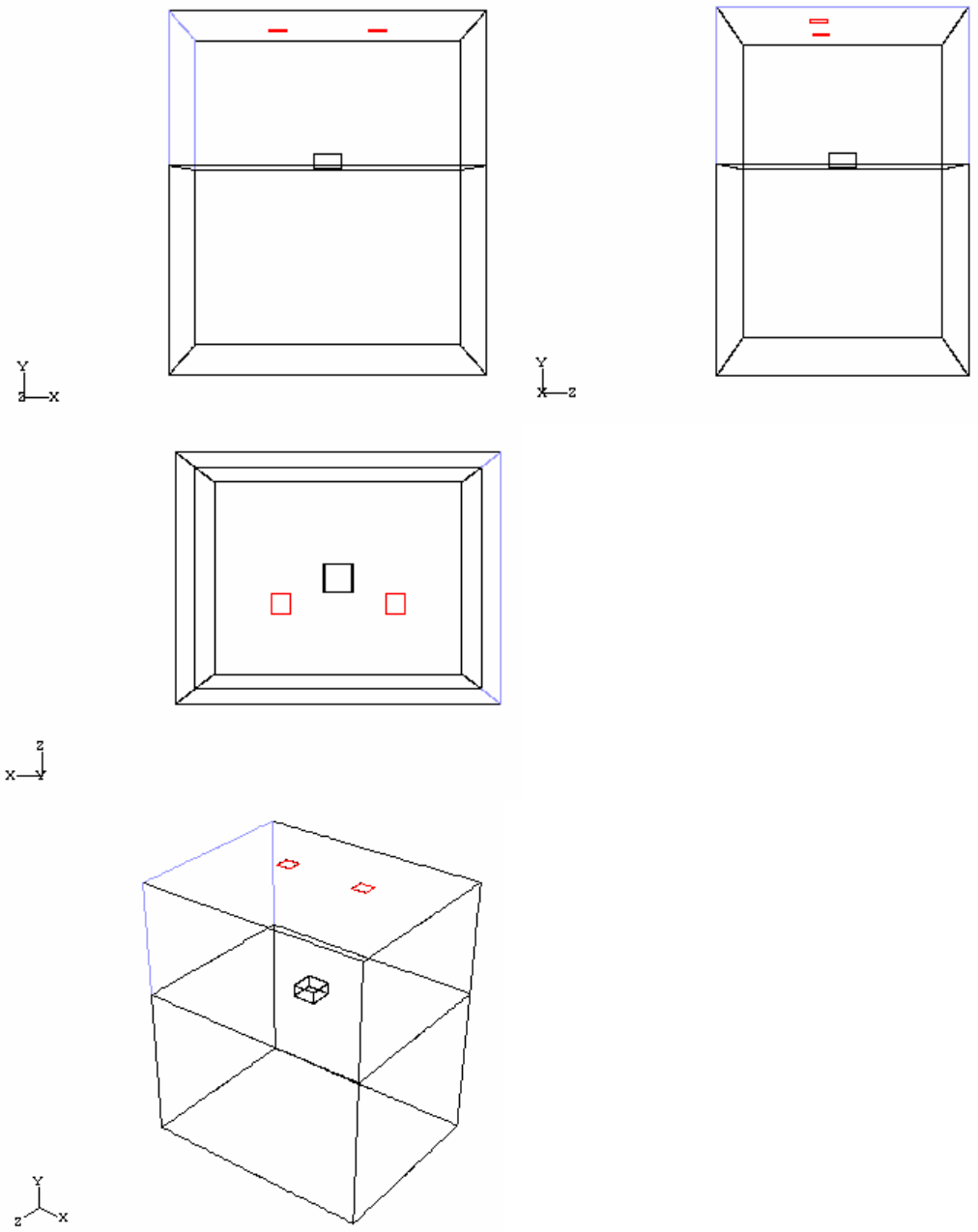

Figure 4.1: The CFD geometry with one horizontal opening of side length *S*=0.4m and height *L*=0.2m.

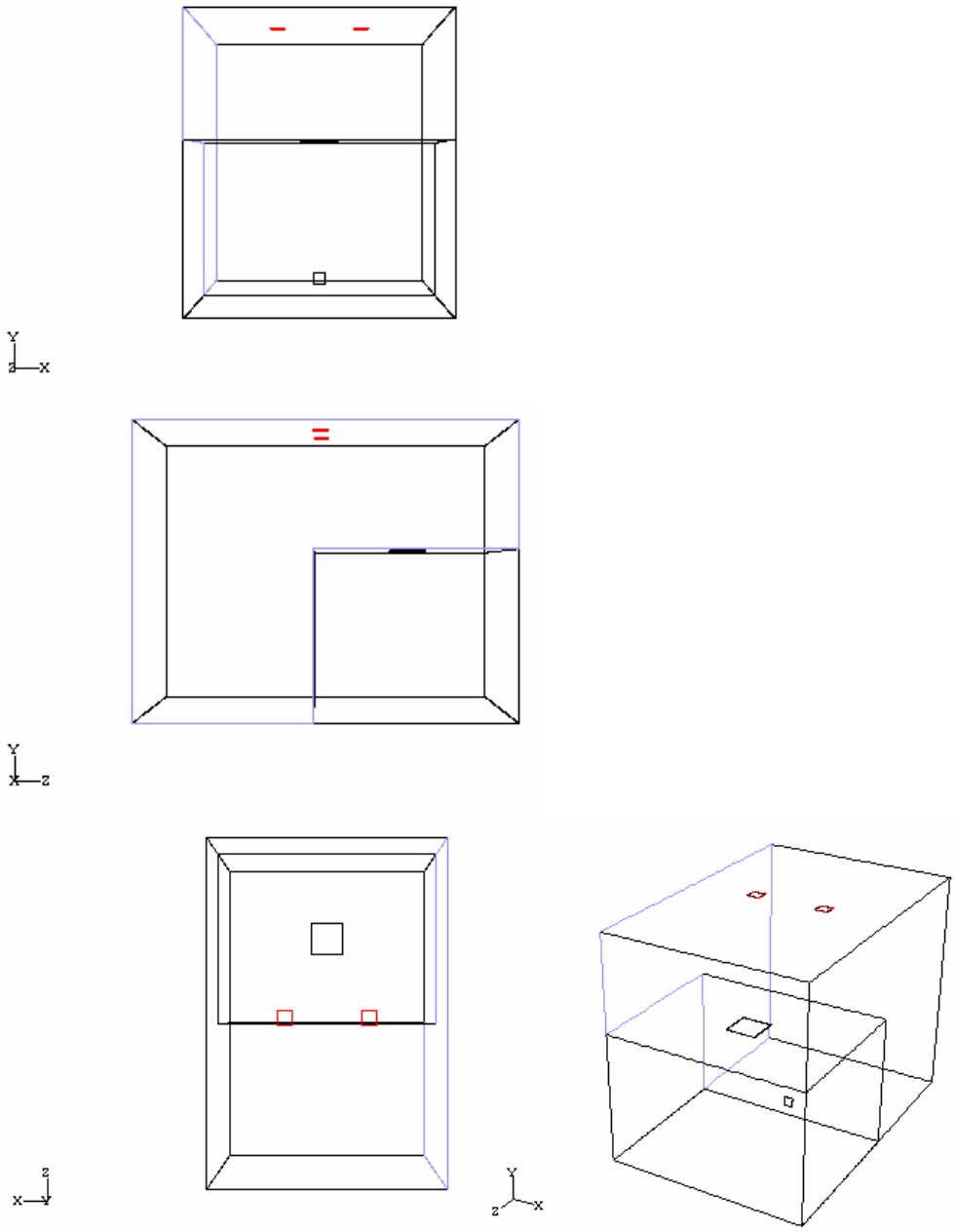

Figure 4.2: The CFD geometry with one horizontal opening *S*=0.6m combined with one vertical opening *S*=0.2m.

4.4.2 Key parameters of buoyancy driven natural ventilation

When heat is added to air and the air density varies with temperature, the air flow can be induced due to the force of gravity acting on the density variations. This kind of natural-convection air flow can be modeled by FLUENT. Archimedes number *Ar* is the ratio of buoyancy force to inertial forces, and this ratio is proportional to the ratio

of buoyancy to momentum forces as well. *Ar* can be calculated by the ratio of the Grashof number *Gr* and Reynolds number *Re*:

$$Gr = \frac{g\beta\Delta TL^3}{\upsilon^2}$$

$$\mathrm{Re} = \frac{UL}{\upsilon}$$

$$Ar = \frac{Gr}{\mathrm{Re}^2} = \frac{g\beta\Delta TL}{U^2}$$

Where *Gr* is the Grashof number
Re is the Reynolds number
Ar is the Archimedes number
g is the gravitational acceleration [m/s^2]
β is the thermal expansion coefficient [1/K]
ΔT is the temperature difference [K]
L is the characteristic length [m]
v is the kinematic viscosity [m^2/s]
U is the air velocity [m/s]

And the thermal expansion coefficient β:

$$\beta = -\frac{1}{\rho}\frac{\partial\rho}{\partial T}$$

When the Archimedes number approaches or exceeds unity, a strong buoyancy contribution to the air flow is expected. In pure natural convection, the strength of the buoyancy-induced flow is measured by the Rayleigh number:

$$Ra = \frac{g\beta\Delta TL^3}{\upsilon\alpha}$$

Where α is the thermal diffusivity [m^2/s]:

$$\alpha = \frac{k}{\rho c_p}$$

Where k is the thermal conductivity [W/mK]
c_p is the heat capacity [J/kgK]

Rayleigh numbers less than 10^8 indicate a buoyancy-induced laminar flow, with transition to turbulence occurring over the range of $10^8<Ra<10^{10}$.

4.4.3 The Boussinesq model

In order to get faster convergence in natural convection flow, the Boussinesq model is usually used. This approximation treats density as a constant value in all solved equations, except for the buoyancy term in the momentum equation:

$$(\rho - \rho_0)g \cong -\rho_0 \beta (T - T_0)g$$

Where ρ_0 is the (constant) density of the flow [kg/m^3]
T_0 is the operating temperature [K]

Then, this equation can be obtained

$$\rho = \rho_0 (1 - \beta \Delta T)$$

to eliminate ρ from the buoyancy term. This approximation is accurate as long as changes in actual density are small.
In flows accompanied by heat transfer, the fluid properties are normally functions of temperature. The Boussinesq approximation introduces errors of the order of only 1% if the temperature differences are below 15°C for air [34]. Therefore, it is important to use the Boussinesq model to calculate time-dependent natural convection inside a closed domain. This model can also be used for steady-state problems, provided that changes in temperature are small.

4.5 Quality control of CFD

CFD simulation is used to predict air movement and distributions of temperature and velocity in this study. In order to improve the quality of CFD calculations, i.e. to make calculations with sufficient accuracy, several important issues should be considered carefully for both the governing equations and the computation [39]. The governing equations consider the selection of governing equations for the solution of a given problem, including boundary conditions, turbulence model, empirical relations and physical properties. The computation considers the selection of methods required to

solve the governing equations, including differencing schemes, computational grids and convergence errors.

4.5.1 CFD simulations of standard *k-ε* model with standard wall function

The governing equations solved by FLUENT include the three-dimensional time-dependent (or steady-state) incompressible Navier-Stokes equations and *k-ε* turbulence equations. For the *k-ε* turbulence equations, the empirical turbulence coefficients C_1, C_2, C_μ, σ_k and σ_ε are assigned the following values: C_1=1.44, C_2=1.92, C_μ=0.09, σ_k=1.0 and σ_ε=1.3. These values are widely accepted in CFD *k-ε* calculations. The pressure-velocity coupling is achieved using the PISO (Pressure Implicit with Splitting of Operators) [45] algorithm. The second-order upwind differencing scheme is used to evaluate the convection terms for the Navier-Stokes equations, the energy equation and the turbulent transport equation, in order to reduce numerical diffusion.

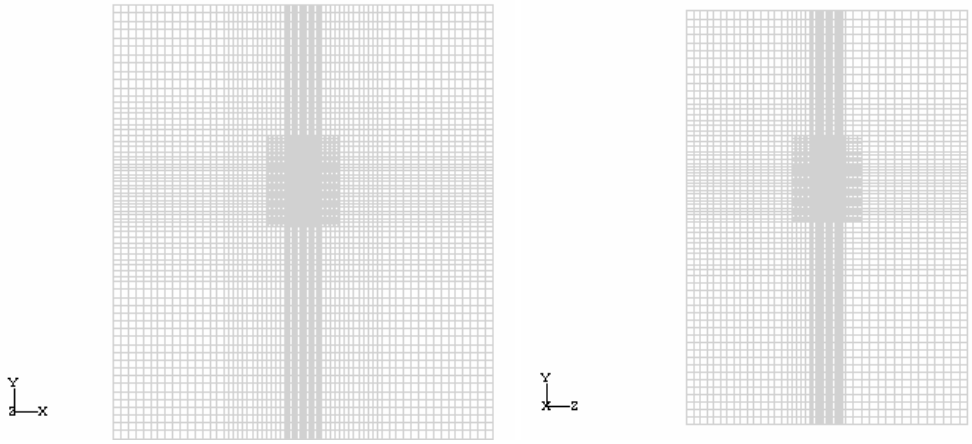

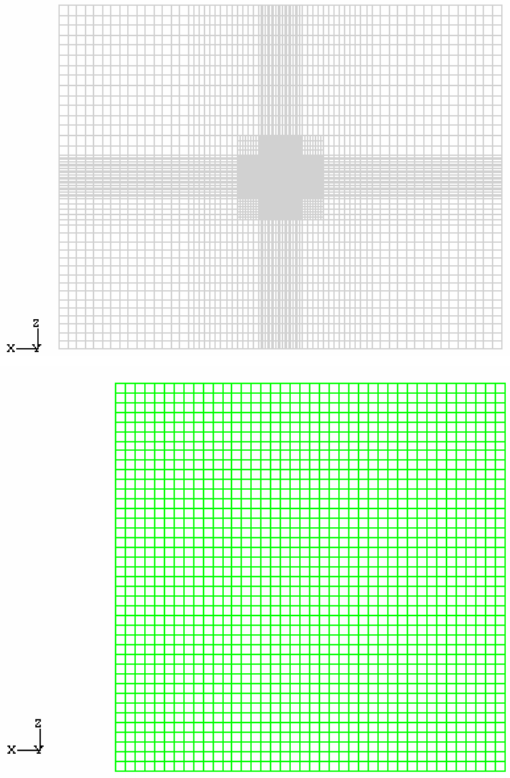

Figure 4.3: The grids of the case with one horizontal opening of side length S=0.4m and height L=0.2m. The grids of three center planes through the opening in x, y, z directions are in grey colour, and the grid of the horizontal opening are in green colour.

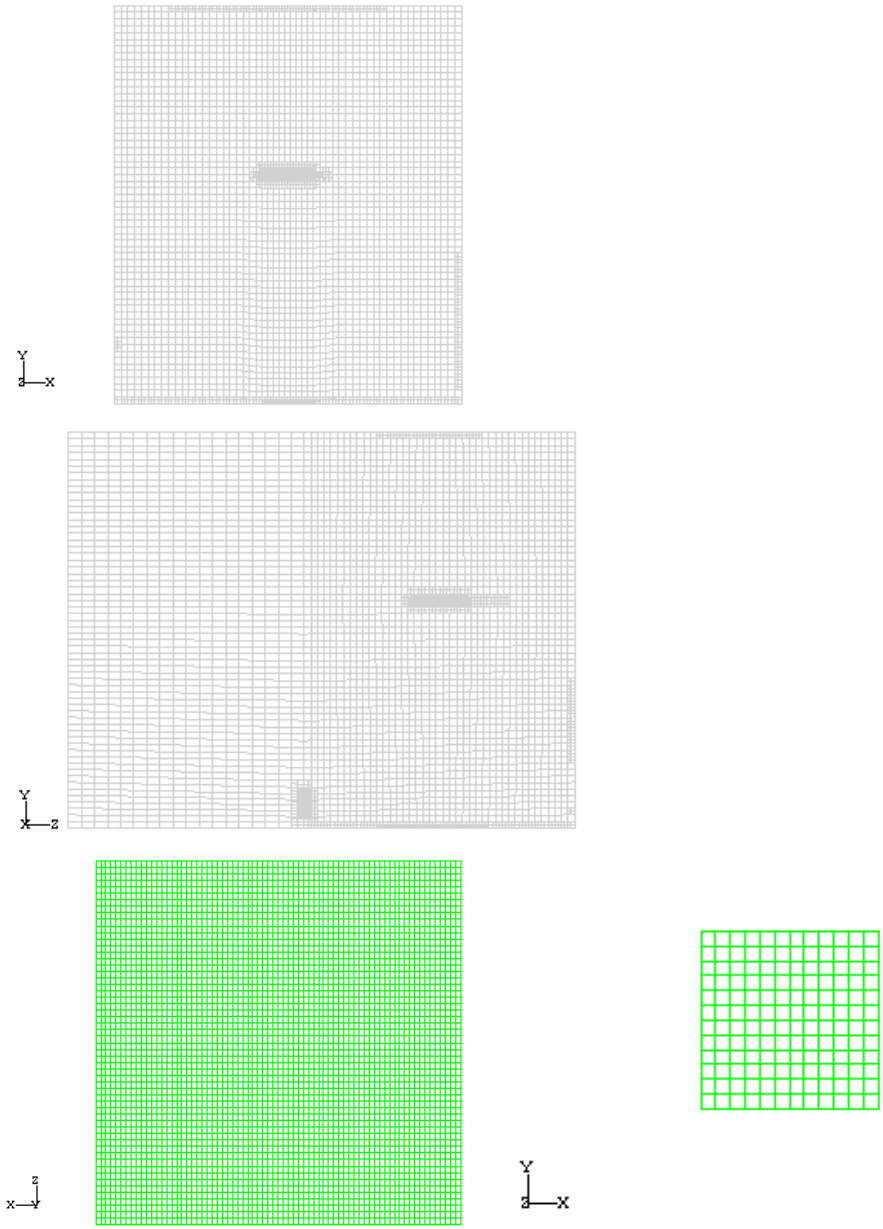

Figure 4.4: The grids of the case with one horizontal opening S=0.6m combined with one vertical opening S=0.2m. The grids of two center planes through the two openings in x, y, z directions are in grey colour, and the grid of the horizontal opening (left) and the vertical opening (right) are in green colour.

The grid for the simulations consisted of approximately 400,000 – 600,000 computational grids in all simulation cases, where high density grids are refined in the field around the horizontal opening and the vertical opening, see Figure 4.3 and Figure 4.4. The grid independences have been investigated to assess the optimum

number of grids for all the simulations including k-ε and LES modeling. The calculated air flow rate value do seem to reach an asymptotical solution for all simulation cases, and the air flow rate value has only small and insignificant changes for further grid refinements in the numerical results. However, when the grid number is below approximate 150,000 the results change dramatically.

The standard wall functions approach is used in the k-ε turbulence model. A specified constant heat flux 20W/m^2 through the test room floor is given to model the uniformly distributed heat source, and all the other walls are set to be adiabatic. The inlet air boundary conditions of the thermostatic chamber are (given by measurement data): velocity 0.015m/s with normal direction to boundary, temperature 10ºC, turbulence intensity 30% and turbulence length scale 0.1m [46].

For the unsteady k-ε model CFD simulations, the first-order implicit unsteady formulation is used. Since the FLUENT formulation is fully implicit, there is no stability criterion that needs to be met in determining the time step Δt. However, to model transient phenomena properly, it is necessary to set Δt at least one order of magnitude smaller than the smallest time constant in the system being modeled. Thus, a good way to choose the Δt is that the time step size Δt is set to be a proper value and the number of iterations converges to 10^{-3} at each time step. Therefore, the number of iterations per time step is chosen to be 10 - 20.

4.5.2 CFD simulations of LES model with Smagorinsky-Lilly model

The Samgorinsky-Lilly model can be utilized in FLUENT (Smagorinsky 1963, Lilly 1966), where this model has a constant model coefficient C_s. The default value C_s=0.1 is used in LES simulations. The second-order central differencing scheme is used to discretize the convection terms. The pressure-velocity coupling is achieved using the PISO. The grid used in the LES simulations is the same with the grid used in k-ε simulations, since the grid independence has been investigated also for LES modeling. Thus, the initial field of the LES can be obtained from the results of the k-ε simulation. The boundary conditions are similar with those used in the k-ε model.

For the LES simulations, the second-order implicit unsteady formulation is used. The time step size Δt is set to be a proper value and the number of iterations converges to 10^{-3} at each time step. The number of iterations per time step is 10 - 20. Since the LES runs a transient solution from the initial condition from the k-ε model results, the simulation must be run long enough to reach independence of the initial condition and to enable the statistics of the flow field.

5 Experimental and numerical analysis of buoyancy driven natural ventilation through one horizontal opening

5.1 Measurement results

5.1.1 Smoke visualization

The lower temperature air above the opening has a higher density and the higher temperature air below the opening has a lower density. The density difference makes buoyancy driven downflow of the heavier air from the upper thermostatic chamber to the lower test room. Since the test room is sealed, mass conservation dictates upflow of the lighter air. In the case of a single opening, this situation gives rise to bidirectional exchange flow across the horizontal opening.

In order to get a better understanding of this bidirectional flow, smoke visualizations are carried out. The air flow pattern in steady state near the opening is observed during the experiment. The smoke is introduced in the thermostatic chamber or in the test room, thus the downflow or upflow can be observed. Figure 5.1 shows the resulting downflow through the opening S=0.4m and L/D=0.295 at time t=0s, 0.5s, 1s, 1.5s, 2.5s and 3.5s, respectively. The air velocity and airflow directions vary all the time through different part of the opening. The smoke visualizations show that the bidirectional air flow is highly transient, unstable and complex. In the full-scale airflow measurements, it is difficult to observe the flow pattern differences for different flow regimes by means of smoke visualization.

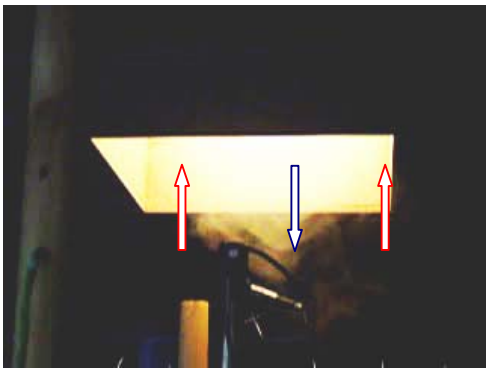

Figure 5.1(A)

Figure 5.1(B)

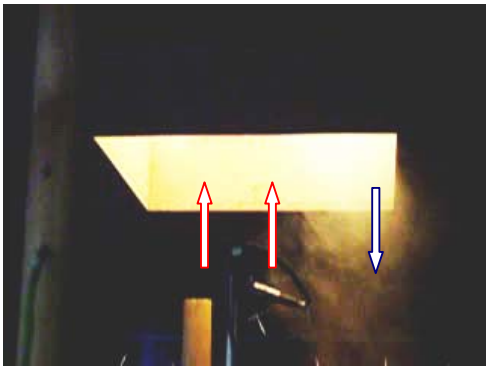

Figure 5.1(C)

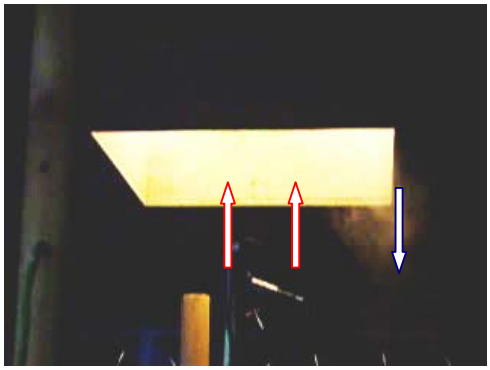

Figure 5.1(D)

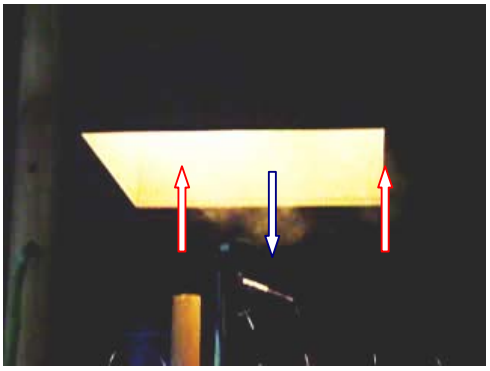

Figure 5.1(E)

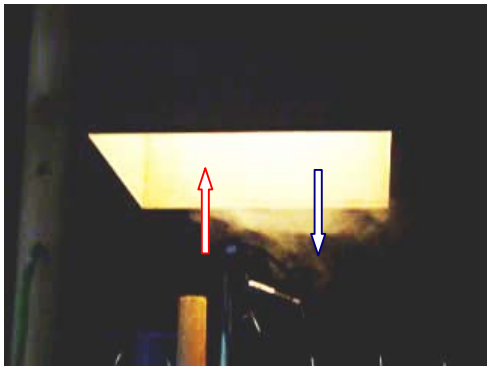

Figure 5.1(F)

Figure 5.1: The smoke visualization of air downflow through the opening S=0.4m and L/D=0.295 at different time, (A) t=0s, (B) t=0.5s, (C) t=1s, (D) t=1.5s, (E) t=2.5s and (F) t=3.5s.

5.1.2 LDV velocity measurement

Vertical velocity component measurements are performed using Laser Doppler Velocimetry (model: Dantec Flowlite laser-optics system). The experiment is made

several times at different points at the opening for one case keeping constant temperature difference, since this LDV instrument made velocity measurement only one point and one velocity component once. Figure 5.2(A) presents the typical vertical velocity history during about 1000 seconds at the center point of the opening for case S=1.0m, L/D=0.115, at temperature difference ΔT=9.6°C.

LDV measurements confirm the qualitative flow patterns given by flow visualization, which means, the bidirectional flow is highly transient. The vertical velocity at one point varies quickly between positive (upflow) and negative (downflow). In Figure 5.2(A), the vertical velocity component varies between -0.3m/s and 0.35m/s. As a result the vertical component of flow measured by LDV can state the bidirectional flow motion and the spectral analysis of flow. The mean air speed in the vertical component is 0.120m/s during this time period. If using this air speed as the mean air vertical speed of the opening, the calculated air flow rate is 215m^3/h, but the measured data is 129m^3/h. The large difference states that one point's velocity can not be used as the mean velocity of the opening, since the air speed distribution over the entire opening are quite complex.

The frequency of pulsations is measured from the power spectrum of LDV data. Figure 5.2(B) shows the corresponding spectrum at this center point, but a clearly defined frequency can not be identified from the spectrum for this L/D aspect ratio. Figure 5.2(C) and Figure 5.2(D) show the vertical velocity history and spectrum analysis at this center point for the same case at the higher temperature difference ΔT=15.0°C. The higher temperature difference results in larger velocity variations between -0.47m/s and 0.45m/s, and the mean speed is 0.149m/s. Similarly, Figure 5.2(E) and Figure 5.2(F) show the vertical velocity history and spectrum analysis at this center point for the same case at lower temperature difference ΔT=6.1°C. The lower temperature difference results in small velocity variations between -0.26m/s and 0.26m/s, and the mean speed is 0.093m/s.

Figure 5.3(A) and Figure5.3(B) presents the typical vertical velocity history and spectrum analysis during about 1000 seconds at the center point 6cm below the opening for case S=0.4m, L/D=0.295, at temperature difference ΔT=11.7°C. The vertical component of velocity varies between -0.44m/s and 0.26m/s, and the mean value is 0.089m/s.

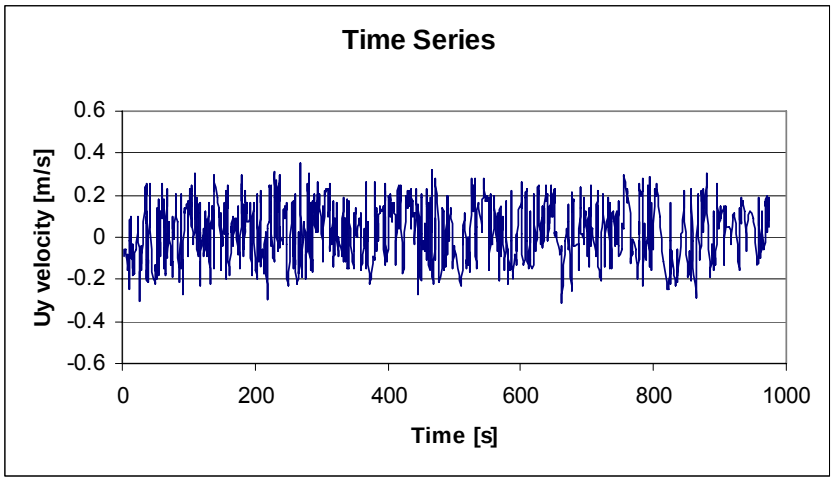

Figure 5.2(A): The vertical velocity history at the center point of the opening S=1.0m, L/D=0.115, at temperature difference ΔT=9.6°C.

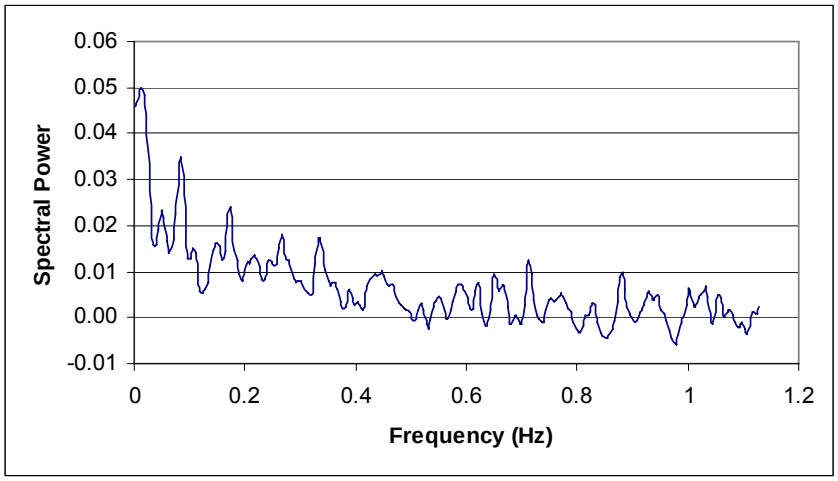

Figure 5.2(B): The corresponding spectrum at the center point of the opening S=1.0m, L/D=0.115, at temperature difference ΔT=9.6°C.

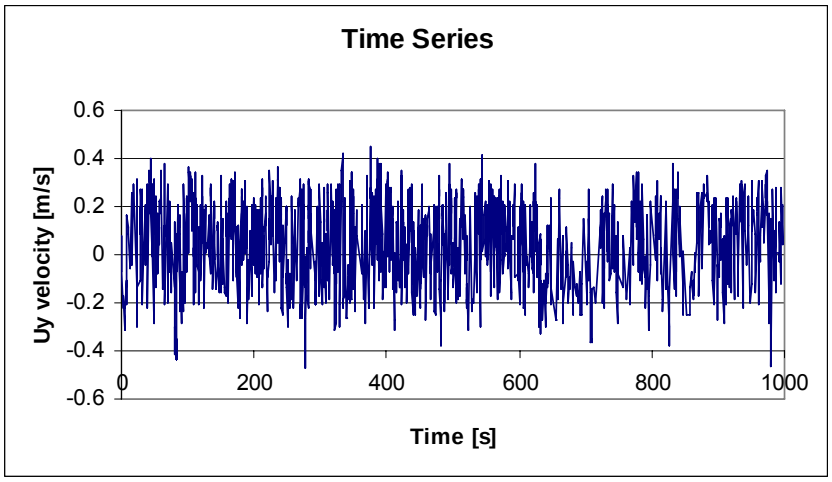

Figure 5.2(C): The vertical velocity history at the center point of the opening S=1.0m, L/D=0.115, at temperature difference ΔT=15.0°C.

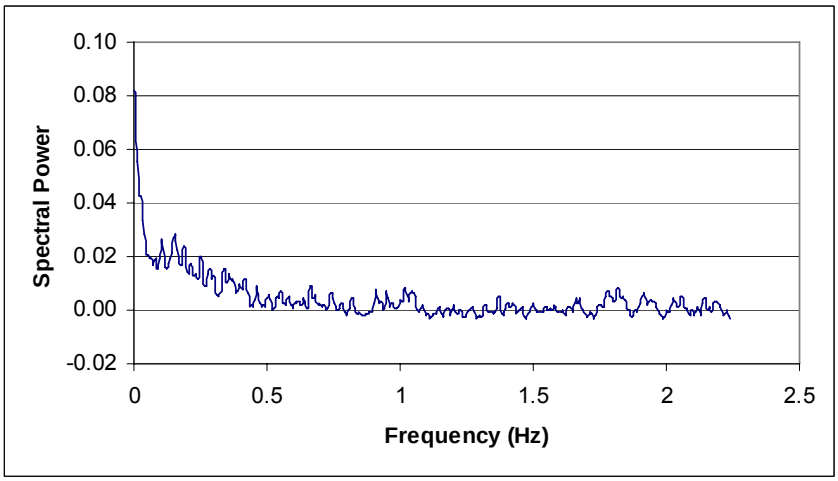

Figure 5.2(D): The corresponding spectrum at the center point of the opening S=1.0m, L/D=0.115, at temperature difference ΔT=15.0°C.

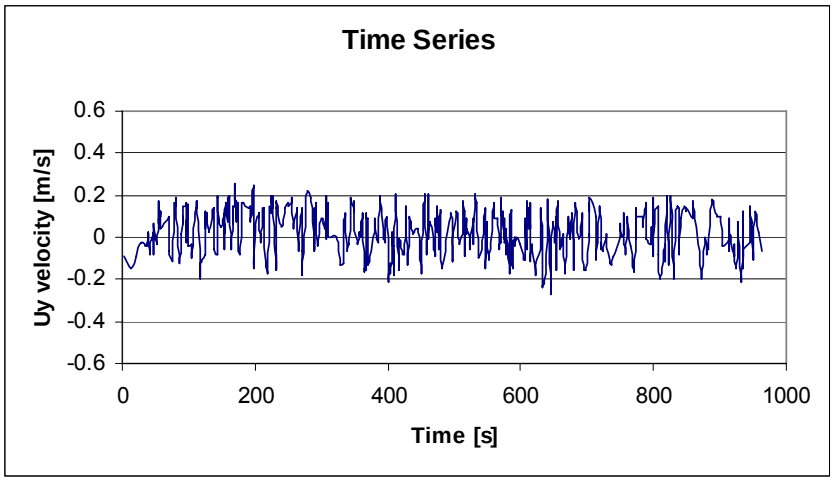

Figure 5.2(E): The vertical velocity history at the center point of the opening S=1.0m, L/D=0.115, at temperature difference ΔT=6.1°C.

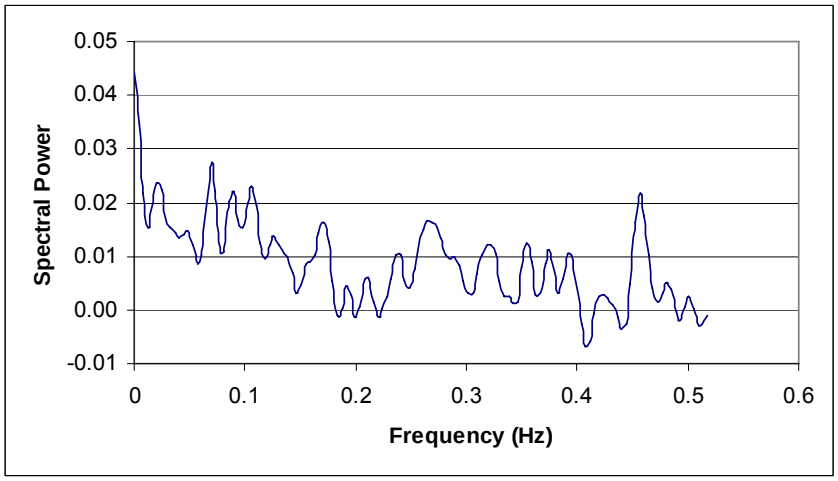

Figure 5.2(F): The corresponding spectrum at the center point of the opening S=1.0m, L/D=0.115, at temperature difference ΔT=6.1°C.

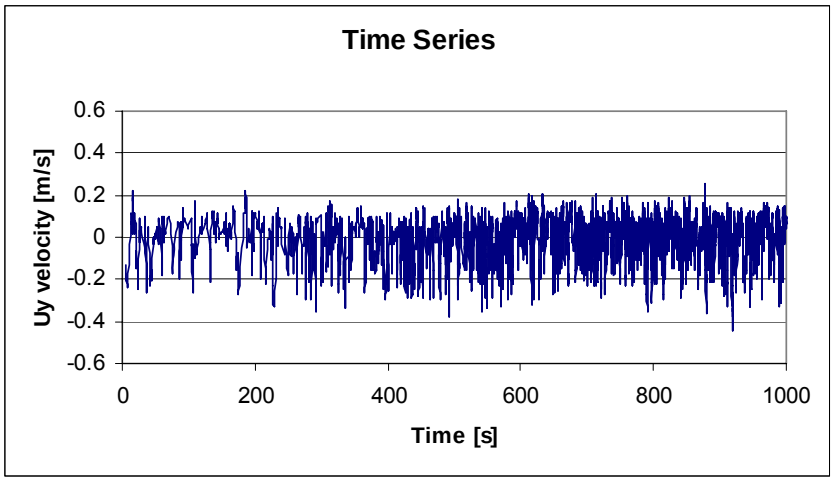

Figure 5.3(A): The vertical velocity history at the center point 6cm below the opening for case S=0.4m, L/D=0.295, at temperature difference ΔT=11.7°C.

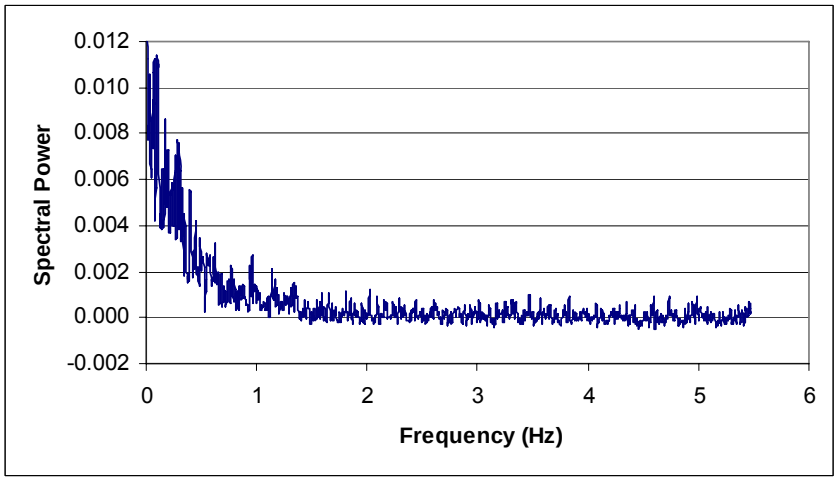

Figure 5.3(B): The corresponding spectrum at the center point 6cm below the opening for case S=0.4m, L/D=0.295, at temperature difference ΔT=11.7°C.

5.1.3 DANTEC 54R10 measurement

The Dantec low velocity measurement system is used to measure the air velocity magnitude inside the test room. The sample time is two minutes, and it does not give clear air velocity curve for each measure point. Nevertheless, the interesting thing of this measurement is to give the velocity magnitude, as an example, see the Figure 5.4 and Figure 5.5. Figure 5.4 shows the air speed measurement just below the opening of S=0.8m and L/D=0.443 at ΔT=18.2°C. The air speeds vary between about 0.2m/s to 0.5m/s. In the same condition, the air speeds in the center vertical column vary between about 0.3m/s to 0.7m/s, shown in Figure 5.5, and the sensors' position can be seen in Figure 3.5.

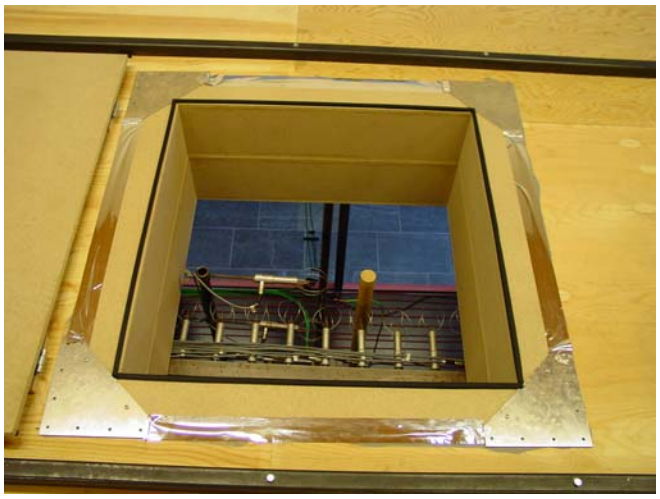

Figure 5.4(A): The air speed measurement just below the opening (sensors' numbers x=0m to x=0.8m are from left to right).

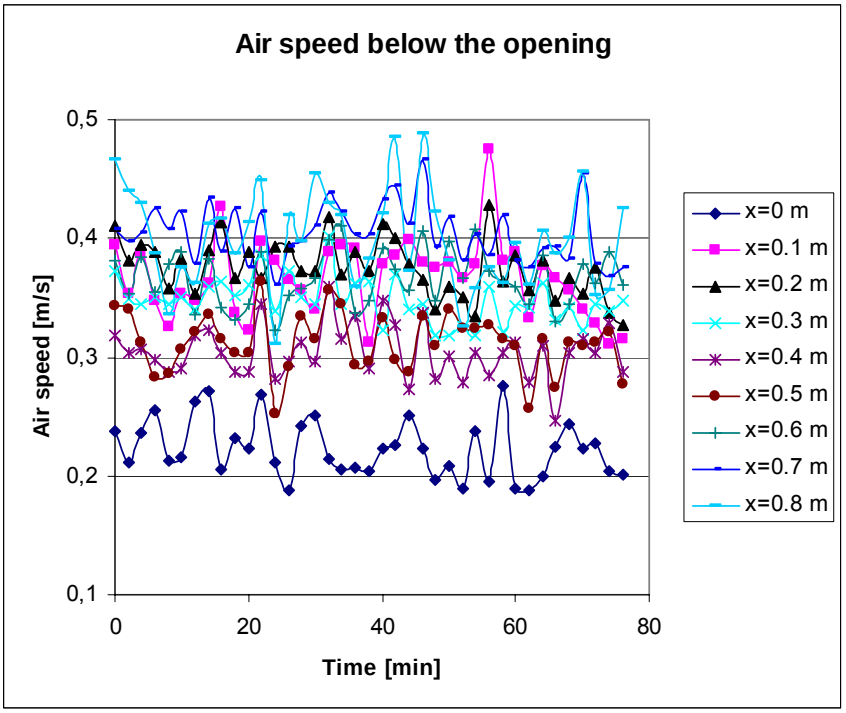

Figure 5.4(B): The air speed history below the opening of 9 sensors.

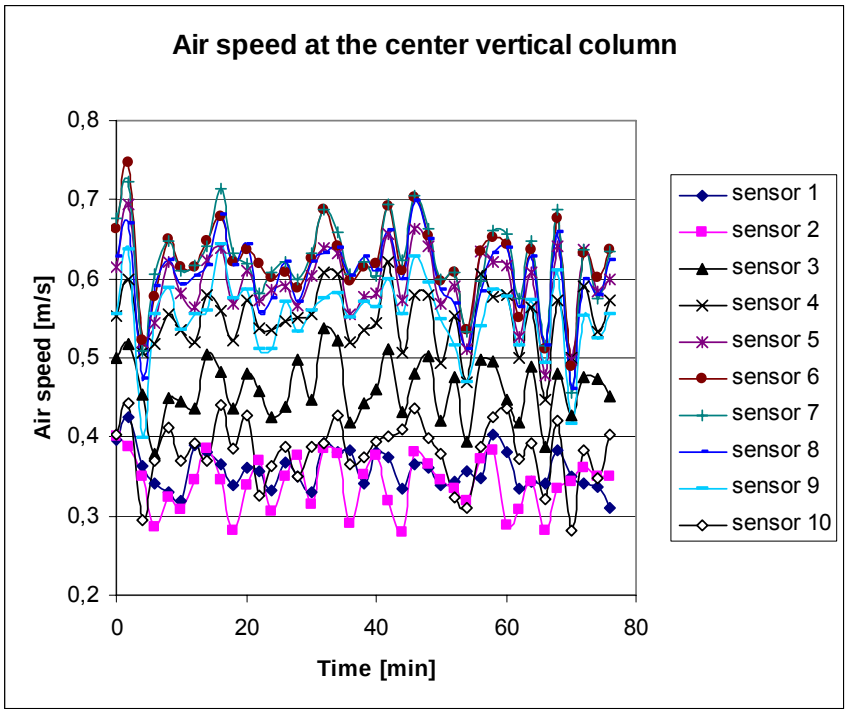

Figure 5.5: The air speed history at the center vertical column of 10 sensors.

5.1.4 Temperature gradient measurement

In a naturally ventilated room, the temperature gradient is an interesting issue which is influenced by the ventilation system. The temperature gradient is an important factor for the use of ventilation system because it influences thermal comfort in a room.

In order to see the transient phenomenon, Figure 5.6 shows two temperature histories of the sensor at the highest measured point y=2.35m below the opening. The temperatures may change more than 2°C during the measurements. In order to compare the temperature gradient between different opening ratio cases, the 10 point's temperature value has been measured in the center line of the test room at height 0.04m, 0.1m, 0.2m, 0.4m, 0.6m, 0.85m, 1.1m, 1.35m, 1.7m and 2.35m. Figure 5.7 shows the dimensionless temperature difference gradients $\Delta T / \overline{\Delta T}$ in the center line of the test room of 5 cases with the same side length of horizontal opening S=0.8m, and different heights L=0.133m, 0.4m, 0.6m, 0.8m and 1m (i.e. L/D=0.147, 0.443, 0.665, 0.887 and 1.108). The temperatures are calculated as the average value of the steady state flow during the measurement time. The ΔT is the temperature difference between the indoor temperature at the measured point and outdoor mean temperature, and $\overline{\Delta T}$ is the temperature difference between the mean indoor temperature and outdoor temperature. It can be seen clearly that the cooled air

downflow gives rise to negative temperature gradient from a certain height, where this height is influenced by air flow rate. For the case of *L/D*=0.147, the air flow rate is quite low compared with other cases, thus the position of this temperature gradient changing point is much higher than other cases.

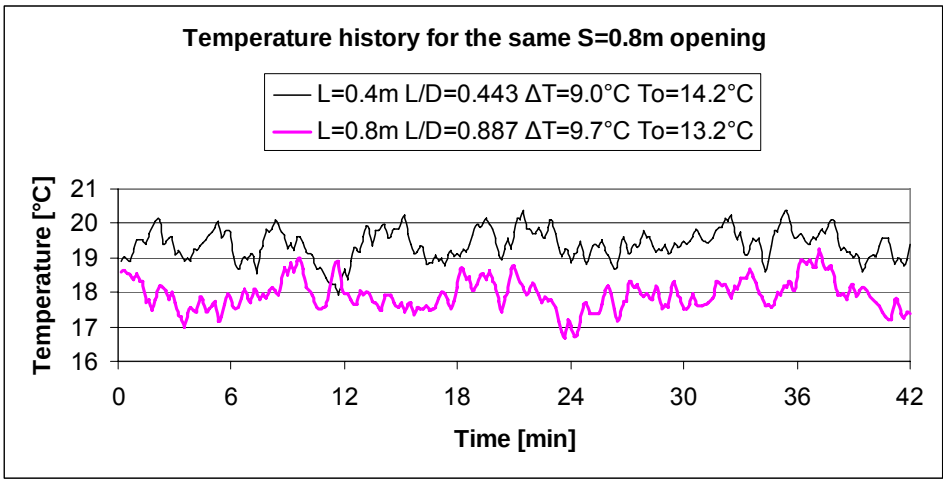

Figure 5.6: The temperature history of the sensor at the highest measured point y=2.35m below the opening.

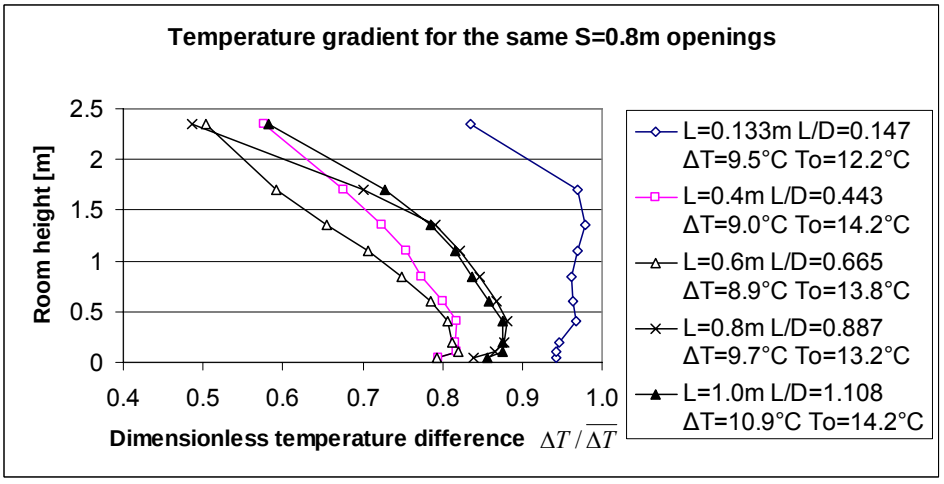

Figure 5.7: The dimensionless temperature difference gradients in the center line of the test room with the same side length of horizontal opening *S*=0.8m.

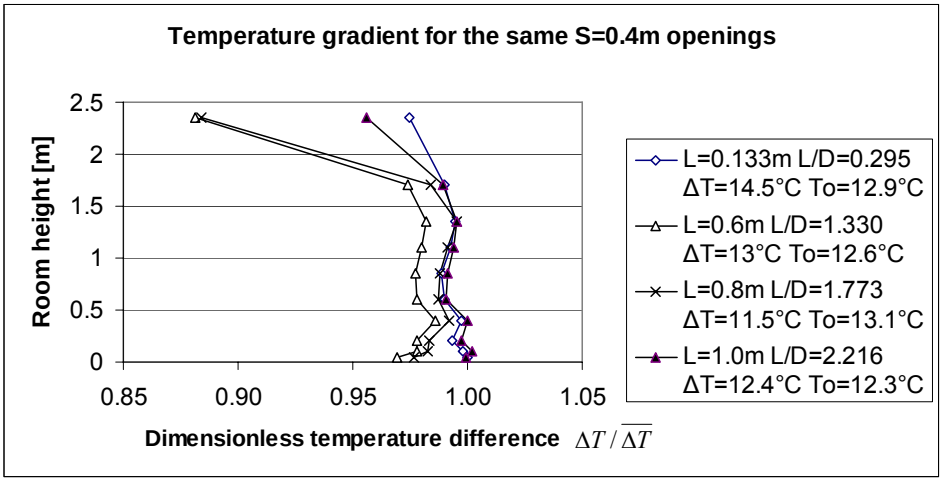

Figure 5.8: The dimensionless temperature gradients in the center line of the test room with the same side length of horizontal opening S=0.4m.

Similarly, Figure 5.8 shows the dimensionless temperature difference gradients $\Delta T / \overline{\Delta T}$ in the center line of the test room of 4 cases with the same side length of horizontal opening S=0.4m, and different heights L=0.133m, 0.6m, 0.8m and 1m (i.e. L/D=0.295, 1.330, 1.773 and 2.216). The temperature gradient has the same tendency as the case S=0.8m, but the position of the changing point is higher than the case S=0.8m, because of the lower air flow rate in these cases.

5.1.5 Air flow rate at different openings and *L/D*

Since the air flow across the opening is time-dependent, the air flow rates will oscillate with time. Therefore, the measured air flow rate should be the mean value of the steady state flow. Because the air exchange rate is small (or time constant quite large) for the test room to actually measure a reliable average value, this value for each measuring case must be demonstrated that the average value has been measured. For different measurement cases of opening size, the injection period of CO_2 tracer gas varies from 2 hours to 2 days depending on the air flow rate value through the opening. Figure 5.9 shows the CO_2 concentration history at the center point of the test room during the measurement case S=0.8m, L/D=0.147, at temperature difference ΔT=18.7°C. It can be seen clearly the fluctuation of CO_2 concentration with time. In the case of one horizontal opening, the fluctuation is not large.

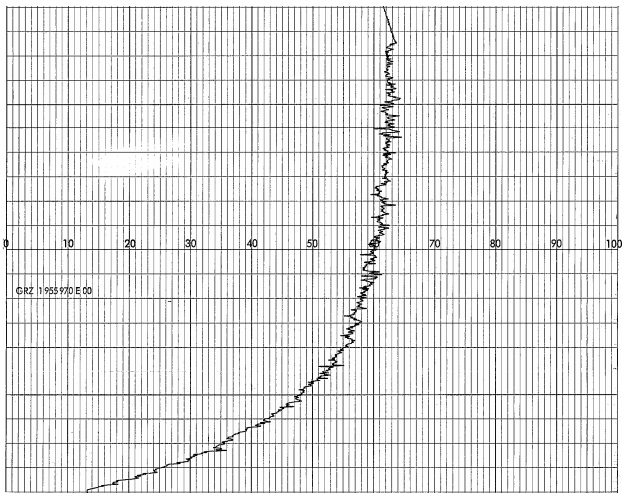

Figure 5.9: The CO_2 concentration history at the center point of the test room for case S=0.8m, L/D=0.147 and ΔT=18.7°C. The horizontal axis records the CO_2 concentration value [ppm], and the vertical axis records the time [min].

Figure 5.10(A) to 5.10(E) show the comparisons of air flow rate versus temperature difference in different flow regimes between the measured data and the calculated data from Epstein's formula. The air flow rate increases with the temperature difference for a certain opening because of higher buoyancy driven force. Generally, the absolute deviations between the measured data and the Epstein's formula data increase when the temperature difference increases, but the relative deviations are almost the same. The air flow rate also changes significantly in the horizontal openings with different L/D ratio. In some cases the measured air flow rate fits quite well with the Epstein's formula, such as the case of L/D=0.147, S= 0.8m in flow Regime I and the case of L/D=0.295, S=0.4m in flow Regime II; but in some cases the measured data show clear deviations with the Epstein's formula, such as the case of L/D=1.108, S=0.8m and the case of L/D=1.773, S=0.4m in flow Regime III. For example in Figure 5.10(C), the flow rates estimated by Epstein formula have no significant differences when L/D ranged from 0.443 to 1.108, but the experimental measurement indicates that the air flow rates vary significantly at these L/D ratios. At temperature difference 10°C, the air flow rates are 127.5, 136.6, 125.4 and 107.3m^3/h for the experimental measurements corresponding to the L/D ratios of 0.443, 0.665, 0.887 and 1.108, but the air flow rates are 149.7, 149.6, 149.0 and 147.6m^3/h for Epstein formula estimation corresponding to these L/D ratios. Here the Epstein formula overestimates the air flow rate for these L/D value of the opening S=0.8m.

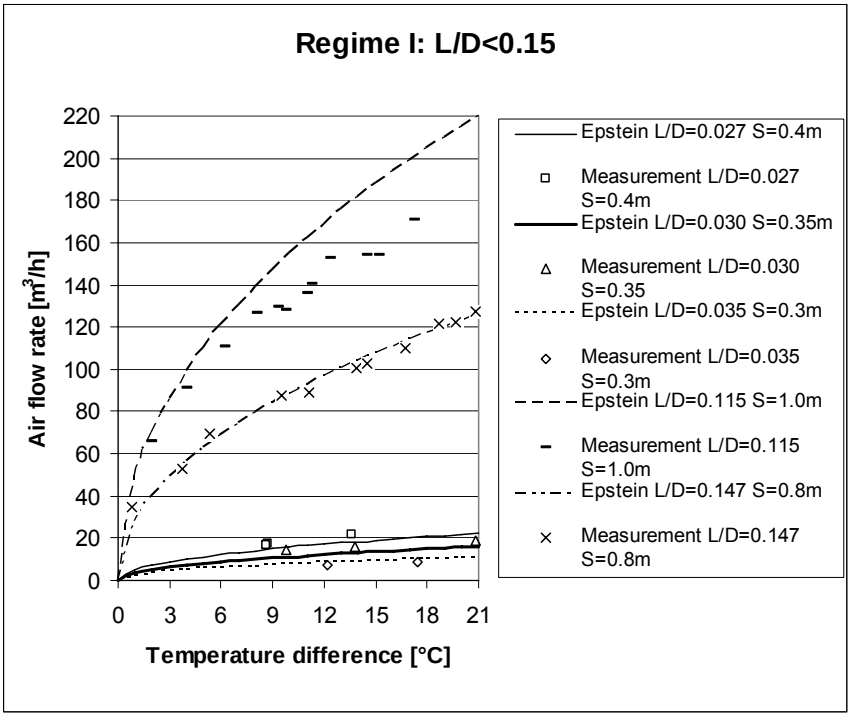

Figure 5.10(A)

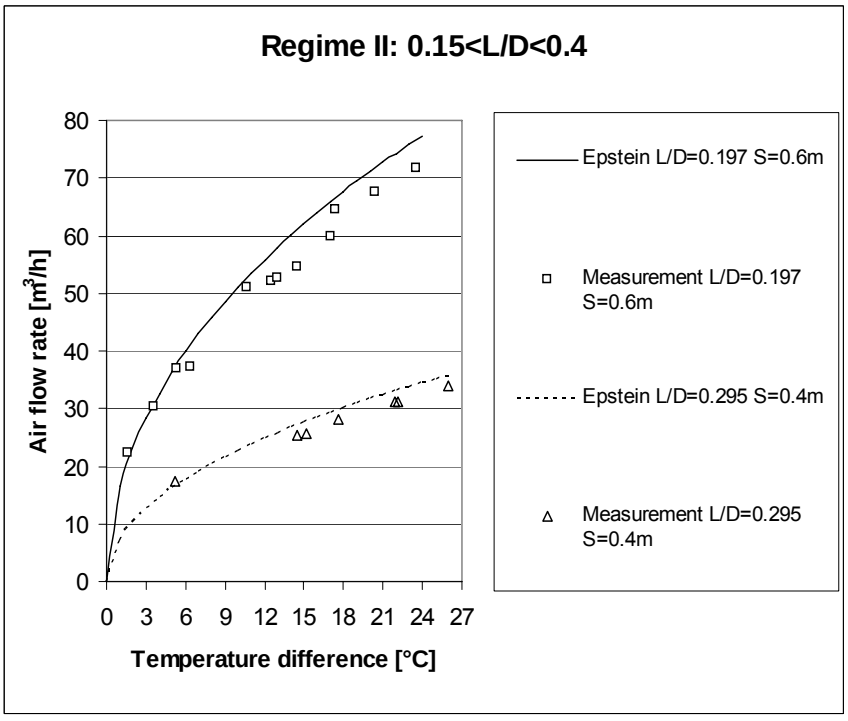

Figure 5.10(B)

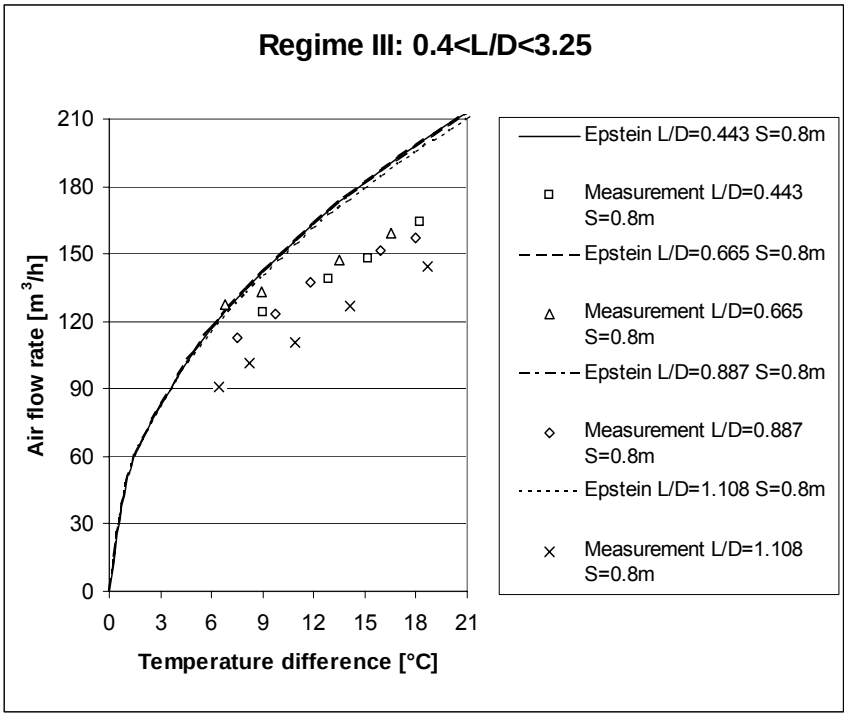

Figure 5.10(C)

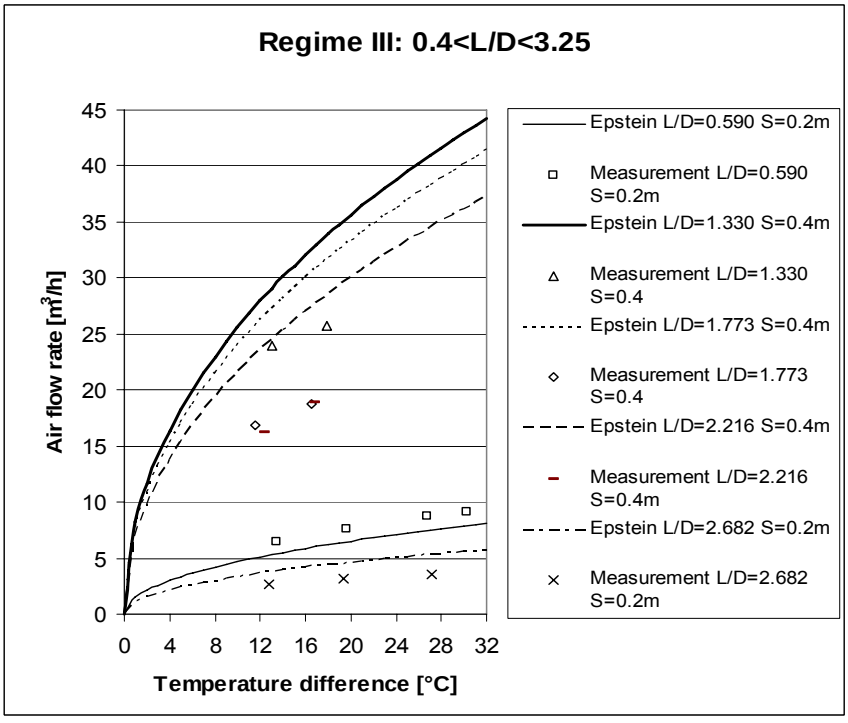

Figure 5.10(D)

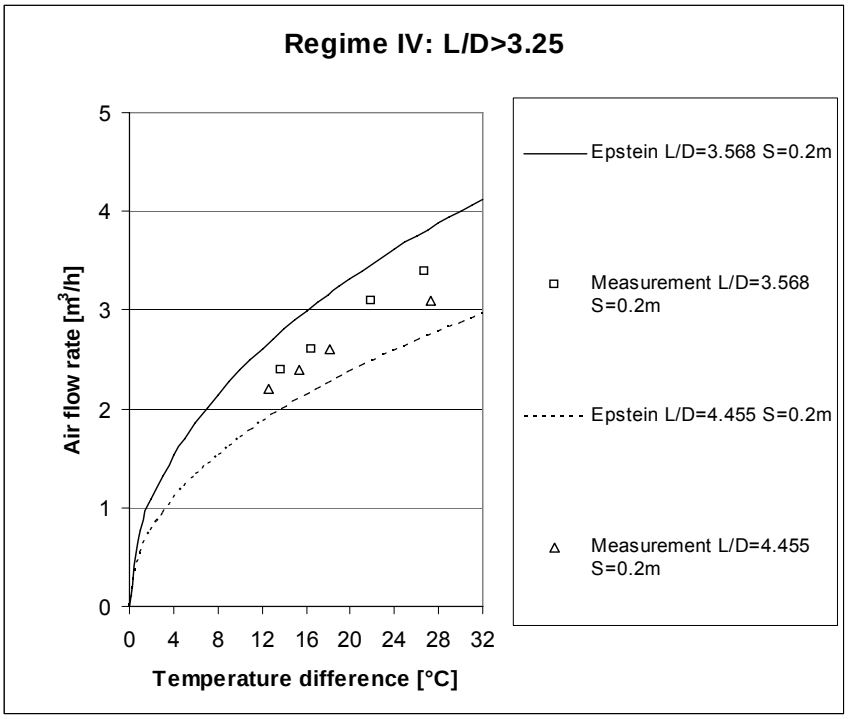

Figure 5.10(E)

Figure 5.10: The comparisons of air flow rate versus temperature difference in different flow regimes between the measured data and the calculated data from Epstein's formula.

In order to compare the full-scale air flow measurement data with the Epstein's brine-water scale measurement data, Figure 5.11 gives all the data of Froude numbers versus *L/D* for the both measurement methods. The Froude number tendency versus *L/D* ratio from the full-scale measurements fit well with those from the brine-water scale measurements. However, significant differences exist between them. For opening ratios *L/D* from 0.035 to 0.115, the dimensionless air flow rate *Fr* is found about 0.050, i.e. lower than the constant *Fr* value 0.055 given by Epstein. Conover et al. [10] as well as Sandberg and Blomqvist [17] also found these values lower than 0.055. Their values were between 0.035 and 0.047. When the *L/D* ratios are 0.027 and 0.03, the *Fr* are about 0.067 much higher than 0.055. The large deviations of these two points' data probably take place by the influence of the test room roof thickness, since the opening side length are 0.4m and 0.35m not much smaller than the hole's side length 1.0m. The maximum dimensionless air flow rate is found about 0.11 for *L/D*=0.59 in stead of *L/D*=0.4, and approximately 15% higher than the peak value 0.095 predicted by Epstein.

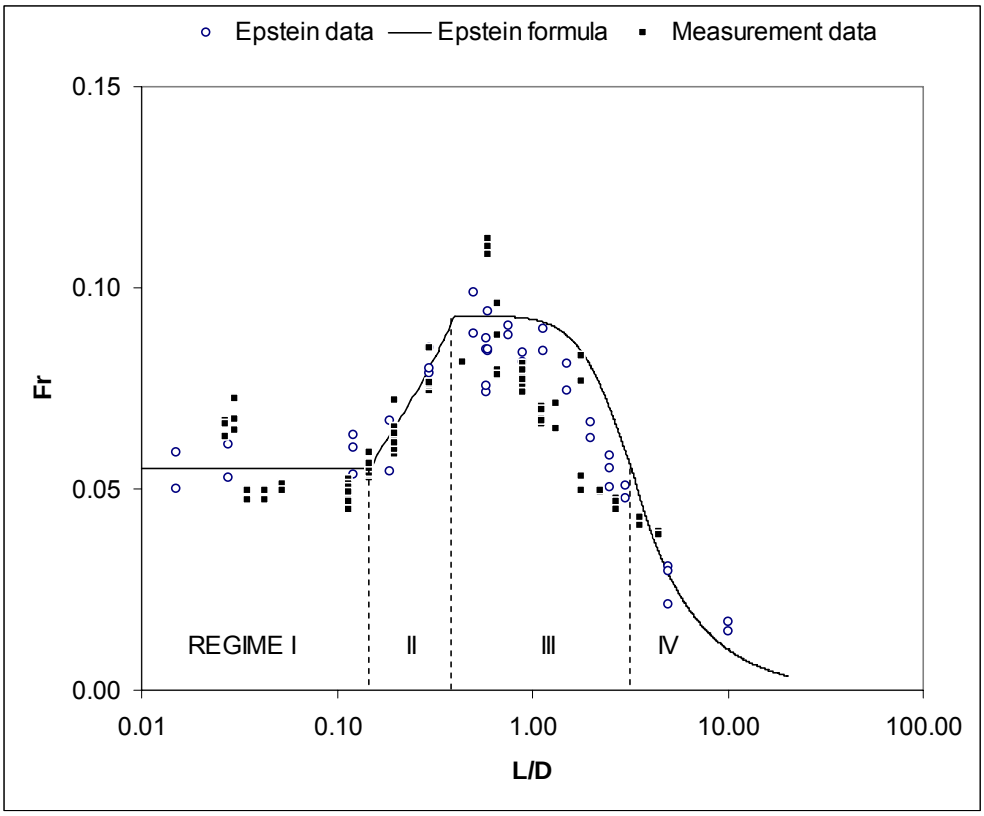

Figure 5.11: The *Fr* comparison between the full-scale air flow measurement and the Epstein brine-water scale measurement.

It can be seen also from this dimensionless *Fr* curve in Figure 5.11, that it seems only three flow regimes are found in this experimental study: oscillatory exchange flow (Regime I), Bernoulli flow (Regime II), and turbulent diffusion (Regime IV). The combined turbulent diffusion and Bernoulli flow (Regime III) is not so clear in this figure.

5.1.6 The developed formula with *Fr* and *L/D*

According to the above data analyses, a formula can be derived. The *Fr* value in the experimental study at *L/D* range below 0.115 can be expressed as:

$$Fr = 0.050 \qquad \frac{L}{D} < 0.115$$

Since the measurement data fit the Epstein's formula quite good in the opening ratio *L/D* range from 0.115 to 0.55, using power regression analysis, the *Fr* value at *L/D* range from 0.115 to 0.55 can be expressed as below, and the *R*-squared value is 0.961:

$$Fr = 0.147\left(\frac{L}{D}\right)^{0,5} \qquad 0.115 < \frac{L}{D} < 0.55$$

The major difference in the *Fr* value is found when the *L/D* range from 0.4 to 2.7. The combined turbulent diffusion and Bernoulli flow (Regime III) and turbulent diffusion (Regime IV) may be defined by using only one formula as below, using power regression analysis, and R^2=0.874:

$$Fr = 0.077\left(\frac{L}{D}\right)^{-0,5} \qquad 0.55 < \frac{L}{D} < 4.455$$

For the opening ratio *L/D* range from 0.55 to 4.455, the *R*-squared value is not good. It seems that there is a shortcoming using one formula to express two flow regimes. In order to overcome this shortcoming, it needs to do more measurements in this *L/D* range in the future.

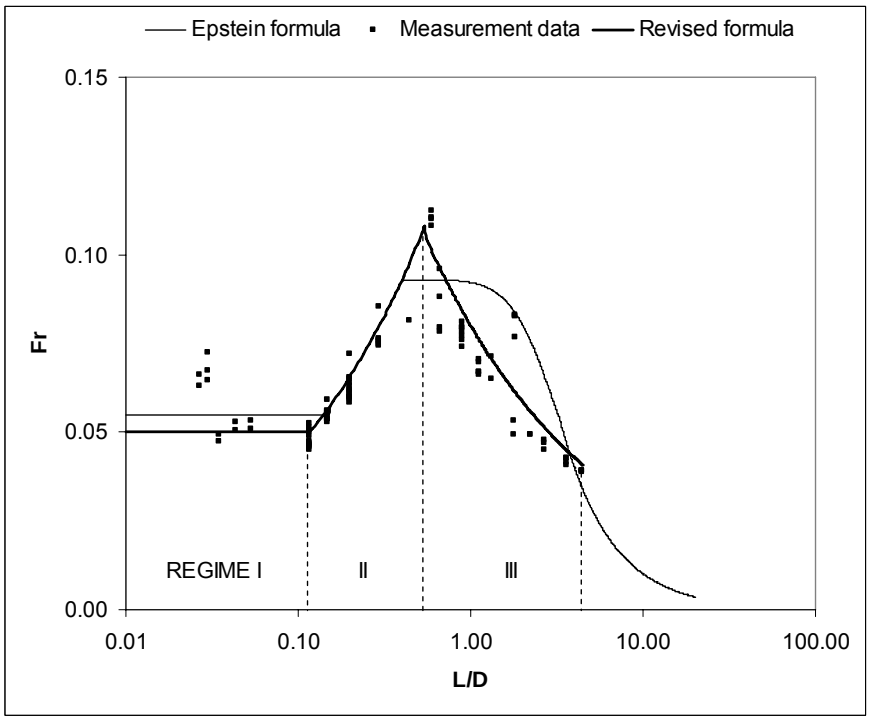

Figure 5.12: The dimensionless number *Fr* comparison between the Epstein's formula and the developed formula.

Thus, the dimensionless number *Fr* comparison between the Epstein's formula and the developed formula can be seen in Figure 5.12.

5.1.7 The developed formula with *Ar* and *A*

The Archimedes number is normally used in the formula of buoyancy driven natural ventilation, therefore, it is very useful to obtain the relation between *Ar* and the opening area *A*. As we know that:

$$Fr = \frac{q}{\sqrt{\frac{g(T_i - T_u)D^5}{T_i}}}$$

$$Ar = \frac{Gr}{\mathrm{Re}^2} = \frac{g\beta\Delta TL}{U^2}$$

If the characteristic length *D* and *L* are replaced by the side length of the square opening *S*, then

$$Fr = \frac{q}{\sqrt{\frac{g(T_i - T_u)D^5}{T_i}}}$$

$$= \frac{q}{\sqrt{\frac{g\Delta TS^5}{T_i}}}$$

$$= \frac{q}{A\sqrt{\frac{g\Delta TS}{T_i}}}$$

$$= \frac{U}{2\sqrt{g\beta\Delta TS}}$$

$$= \frac{1}{2\sqrt{Ar}}$$

Thus,

$$Ar = \frac{1}{4Fr^2} = \frac{\frac{g(T_i - T_u)S^5}{T_i}}{4q^2} = \frac{g\beta\Delta TS^5}{4q^2}$$

$$q = \frac{A}{2}\sqrt{\frac{g(T_i - T_u)\sqrt{A}}{T_i Ar}} = \frac{A}{2}\sqrt{\frac{g\beta\Delta T\sqrt{A}}{Ar}}$$

So, the Epstein formula can be described as the relation between *Ar* and *A* as follows:

$$\frac{L}{D}=\frac{L}{1.128\cdot S}=\frac{L}{1.128\cdot\sqrt{A}}$$

When

$$\frac{L}{D}=\frac{L}{1.128\cdot\sqrt{A}}<0.15$$

i.e.

$$\frac{L}{\sqrt{A}}<0.169$$

Then

$$Ar=\frac{1}{4Fr^2}=\frac{1}{4*0.055^2}=82.6$$

Similarly, the other three formulas can be obtained. Thus, the Epstein formula can be expressed as:

$$Ar=\frac{g\beta\Delta TS^5}{4q^2}$$

$$Ar=82.6 \qquad \frac{L}{\sqrt{A}}<0.169$$

$$Ar=13.0\frac{\sqrt{A}}{L}=13.0\left(\frac{L}{\sqrt{A}}\right)^{-1} \qquad 0.169<\frac{L}{\sqrt{A}}<0.451$$

$$Ar=28.9+1.692\left(\frac{L}{\sqrt{A}}-0.451\right)^3 \qquad 0.451<\frac{L}{\sqrt{A}}<3.666$$

$$Ar=1.701\left(\frac{L}{\sqrt{A}}\right)^3 \qquad 3.666<\frac{L}{\sqrt{A}}<11.28$$

Similarly, the new developed formula with Ar and $L/\sqrt{A}$ can be described as:

$$Ar = \frac{g\beta\Delta T S^5}{4q^2}$$

$$Ar = 100 \qquad \frac{L}{\sqrt{A}} < 0.130$$

$$Ar = 13.0\left(\frac{L}{\sqrt{A}}\right)^{-1} \qquad 0.130 < \frac{L}{\sqrt{A}} < 0.620$$

$$Ar = 37.4\frac{L}{\sqrt{A}} \qquad 0.620 < \frac{L}{\sqrt{A}} < 5.025$$

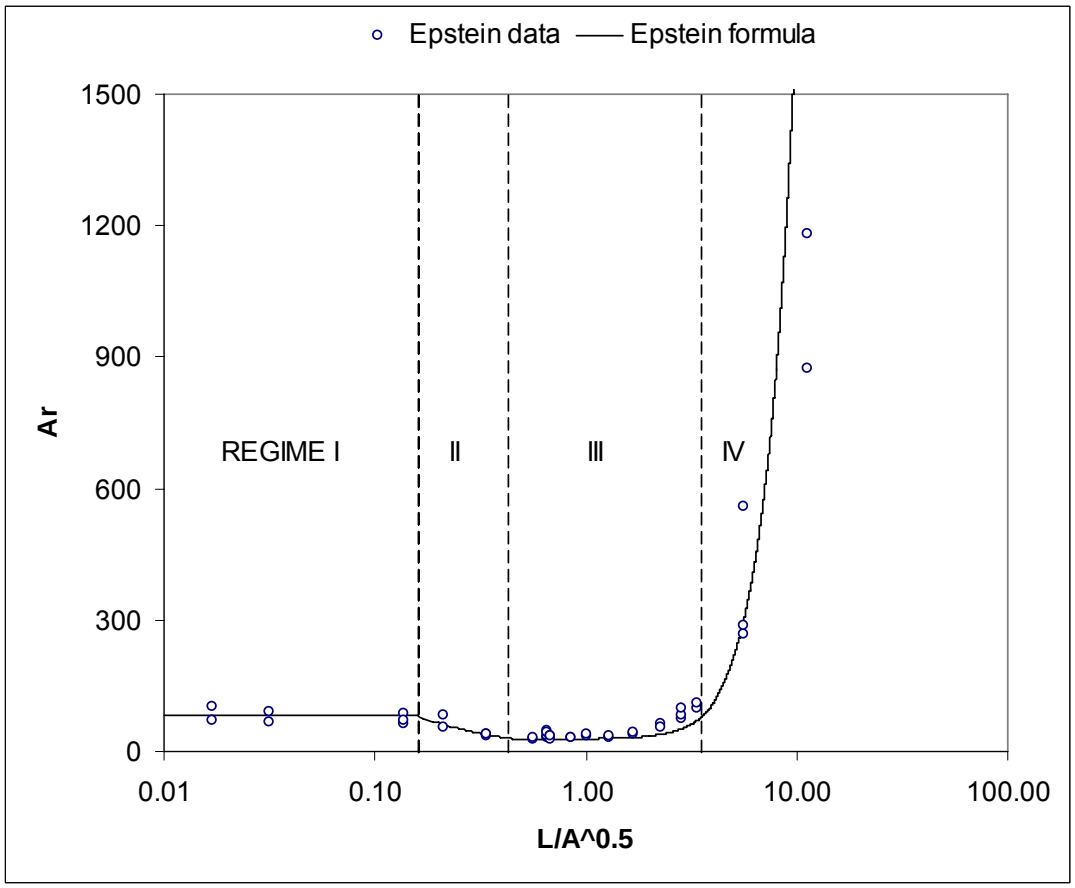

Figure 5.13: The Epstein's data and formula expressed by the dimensionless number Ar versus $L/\sqrt{A}$.

Figure 5.13 shows the Epstein's data and formula expressed by the dimensionless number Ar versus $L/\sqrt{A}$, and Figure 5.14 shows the Ar comparison between the full-scale air flow measurement and the Epstein brine-water scale measurement.

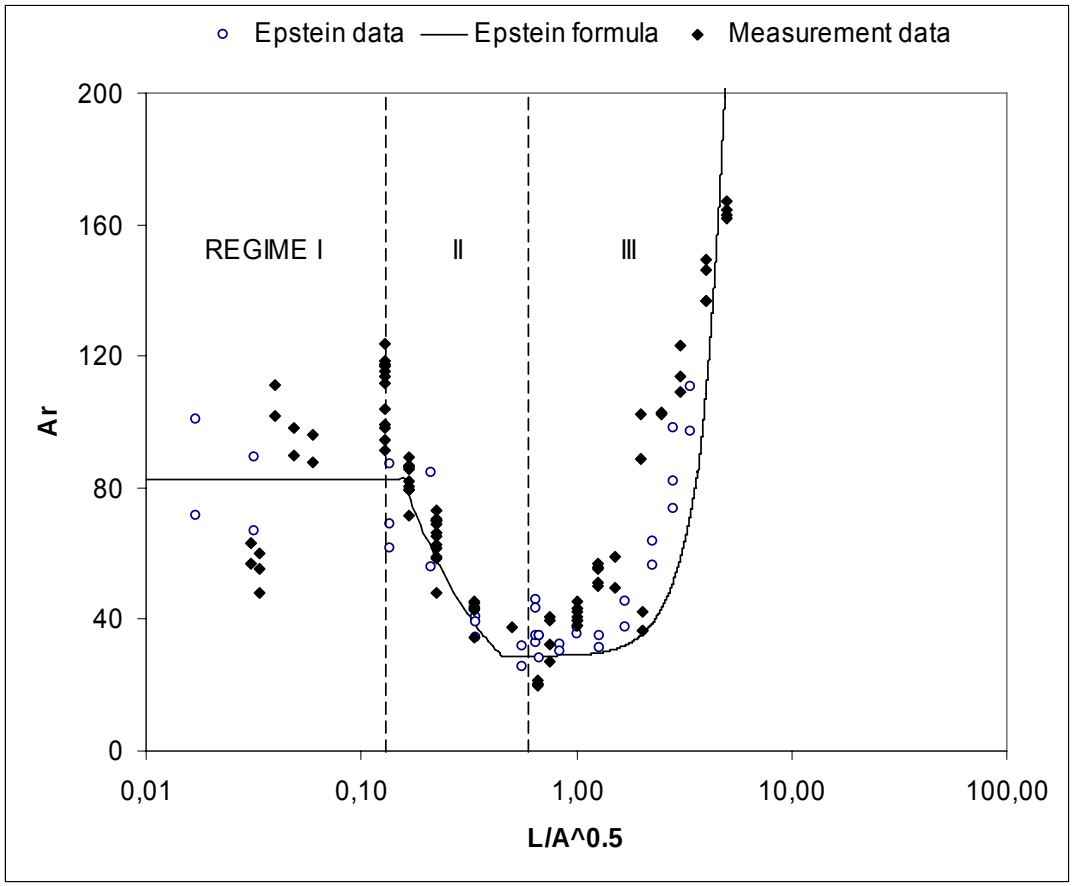

Figure 5.14: The *Ar* comparison between the full-scale air flow measurement and the Epstein brine-water scale measurement.

5.2 CFD results

5.2.1 CFD cases

Two cases of CFD simulations are carried out:

Case A: S=0.4m, L=0.2m, L/D=0.443, $L/\sqrt{A}=L/S$=0.5

Case B: S=0.4m, L=0.27m, L/D=0.6, $L/\sqrt{A}=L/S$=0.675

5.2.2 Case A results

Figure 5.15(A) and 5.15(B) show the air flow rate history calculated by time-dependent k-ε model and LES model. The time step size Δt is set to be 0.1s for k-ε model and 0.03s for LES. The calculated temperature difference between the test room and the thermostatic chamber is 15.3ºC that changes slightly with the time. The measured air flow rate at this temperature difference is 27m^3/h; and the calculated

average air flow rate during the simulation flow time is 14.6m^3/h for *k*-*ε* model and 29.2m^3/h for LES model. The air flow rate calculated by LES agrees well with the measured data, whereas the air flow rate calculated by *k*-*ε* model is almost half of the measured value.

The steady state *k*-*ε* model has been also simulated, but a converged solution can not be obtained since the buoyancy driven flow through this horizontal opening is highly transient and unstable. The time-dependent computation reveals that the flow patterns in the zones as well as in the horizontal opening are highly transient and unstable and the dominant mode of air exchange through the opening is intermittent pulses. The LES simulation gives the air flow rate pulse frequency about 0.3s^{-1}, which is much higher than given by the *k*-*ε* model. The same tendency of the mean air temperature history at the lower end of the opening is shown in Figure 5.16. Figure 5.17 shows the air velocity vector distribution at the middle plane of the horizontal opening in X direction at four different time instants calculated by LES model. The flow pattern varies significantly at each time instant. Figure 5.18 and Figure 5.19 show the air velocity vector distribution at time *t*=11.3s by LES simulation.

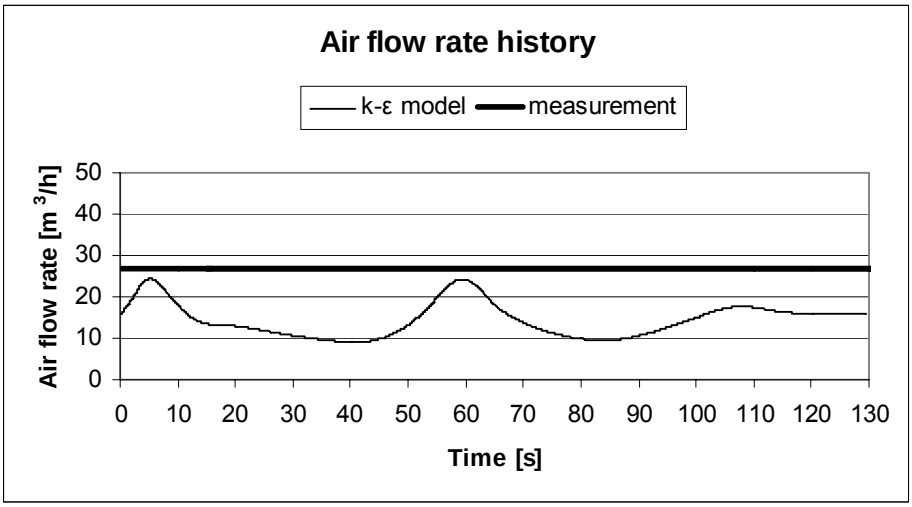

Figure 5.15(A)

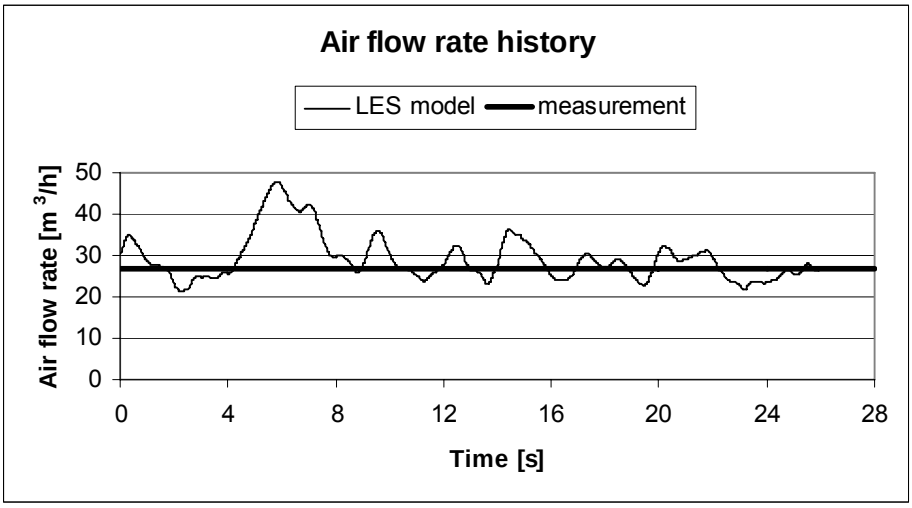

Figure 5.15(B)

Figure 5.15: The air flow rate history for Case A of buoyancy driven natural ventilation through one single-sided horizontal opening, (A) calculated by *k-ε* model (B) calculated by LES model.

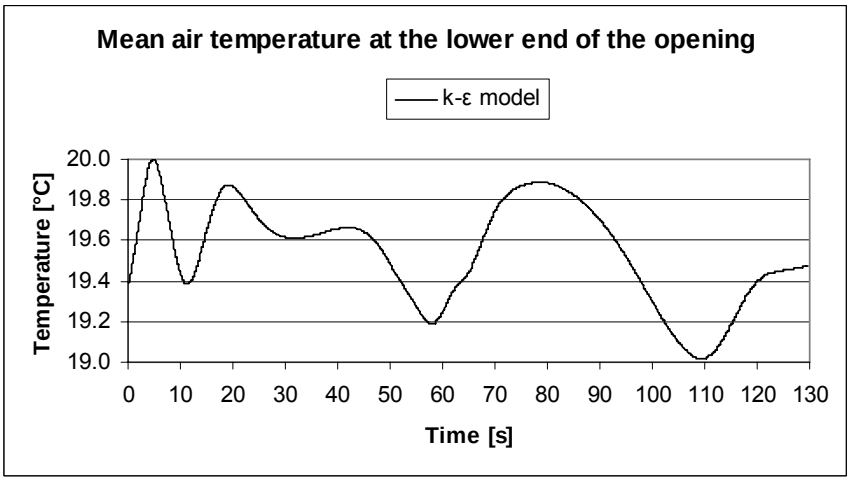

Figure 5.16(A)

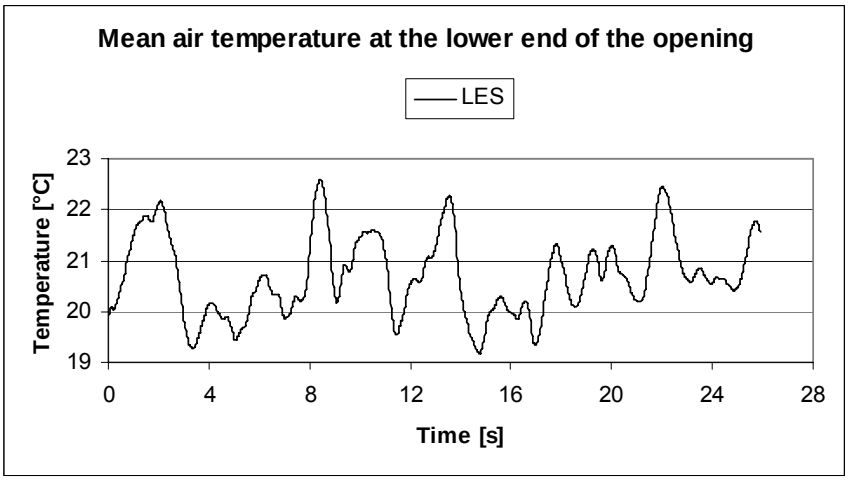

Figure 5.16(B)

Figure 5.16: The mean air temperature history at the lower end of the opening for Case A of buoyancy driven natural ventilation through single-sided one horizontal opening, (A) calculated by *k*-*ε* model (B) calculated by LES model.

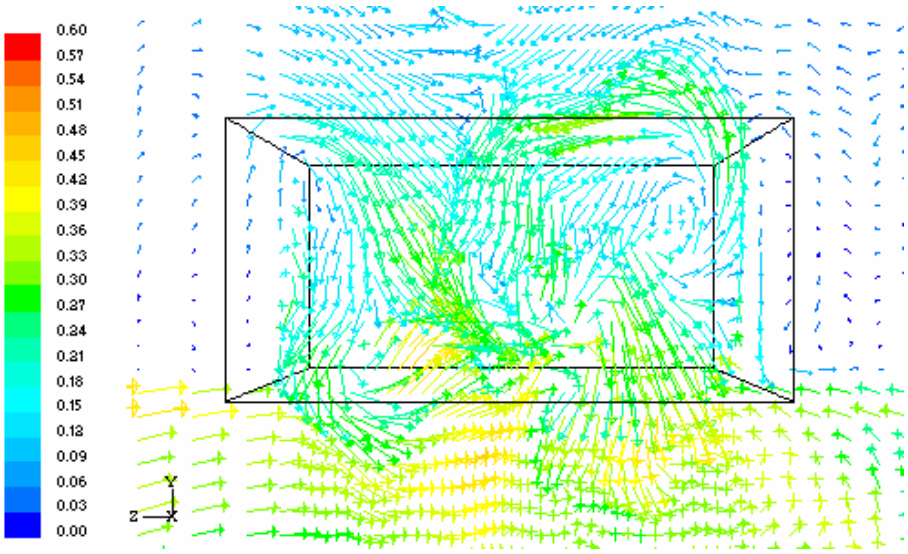

Figure 5.17(A)

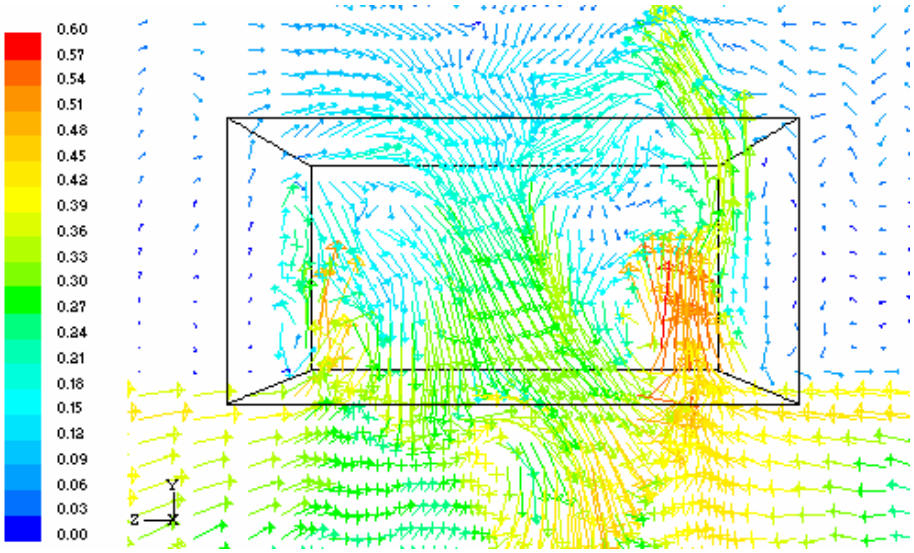

Figure 5.17(B)

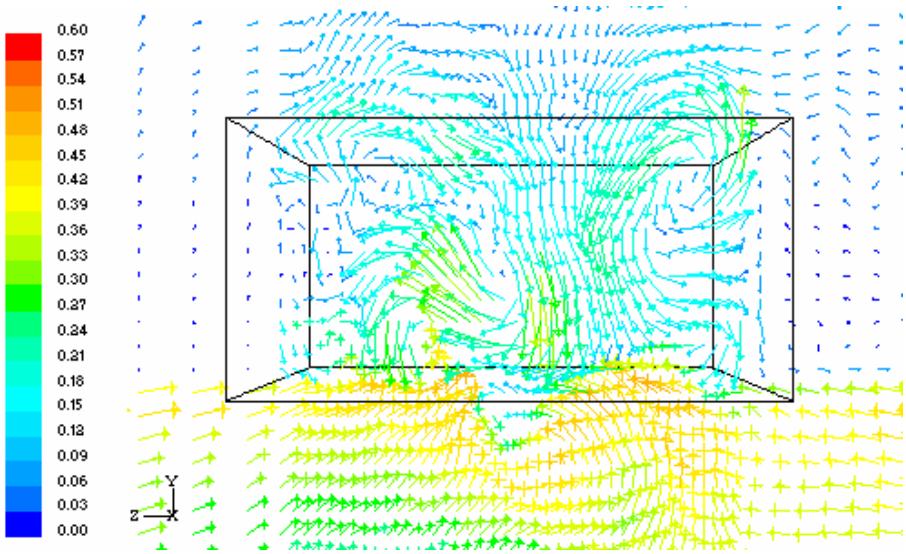

Figure 5.17(C)

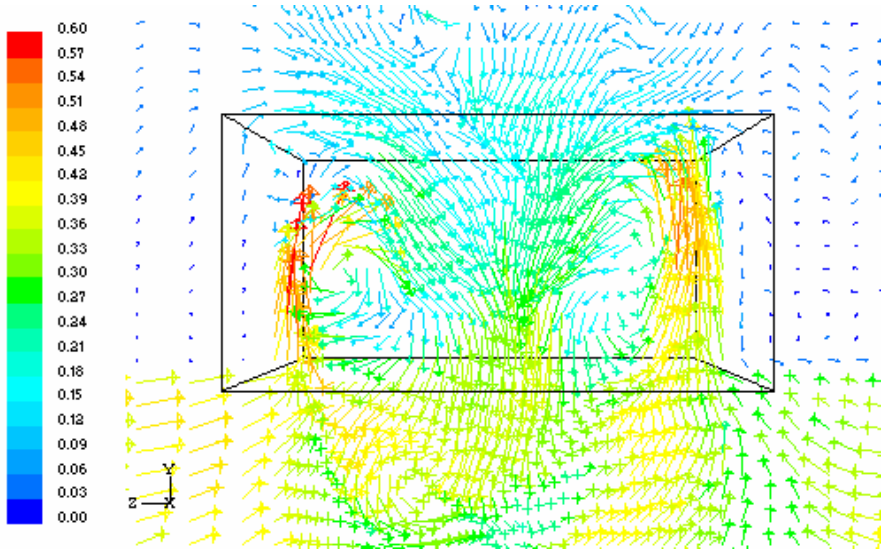

Figure 5.17(D)

Figure 5.17: The air velocity vector distribution coloured by velocity magnitude at the middle plane of the opening in X direction at four different time instants for Case A by LES simulation, (A) 11.3s, (B) 12.5s, (C) 13.7s and (D) 14.6s.

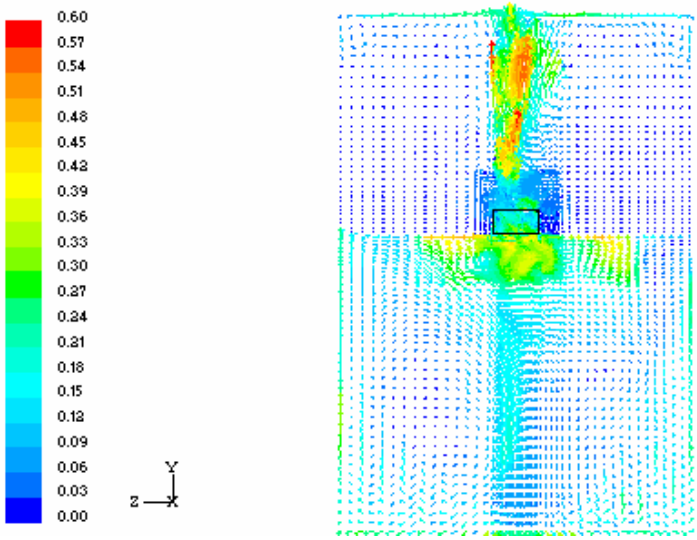

Figure 5.18(A). The air velocity vector distribution coloured by velocity magnitude at the middle plane of the opening in X direction at time t=11.3s by LES simulation.

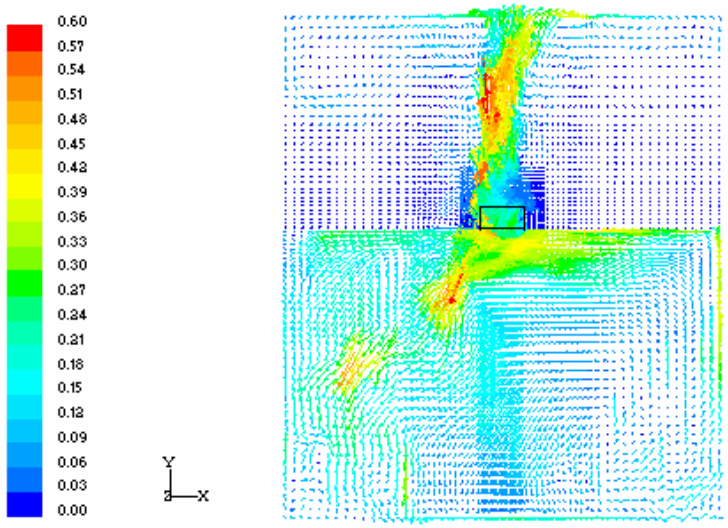

Figure 5.18(B). The air velocity vector distribution coloured by velocity magnitude at the middle plane of the opening in Z direction at time *t*=11.3s by LES simulation.

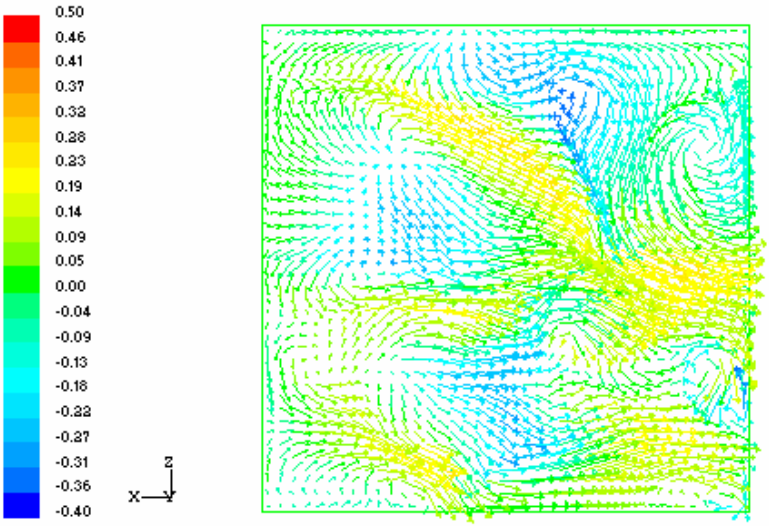

Figure 5.19(A). The air velocity vector distribution coloured by Y velocity at the lower end of the opening Y=2.7m in Y direction at time *t*=11.3s by LES simulation.

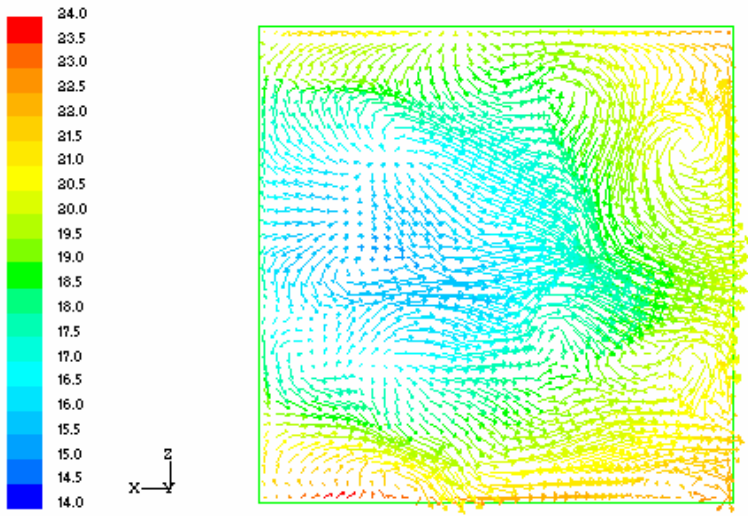

Figure 5.19(B). The air velocity vector distribution coloured by temperature at the lower end of the opening Y=2.7m in Y direction at time *t*=11.3s by LES simulation.

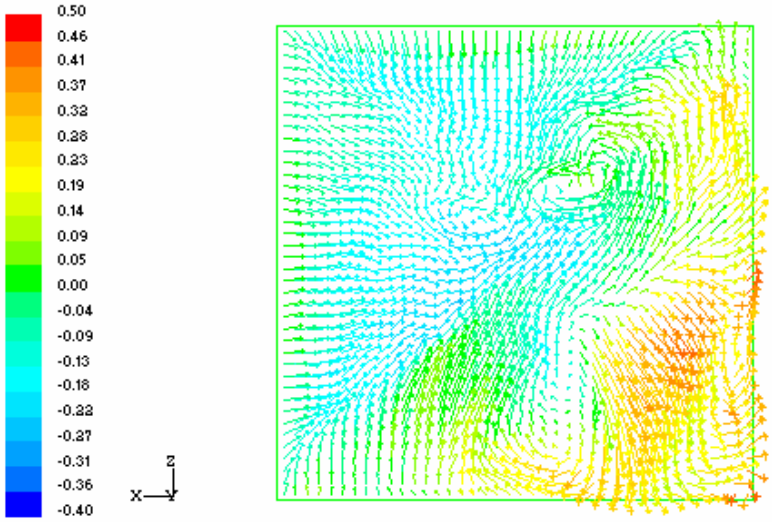

Figure 5.19(C). The air velocity vector distribution coloured by Y velocity at the upper end of the opening Y=2.9m in Y direction at time *t*=11.3s by LES simulation.

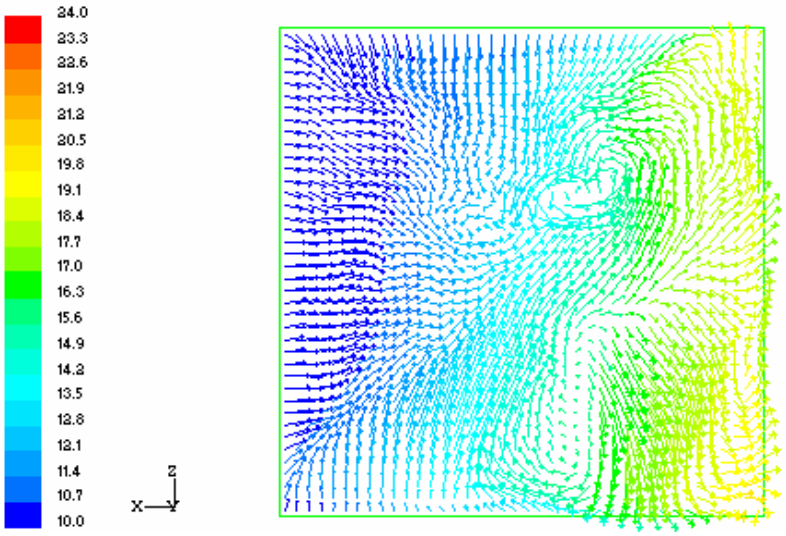

Figure 5.19(D). The air velocity vector distribution coloured by temperature at the upper end of the opening Y=2.9m in Y direction at time *t*=11.3s by LES simulation.

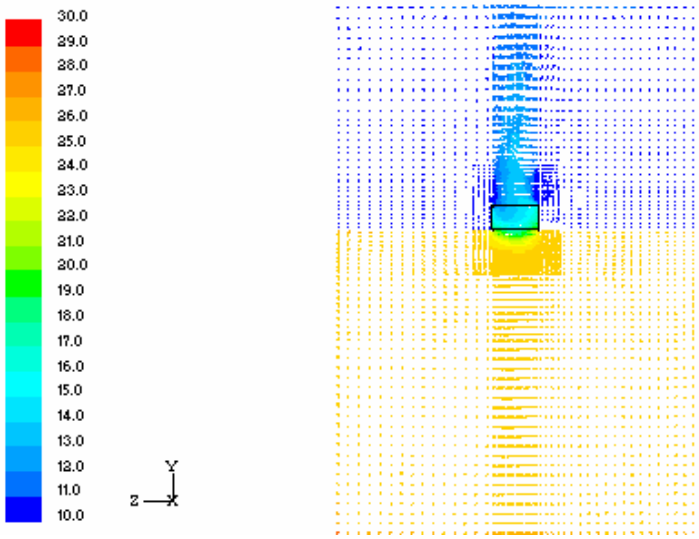

Figure 5.19(E). The air velocity vector distribution coloured by temperature at the middle plane in X direction at time *t*=11.3s by LES simulation.

5.2.3 Case B results

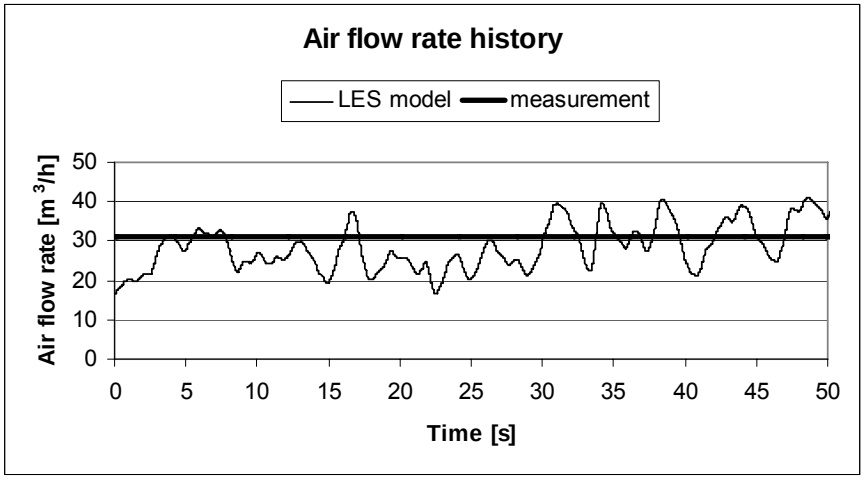

Figure 5.20: The air flow rate history for Case B of buoyancy driven natural ventilation through one single-sided horizontal opening, calculated by LES model.

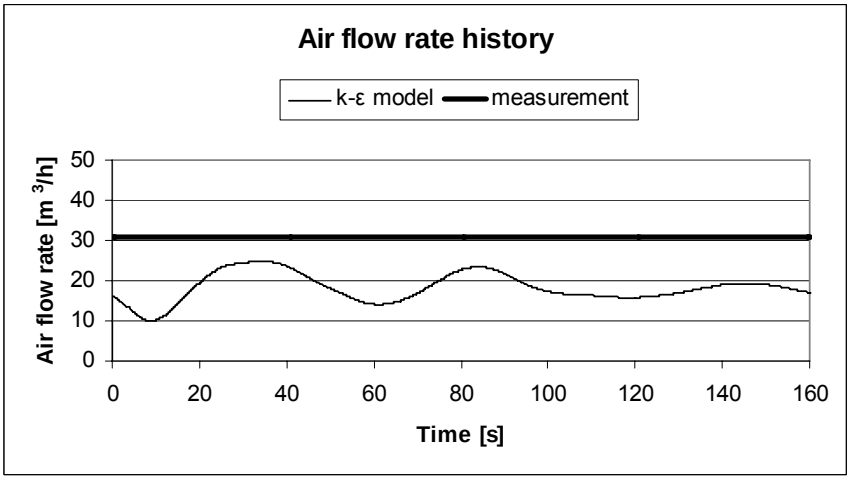

Figure 5.21: The air flow rate history calculated by *k-ε* model for Case B.

The time step size Δt is set to be 0.02s for LES model and 0.2s for *k-ε* mocel. The calculated temperature difference between the test room and the thermostatic chamber is about 13.8ºC that changes slightly with the time. The measured air flow rate at this temperature difference is about 31m^3/h; and the calculated average air flow rate during the simulation flow time is 28.9m^3/h by LES model and 18.2m^3/h by *k-ε* model. The air flow rate calculated by LES agrees well to the measured data, whereas the air flow rate calculated air flow rate by *k-ε* model is almost half of the measured value.

5.3 Conclusions

The highly transient, unstable and complex phenomenon of buoyancy driven natural ventilation through single-sided horizontal openings has been investigated in order to deepen understanding of the character of air flow within buildings. This experimental study has been focused on the bidirectional exchange flow through a single opening, and indicates that the deviations exist in the full-scale measurements and the Epstein's formula obtained from brine-water technique for estimating the air flow rate. The brine-water measurement should be testified and developed by a full-scale air flow measurement. The developed formula is necessary for predicting the air flow rate of buoyancy driven natural ventilation through a single horizontal opening. The limitation in this study is that only the maximum L/D ratio 4.455 is investigated, the scaling outside this range needs further studies. More measurements will also be required especially for the L/D range below than 0.035, since the significant deviations take place here probably due to the opening set-up.

The air flow rate and air flow pattern are predicted by the k-ε model and LES model. The cases calculated by the LES model agree well with the measured data, however, the cases simulated by the k-ε model are inaccurate compared to the measured data. The k-ε model simulation requires less computing time than the LES, and it can provide detailed airflow field distribution. However, the predicted ventilation rate and the air flow field are not good due to the simplification of the method for the highly transient and unstable flow, such as the buoyancy driven air flow through the horizontal openings. The LES model seems to be a suitable tool to study the case of highly transient buoyancy driven natural ventilation through one horizontal opening in order to provide detailed and accurate air flow information.

6 Experimental and numerical analysis of buoyancy driven natural ventilation through one horizontal opening combined with one vertical opening

6.1 Measurement results

6.1.1 Smoke visualization

The lower temperature air outside the test room has a higher density than the higher temperature air inside the test room. The density difference creates buoyancy driven flow through the high-level horizontal opening and the low-level vertical opening. The buoyancy force drives the heavier air inflow from the outside thermostatic chamber to the test room. In the case of two openings, this situation gives rise to unidirectional or bidirectional exchange flow across the two openings.

In order to get a better understanding of this unidirectional or bidirectional flow, smoke visualizations are carried out. The air flow pattern in steady state near the two openings is observed during the experiment. The smoke is introduced in the thermostatic chamber or in the test room, thus the inflow or outflow can be observed. Figure 6.1 shows the smoke visualization for the case of S_T=0.8m, S_B=0.2m, A_T/A_B=16 (A_T/A_B>1). Figure 6.1(A) presents the unidirectional inflow through the small bottom vertical opening S_B=0.2m. The cool incoming air flows into the room and then down to the floor because of its greater density. The air flows along the floor and picks up heat from it, then moves upwards and displaces the lighter air out across the top horizontal opening. Figure 6.1(B) presents the outflow through the larger top horizontal opening S_T=0.8m. The warm air flows out through a large part of the opening with varying air velocity and airflow directions. The dominant outflow takes a large part of the opening, and some heavier cool air flows into the test room through a small part of the opening. Vortices are produced when the warm air meets the cool air. The outflow is transient, unstable and complex compared with unidirectional displacement ventilation airflow, see flow pattern at different times t=0s, 0.5s, 1s and 2s in Figure 6.1(B(a)) to Figure 6.1(B(d)). In order to observe the inflow air through the top opening from the chamber into the test room, the smoke visualization is also introduced inside the test room, see Figure 6.1(C(a)) to Figure 6.1(C(d))

corresponding to the flow pattern at time t=0s, 0.5s, 1.5s and 2s. The smoke visualization shows clearly that the air inflow is highly transient, unstable and complex. The air velocity changes with time through different parts of the horizontal opening. In this case, the transient and unstable bidirectional flow occurs at the large horizontal opening, and comparatively steady unidirectional flow takes place at the small vertical opening. It may be said that displacement air distribution principle and mixing air distribution principle occur simultaneously at the horizontal opening, but only displacement air distribution occurs at the vertical opening. Because the air outflow rate is much higher than the air inflow rate across the horizontal opening, i.e. the air flow rate contributed by displacement is much higher than contributed by mixing, the displacement air distribution is dominant in this case.

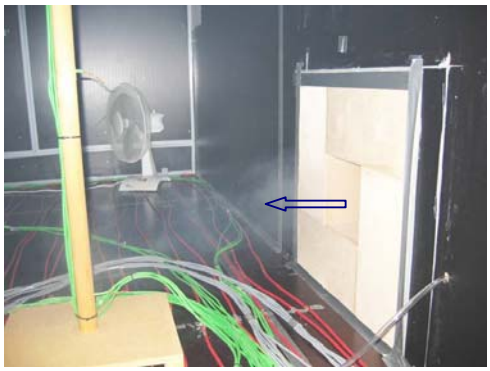

Figure 6.1(A)

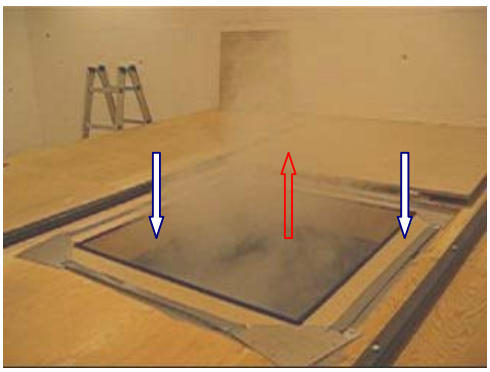

Figure 6.1(B(a))

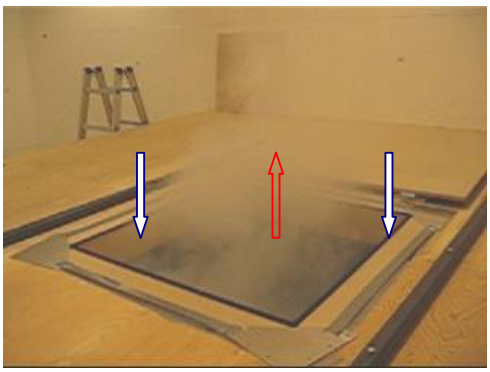

Figure 6.1(B(b))

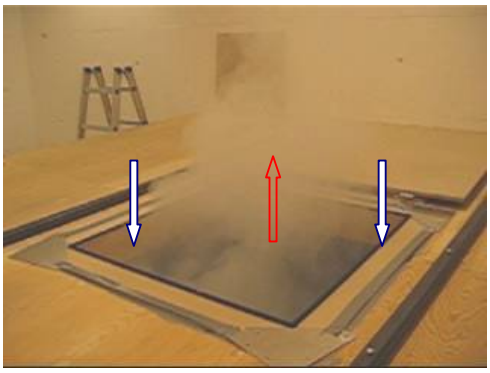

Figure 6.1(B(c))

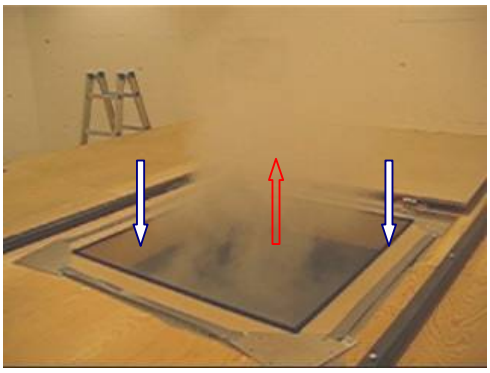

Figure 6.1(B(d))

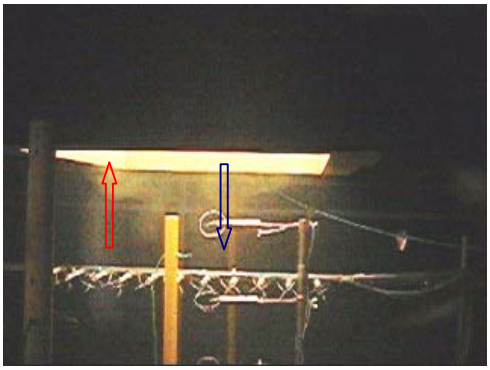

Figure 6.1(C(a))

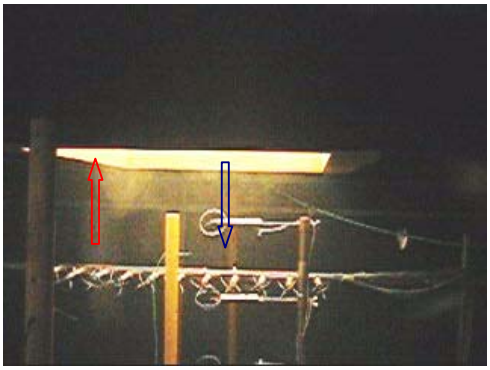

Figure 6.1(C(b))

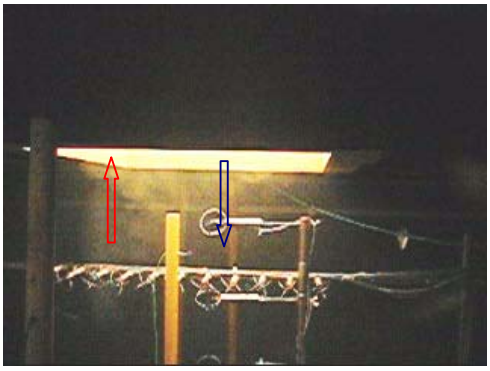

Figure 6.1(C(c))

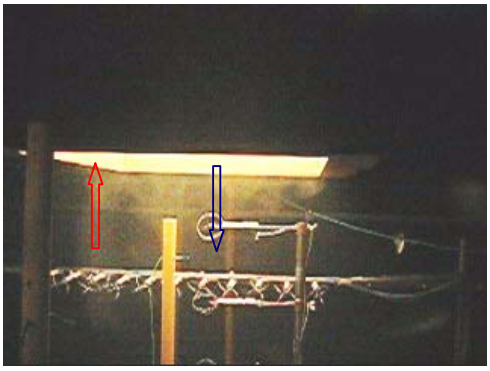

Figure 6.1(C(d))

Figure 6.1: The smoke visualization for the case of S_T=0.8m, S_B=0.2m, A_T/A_B=16. (A) The unidirectional inflow through the small bottom vertical opening S_B=0.2m. (B) The outflow pattern through the larger top horizontal opening S_T=0.8m at different times, (a) t=0s, (b) t=0.5s, (c) t=1s and (d) t=2s. (C) The inflow pattern through the larger top opening S_T=0.8m at different times, (a) t=0s, (b) t=0.5s, (c) t=1s and (d) t =2s.

As an example of the case $A_T/A_B<1$, the smoke visualization is shown in Figure 6.2 for the case of S_T=0.2m, S_B=0.5m, A_T/A_B=0.16. Figure 6.2(A) presents the unidirectional outflow through the top horizontal opening. Since the bottom opening is significantly larger than the horizontal opening, the bidirectional flow occurs through the vertical opening. The cool air flows into the test room across the lower part of the opening; and at the same time, due to the lower density, the warm air flows out from the test room into the chamber across the upper part of the opening, then flows upwards inside the chamber, see Figure 6.2(B). The flow pattern at the vertical opening is quite similar with the buoyancy driven natural ventilation through a single-sided vertical opening, but the air inflow rate is much higher than the air outflow rate across the vertical opening. It may be also said that displacement air distribution principle and mixing air distribution principle occur simultaneously at the vertical opening, and only displacement air distribution occurs at the vertical opening. Because the air inflow rate is much higher than the air outflow rate across the vertical opening, i.e. the air flow rate contributed by displacement is much higher than it contributed by mixing, the displacement is still dominant in this case.

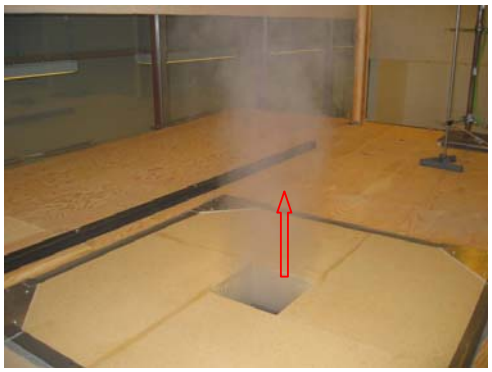

Figure 6.2(A)

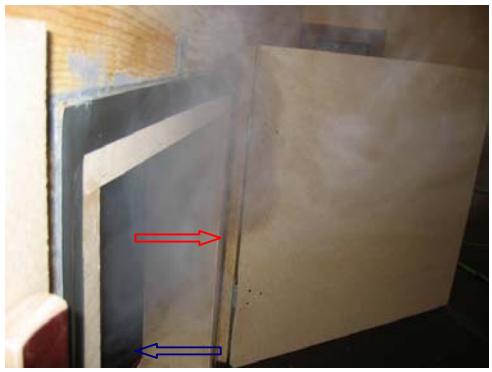

Figure 6.2(B)

Figure 6.2: The smoke visualization for the case of S_T=0.2m, S_B=0.5m, A_T/A_B=0.16. (A) The unidirectional outflow through the top horizontal opening and (B) The outflow pattern through the upper part of the bottom opening.

For the case of A_T/A_B close to 1, the unidirectional flow occurs through both the vertical and horizontal openings. It is not necessary to present the smoke visualization here, since the flow pattern belongs to the typical displacement ventilation, which is well known in many studies.

6.1.2 Three flow modes

The smoke visualizations have been done in all of the measurement cases for the opening ratio A_T/A_B range from 0.11 to 25, in order to find the flow modes' transition points. Thus, three flow modes have been observed:

- Mode I ($0.11<A_T/A_B<0.25$): bidirectional flow through the large vertical opening and one directional flow out through the small horizontal opening, the air flow pattern is comparative stable, schematically shown in Figure 6.3(A);
- Mode II ($0.33<A_T/A_B<4.94$): unidirectional flow through the both vertical and horizontal opening, the air flow pattern is stable, shown in Figure 6.3(B);
- Mode III ($5.76<A_T/A_B<25$): unidirectional flow through the small vertical opening and bidirectional flow through the large horizontal opening, the bidirectional flow is transient and unstable, shown in Figure 6.3(C).

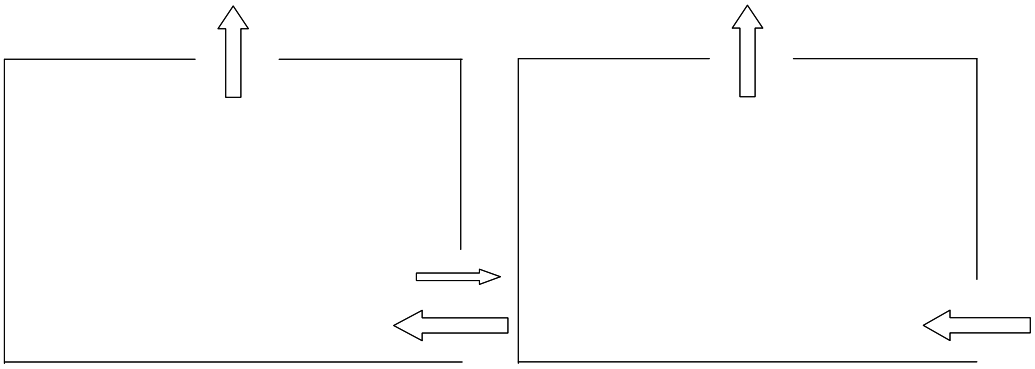

Figure 6.3(A)

Figure 6.3(B)

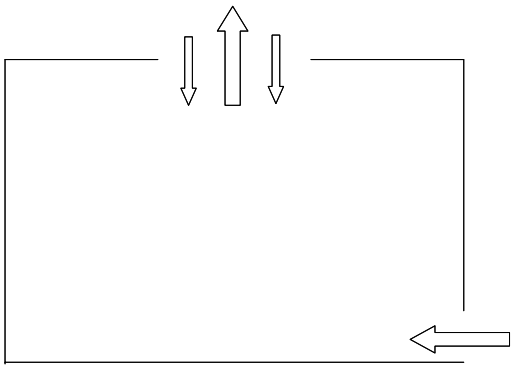

Figure 6.3(C)

Figure 6.3: The schematics of three flow modes, (A) the flow mode I, (B) the flow mode II, and (C) the flow mode III.

In mode I, the main air flow is supplied into the test room through the vertical opening and displaces the lighter air inside the room out through the horizontal opening.

However, some incoming air mixes with the air inside the room and flows out through the upper part of the vertical opening. In this mode, the displacement and the mixing air distribution occur simultaneously, but the displacement air distribution is dominant. The mixing effect increases when the A_T/A_B value decreases. Therefore, the air flow rate may increase due to this bidirectional flow. The air flow rate calculated by the present calculation formula is smaller than the measured air flow rate. Thus, a new air flow rate calculation formula is required.

The mode II is the simple displacement ventilation case and has been discussed widely in the literatures. The air flow rate calculated by the present calculation formula is close to the measured air flow rate.

The unidirectional flow entering into the test room through the vertical opening and flowing out through the horizontal opening is found in the mode III. But some dense air also enters into the test room from the upper thermostatic chamber. This situation gives rise to bidirectional exchange flow across the horizontal opening, and thus the incoming flow is highly transient and unstable. In the mode III, the displacement and the mixing air distribution occur simultaneously as well, and the displacement is also dominant. The effect of the mixing increases with the A_T/A_B value increasing. The air flow rate calculated by the present calculation formula is smaller than the measured air flow rate. Thus, a new air flow rate calculation formula may be derived in this mode as well.

The critical transition points for flow mode exchange are located in the A_T/A_B range of $0.25<A_T/A_B<0.33$ and $4.94<A_T/A_B<5.76$.

6.1.3 LDV velocity measurement

Vertical velocity component measurements are performed using Laser Doppler Velocimetry. The experiment is made several times at different points at the horizontal opening for one case keeping constant temperature difference, since this LDV instrument made velocity measurement at only one point and one velocity component once.

Figure 6.4(A) presents a typical vertical velocity history during 1000 seconds at a point close to one corner of the top horizontal opening for case S_T=0.6m, S_B=0.2m and A_T/A_B=9 at temperature difference ΔT=11.7°C. The distance from this point to the opening corner is 13cm. This case belongs to the air flow mode III. The vertical velocity at this point varies between positive (upflow) and negative (downflow). The

vertical velocity component varies between -0.29m/s and 0.28m/s, but the positive velocity value is dominant. The vertical velocity histogram of this point can be seen in Figure 6.4(B). The positive velocity value takes about 97% of the total occurrences, but the negative velocity value takes only 3%. The velocity values mainly concentrate in the range of 0.15m/s to 0.25m/s, occupying 90%. The LDV measurements confirm the qualitative flow patterns given by flow visualization, which means, the bidirectional flow is transient and unstable, and the displacement air distribution is dominant. All of the LDV measurements at different points in this case gave quite similar vertical velocity pattern.

As a result the vertical component of velocity measured by LDV can state the bidirectional flow motion and the spectral analysis of flow. The frequency of pulsations is measured from the power spectrum of LDV data. Figure 6.4(C) shows the corresponding spectrum at the same point, but the clearly defined frequency can not be identified from the spectrum. Figure 6.4(D) and Figure 6.4(E) show the vertical velocity history and its histogram at this point for the same case at lower temperature difference ΔT=6.7°C. The lower temperature difference results in little lower velocity variations between -0.22m/s and 0.28m/s. The positive velocity value takes about 98% of the total value and the velocity values mainly concentrate in the range of 0.1m/s to 0.25m/s, occupying 84%.

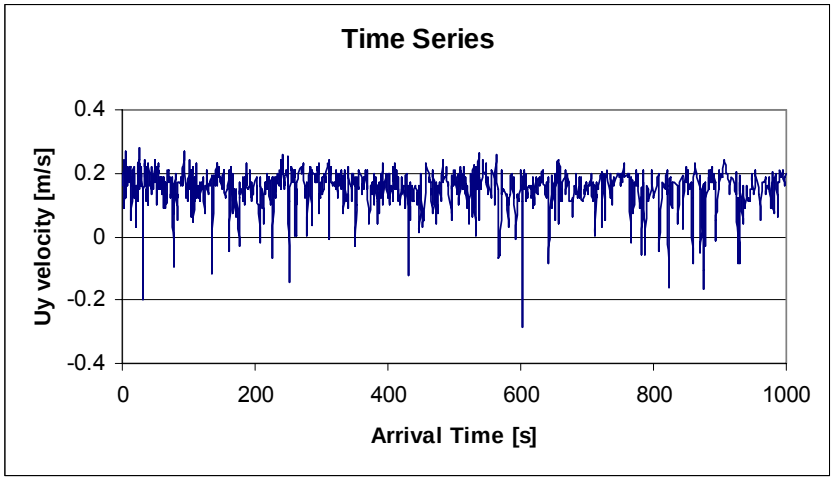

Figure 6.4(A)

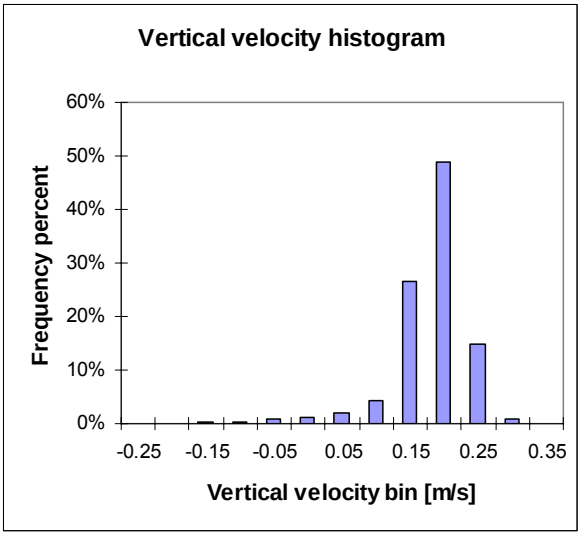

Figure 6.4(B)

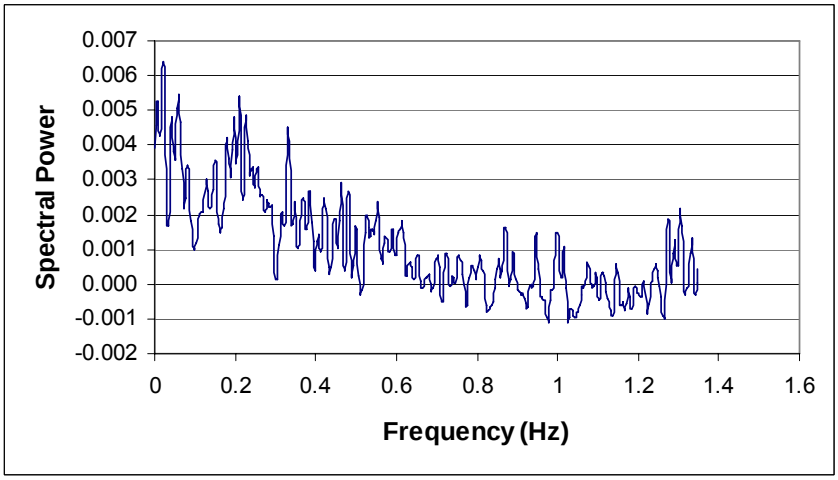

Figure 6.4(C)

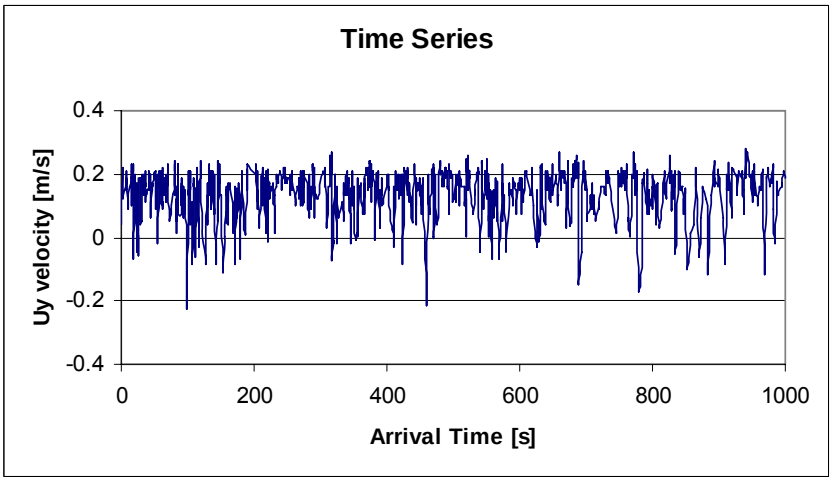

Figure 6.4(D)

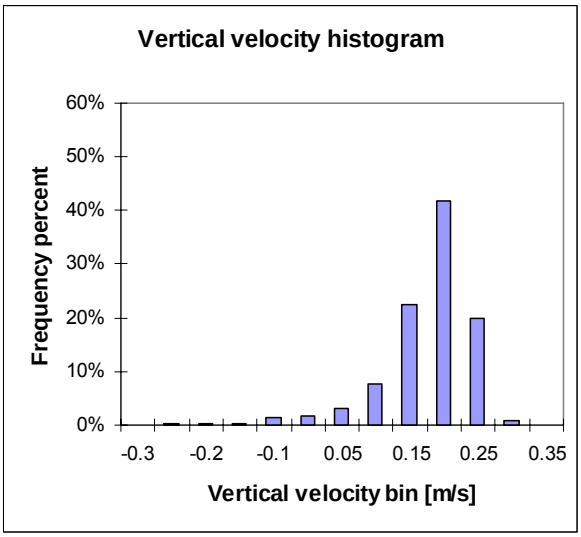

Figure 6.4(E)

Figure 6.4: LDV measurement at a point close to one corner of the top horizontal opening for the case S_T=0.6m, S_B=0.2m and A_T/A_B=9. (A) The vertical velocity history during 1000 seconds, ΔT=11.7°C. (B) The vertical velocity histogram, ΔT=11.7°C. (C) The corresponding spectrum, ΔT=11.7°C. (D) The vertical velocity history, ΔT=6.7°C. (E) The vertical velocity histogram, ΔT=6.7°C.

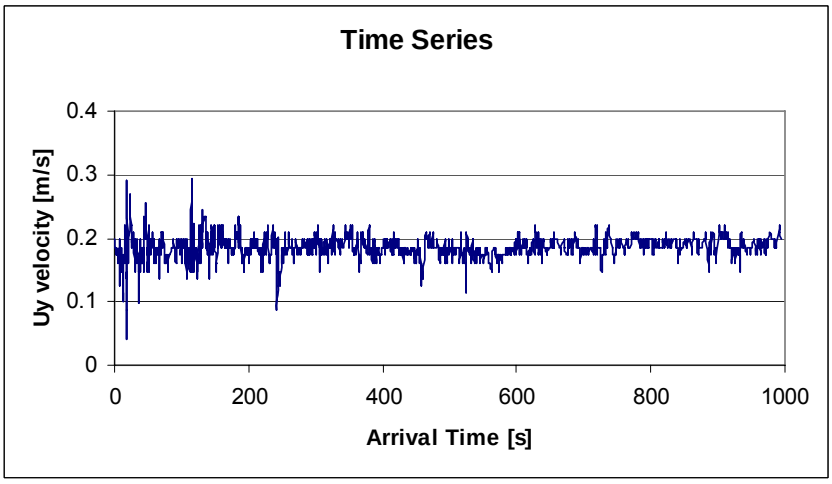

Figure 6.5(A)

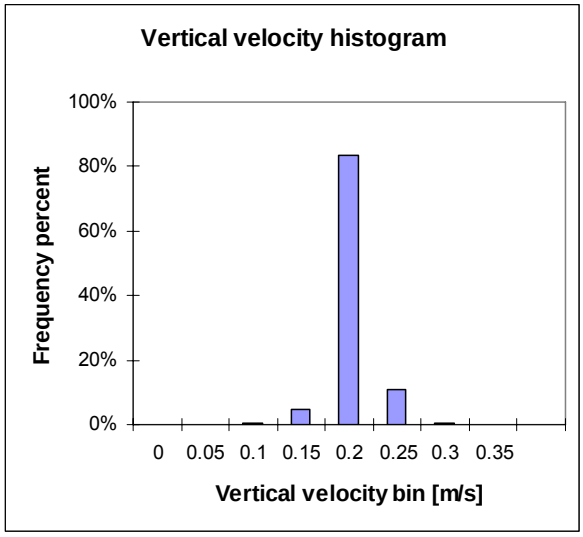

Figure 6.5(B)

Figure 6.5: LDV measurement for the case S_T=0.4m, S_B=0.2m, A_T/A_B=4 and ΔT=8.9°C. (A) The vertical velocity history during 1000 seconds. (B) The vertical velocity histogram.

Figure 6.5 shows the vertical velocity history measured by LDV for the case S_T=0.4m, S_B=0.2m, and A_T/A_B=4, at temperature difference ΔT=8.9°C, which belongs to the air flow mode II. Because the laser probe length used plus the laser beam length is longer than 0.6m, the measuring point has to be located at minimum 6cm below the center of top horizontal opening. All the vertical velocity at this point is positive, which implies the unidirectional upflow through the horizontal opening, shown in Figure 6.5(A). The velocity values mainly concentrate in the range of 0.15m/s to 0.20m/s, taking 83% of the total occurrences, see Figure 6.5(B). The LDV measurements confirmed that the unidirectional air flow is quite stable in this case.

6.1.4 Temperature gradient

A feature of displacement ventilation is the formation of horizontal air layers. The warmest air layer is at the top, and the coolest air layer is at the bottom. However, this situation is only fit for air flow mode II, because this mode is completely displacement ventilation. The flow mode III are not fit for this temperature gradient situation, because the bidirectional flow mixing air distribution occurs in this case.

In order to compare the temperature gradient between different opening ratio cases, the 10 point's temperature value has been measured in the center line of the test room at height 0.04m, 0.1m, 0.2m, 0.4m, 0.6m, 0.85m, 1.1m, 1.35m, 1.7m and 2.35m.

Figure 6.6(A) shows the temperature gradients of 5 cases with the same bottom vertical opening S_B=0.2m, and Figure 6.6(B) shows the temperature gradients as well of 5 cases with the same top horizontal opening S_T=0.2m. The temperatures are calculated as the average value of the steady state flow during the measurement time. If the dimensionless temperature difference $\Delta T / \overline{\Delta T}$ is used, where the ΔT is the temperature difference between the indoor temperature at the measured point and outdoor mean temperature, and $\overline{\Delta T}$ is the temperature difference between the mean indoor temperature and outdoor mean temperature, the temperature gradient can be seen in Figure 6.6(A) and Figure 6.6(B).

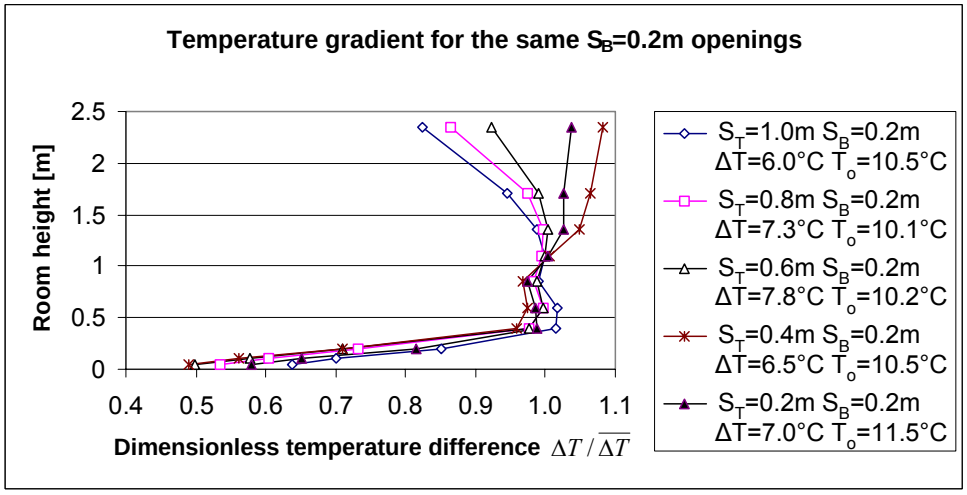

Figure 6.6(A)

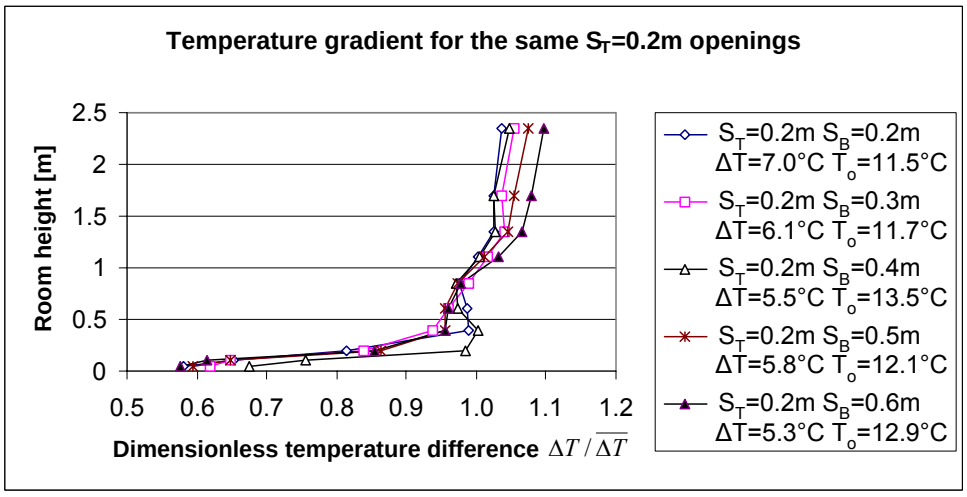

Figure 6.6(B)

Figure 6.6: The temperature gradients in the center line of the test room. (A) The temperature gradients of 5 cases with the same bottom vertical opening S_B=0.2m. (B) The temperature gradients of 5 cases with the same top horizontal opening S_T=0.2m.

When the bidirectional flow occurs through the top opening shown in Figure 6.6(A), the temperature increases first from the lowest level and then decreases at a certain height level. Because the air flow rate influences the temperature gradient inside the room, this height level is lower with the larger top opening. When the bidirectional flow occurs through the bottom opening shown in Figure 6.6(B), the temperature gradients do not change so much in these different cases in the center line of the test room.

6.1.5 The neutral plane

For the case of two opening at two different heights, there exists a horizontal plane between the openings that is called the neutral plane, where inside and outside pressures are equal. Due to the same type of the two openings, the height of the neutral plane can be calculated as:

$$H_0 = \frac{A_T^2 H_T + A_B^2 H_B}{A_T^2 + A_B^2}$$

$$H_0 = \frac{\left(\frac{A_T}{A_B}\right)^2 H_T + H_B}{\left(\frac{A_T}{A_B}\right)^2 + 1}$$

Where H_0 is the height of the neutral plane [m]
H_T is the height of the top horizontal opening [m]
H_B is the height of the bottom vertical opening [m]

In this full scale measurement, H_B=0.3m, H_T=2.7+0.133/2=2.7665m, the neutral plane height versus opening ratios A_T/A_B can be illustrated in Figure 6.7(A). Figure 6.7(B) shows the dimensionless neutral plane height H_0/H_T versus A_T/A_B.

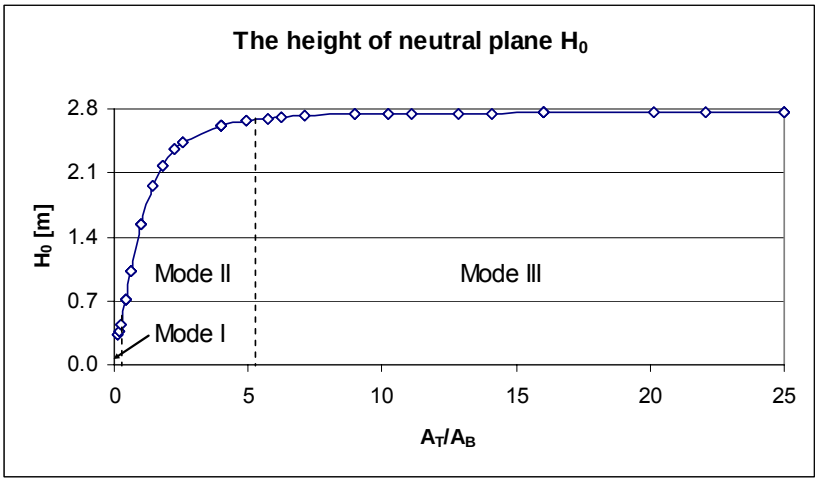

Figure 6.7(A): The neutral plane height versus opening ratios A_T/A_B.

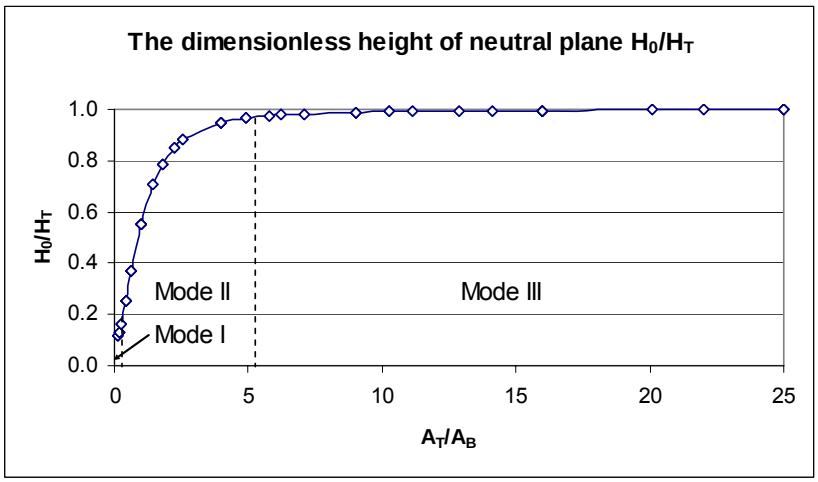

Figure 6.7(B): The dimensionless neutral plane height H_0/H_T versus opening ratios A_T/A_B.

These two figures clearly show that the neutral plane height rises with opening ratio A_T/A_B increase, and the flow mode varies from Mode I to Mode II or from Mode II to Mode III at a critical transition point. The measurements show that this critical point locates at $0.25<A_T/A_B<0.33$. Table 6.1 shows the two measurement opening cases for critical point from Mode I to Mode II. The air flow Mode I occurs when the height of neutral plane H_0 locates below the height of bottom vertical opening H_{BT}; and the air flow transition from Mode I to Mode II occurs when H_0 locates above H_{BT}. When the neutral plane is quite close to the top horizontal opening, the air flow mode changes to Mode III, i.e. the air flow Mode II occurs when the neutral plane locates between the

two openings. Table 6.2 shows the two measurement opening cases for critical point from Mode II to Mode III.

S_T [m]	S_B [m]	A_T/A_B	Height of neutral plane H_0 [m]	Top height of the bottom vertical opening H_{BT} [m]	Flow direction through the bottom vertical opening	Flow mode
0.2	0.4	0.25	0.445	0.5	bidirectional	I
0.2	0.35	0.33	0.538	0.475	unidirectional	II

Table 6.1: The two measurement opening cases for critical point from Mode I to Mode II.

S_T [m]	S_B [m]	A_T/A_B	Height of neutral plane H_0 [m]	Flow direction through the bottom vertical opening	Flow mode
0.8	0.36	4.94	2.669	unidirectional	II
0.6	0.25	5.76	2.694	bidirectional	III

Table 6.2: The two measurement opening cases for critical point from Mode II to Mode III.

The pressure difference for the top horizontal opening can be calculated as [32]:

$$\Delta P_T = \rho_u g \frac{T_i - T_u}{T_i}\left(H_T - H_o\right)$$

S_T [m]	S_B [m]	T_i [˚C]	T_u [˚C]	ρ_i [kg/m^3]	ρ_u [kg/m^3]	H_T [m]	ΔP_T [Pa]	ΔP_C [Pa]
0.8	0.36	16.5	13.1	1.222	1.237	2.669	0.014	0.020
0.8	0.36	20.9	14.1	1.204	1.232	2.669	0.027	0.037
0.8	0.36	23.9	13.8	1.1915	1.234	2.669	0.040	0.056
0.6	0.25	17.1	12.3	1.22	1.240	2.694	0.015	0.026
0.6	0.25	20.7	13.3	1.2045	1.236	2.694	0.022	0.041

Table 6.3: The ΔP_T calculation for the five measurements.

A total of 5 measurements have been done for these two opening cases of Table 6.2. The ΔP_T calculations for the 5 measurements are shown in Table 6.3. Q.Tan et al. [8] and Y.Jaluria [9] studied the critical pressure difference ΔP_C of air flow mode transition from unidirectional flow to bidirectional flow through a top horizontal opening, which is of order of ($g\Delta\rho L$) for a vent of height L. The ΔP_C values are shown also in Table 6.3, calculated according to ($g\Delta\rho L$), where the opening height L is 0.133m. Comparing ΔP_T and ΔP_C values, it seems that the critical pressure difference ΔP_C in these full-scale air measurements is in good agreement with ΔP_C, but ΔP_T is lower than ΔP_C as expected. If the exact critical point for change of flow mode had been found, the ΔP_C value of [8] and [9] might have been verified.

6.1.6 Air flow rate ratio at different opening ratio A_T/A_B

The air flow rate of buoyancy driven natural ventilation through two openings are measured for opening ratios A_T/A_B in the range from 0.11 to 25. The measured air flow rate is the mean value of the steady state flow. It is very important that a reliable average value must be measured for the test room during every measuring case. Figure 6.8 shows the CO_2 concentration history at the center point of the test room during the measurement case A_T=0.8m, A_B=0.2m and A_T/A_B=16 at temperature difference ΔT=11.8°C. It can be seen clearly that the steady state concentration level is reached inside the test room for the constant injection tracer gas measurement. Nevertheless, the band width of CO_2 concentration fluctuation is larger than for the case one horizontal opening, which means, the measurement uncertainty is larger than the one horizontal opening case.

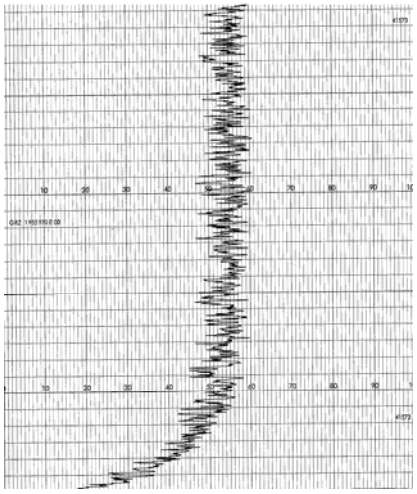

Figure 6.8: The CO_2 concentration history at the center point of the test room during the measurement case A_T=0.8m, A_B=0.2m, A_T/A_B=16 and ΔT=11.8°C. The horizontal axis records the CO_2 concentration value [ppm], and the vertical axis records the time [min].

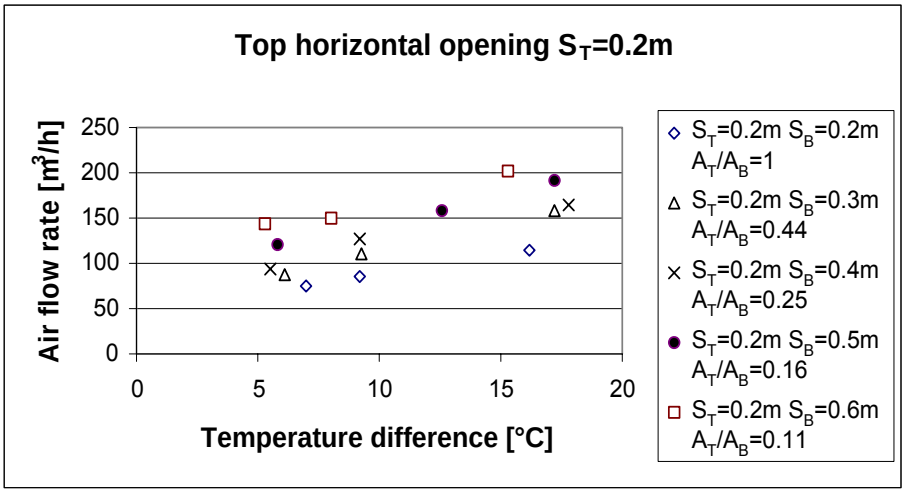

Figure 6.9: The measured air flow rate for the cases with same horizontal opening S_T=0.2m.

The measured air flow rate are shown in Figure 6.9 for the cases with same horizontal opening S_T=0.2m and different vertical opening S_B=0.2m, 0.3m, 0.4m, 0.5m and 0.6m, where the opening ratios varies from 1 to 0.11. The air flow rate increases with the temperature difference increasing for each case, because of higher buoyancy driven force. The air flow rate also changes significantly through the horizontal openings with different A_T/A_B ratio. When the opening ratio decreases from 1 to 0.11, the air flow mode changes from mode II to mode I, and the air flow through the vertical opening varies from unidirectional flow to bidirectional flow. Therefore, the bidirectional flow results in the higher air flow rate, and the lower A_T/A_B value gives rise to the higher flow rate for the same top horizontal opening. The similar situations also occur for the cases of same vertical opening S_B=0.2m and different horizontal opening S_T=0.2m, 0.4m, 0.6m, 0.8m and 1.0m, where the opening ratio varies from 1 to 25, shown in Figure 6.10. The air flow mode changes from mode II to mode III and the bidirectional flow through the horizontal opening results in the higher air flow rate. The bidirectional flow increases the air flow rate with higher A_T/A_B value.

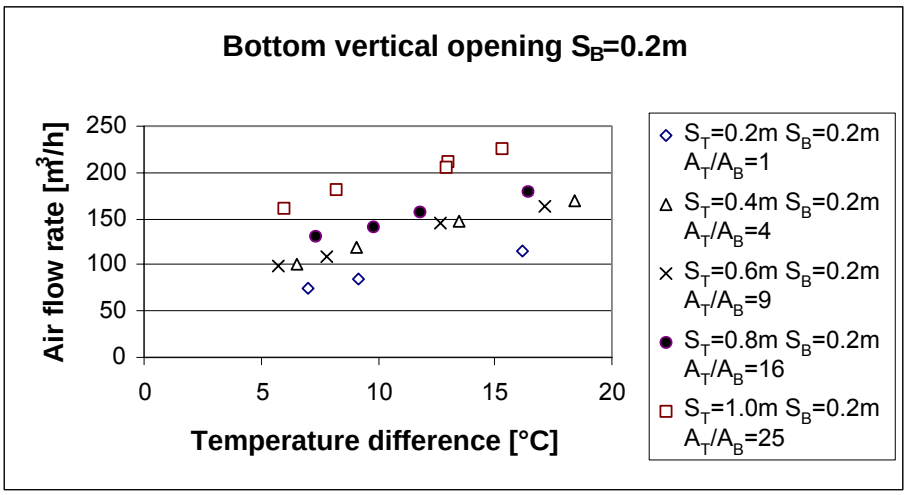

Figure 6.10: The measured air flow rate for the cases of same vertical opening S_B=0.2m.

If the two openings with different area are located at a room in two opposite ways, the calculated air flow rates are equal by the present calculation formula. However, the change of air flow rate in the two installation ways takes place, especially for the case of large area difference openings where the air flow mode belongs to mode I or mode III. It is easy to see the air flow rate change in Figure 6.9 and Figure 6.10 for the case of two opening side lengths 0.2m and 0.6m. When the S=0.2m opening is located at the top and the S=0.6m opening is located at the bottom, the air flow rate is about 175m^3/h at ΔT=10°C. In the opposite installation way, when the S=0.2m opening is located at the bottom and the S=0.6m opening is at the top, the air flow rate is about 125m^3/h at the same temperature difference ΔT=10°C. The air flow rate in mode I is higher than the mode III for these two installation ways, because the extra air flow rate of the bidirectional flow through the vertical opening is higher than it of the bidirectional flow through the horizontal opening at the same temperature difference. As to air flow mode II, the air flow rate does not change much which can be seen for openings of side lengths 0.2m and 0.4m both in Figure 6.9 and Figure 6.10.

In order to compare the measured air flow rate with the data calculated based on the present calculating formula, the dimensionless air flow rate ratio q_m/q_f is used, where q_m is the measured air flow rate and q_f is the formula calculated air flow rate. If the measured air flow rate value is close to the formula calculated value, the ratio q_m/q_f should close to 1. The flow rate with the opening A_T/A_B range from 0 to 2 and from 2 to 26 are illustrated, see Figure 6.11(A) and 6.11(B). The measured air flow rates agree well with formula calculated data in the range of $0.25<A_T/A_B<11$. Three flow

modes are included in this range where the displacement air distribution is dominant and the mixing air distribution is weak. Hence, the air flow rate can be described by the present formula. Whereas, the q_m/q_f value becomes far from 1 in the opening ratio range of $0.11<A_T/A_B<0.25$ and $11<A_T/A_B<25$. It is due to the air flow rate increase as the bidirectional flow effects increase. Thus, the larger errors will be generated by using the formula for the air flow rate calculation.

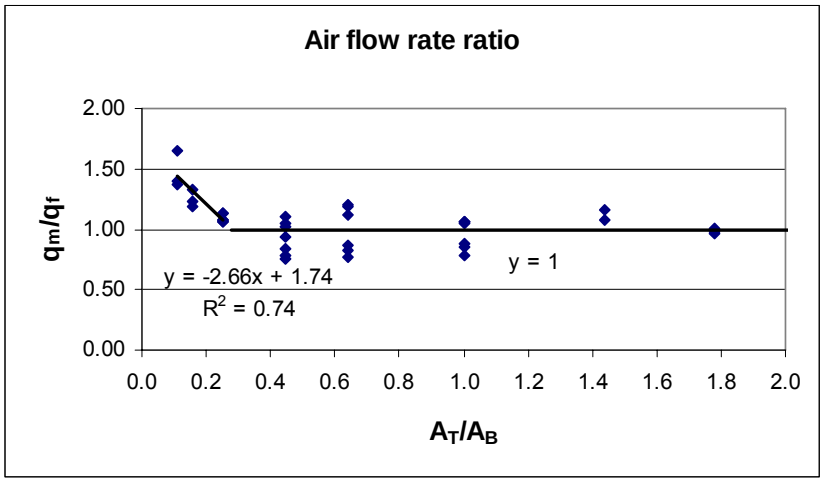

Figure 6.11(A)

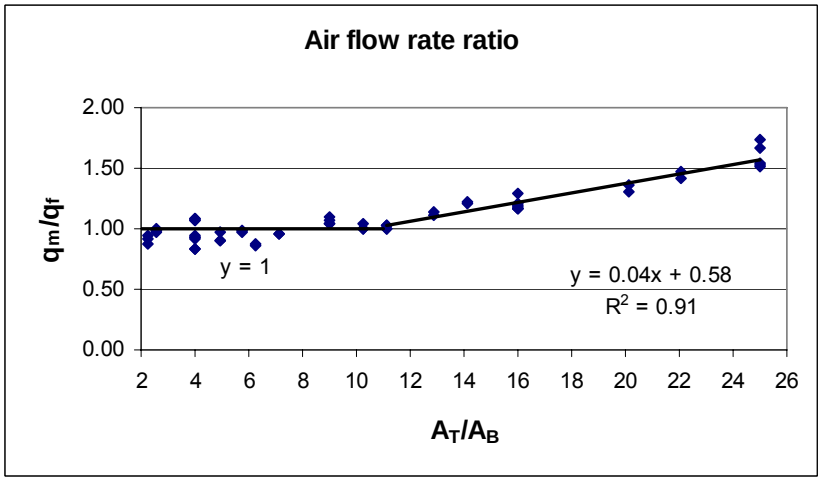

Figure 6.11(B)

Figure 6.11: The air flow rate ratio q_m/q_f versus opening ratio A_T/A_B, (A) in the range of $0<A_T/A_B<2$ and (B) in the range of $2<A_T/A_B<26$.

At some measured points such as A_T/A_B at 0.44, 0.64, 1.0 and 4, some of the measured air flow rates have large deviations compared to the formula calculated data. The errors happen probably due to the larger opening sizes. Such larger opening size and larger air flow rate will increase uncertainties during the measurements.

6.1.7 New empirical formula

According to the relationship between the air flow rate ratio q_m/q_f and the opening ratio A_T/A_B, a new empirical air flow rate calculation formula can thus be obtained. An opening area ratio factor C_A, which is a linear function of A_T/A_B, is introduced. The formula can be expressed as:

$$q = C_A C_d A^* \sqrt{\frac{2gh(T_i - T_o)}{T_o}}$$

$$A^* = \frac{A_T \cdot A_B}{\sqrt{A_T^2 + A_B^2}}$$

$$C_A = -2.66\frac{A_T}{A_B} + 1.74 \qquad 0.11 < \frac{A_T}{A_B} < 0.28$$

$$C_A = 1 \qquad 0.28 < \frac{A_T}{A_B} < 11$$

$$C_A = 0.04\frac{A_T}{A_B} + 0.58 \qquad 11 < \frac{A_T}{A_B} < 25$$

6.2 CFD results

6.2.1 Introduction

Two cases of the buoyancy driven natural ventilation through two openings are simulated, and the grid independences have been tested:

Case A: S_T=0.2m, S_B=0.2m, A_T/A_B=1
Case B: S_T=0.6m, S_B=0.2m, A_T/A_B=9

6.2.2 Case A results

Case A is typical displacement ventilation, the simulation using steady state k-ε model can converge. The calculated temperature difference between the test room and the thermostatic chamber is 9.4ºC, and the calculated air flow rate is 69.6m^3/h. Compared with the measured data 86m^3/h at the same temperature difference, the calculated value is lower than the measured value.

Figure 6.12 shows the temperature distribution contour coloured by temperature magnitude at the middle plane of the opening in X direction by steady state *k-ε* simulation. The clear temperature stratification can be seen inside the test room. Figure 6.13 shows the air flow rate history calculated by LES model and comparison with it by steady state *k-ε* model. The time step size Δt is set to be 1s for LES, because this flow pattern is quite stable. The calculated average air flow rate during the simulation flow time is 70.4m^3/h for LES model, which is little higher than calculated by the steady state *k-ε* model. Compared with the measured data, the LES model can not give much better result than the steady state *k-ε* model for this quite stable air flow case.

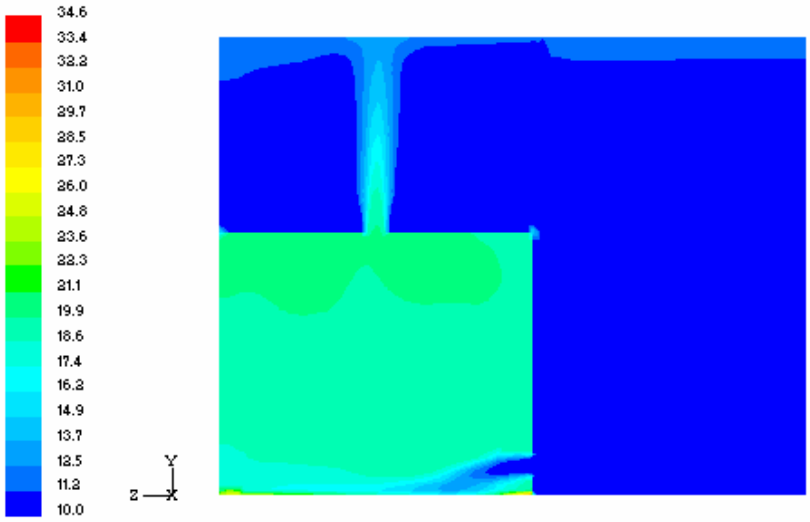

Figure 6.12: The temperature distribution contour coloured by temperature magnitude at the middle plane of the opening in X direction by steady state *k-ε* simulation.

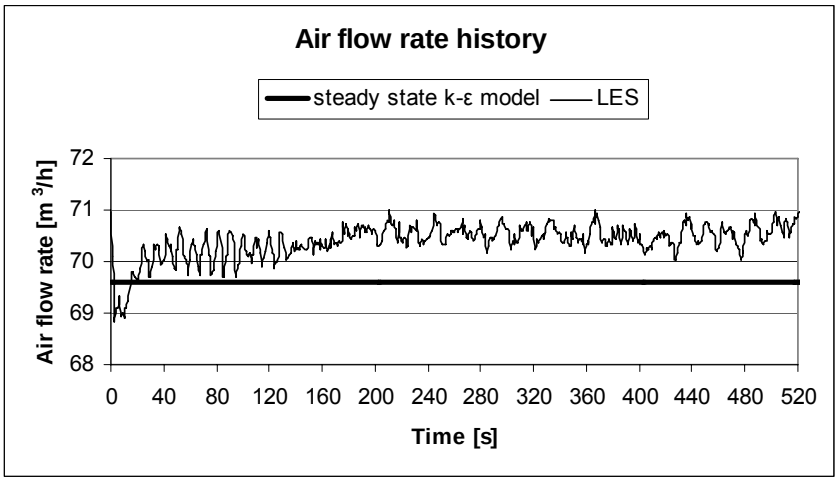

Figure 6.13: The air flow rate history for Case A calculated by LES model and comparison with the calculated data by steady state *k*-*ε* model.

6.2.3 Case B results

Observed by measurements for this case, the unidirectional flow enters into the test room through the low level vertical opening and displaces the lighter air inside the test room out through the high level horizontal opening. However some dense air also enters into the test room through the large horizontal opening from the upper thermostatic chamber. The bidirectional exchange flow across the horizontal opening is highly transient and unstable.

Although a converged steady state *k*-*ε* model solution can be obtained in this case, the outflow through the large horizontal opening is only one direction in this model, shown in Figure 6.14. The flow through the horizontal opening is still unidirectional even calculated by time-dependent *k*-*ε* model. Whereas the highly transient and unstable bidirectional flow through the horizontal opening can be obtained by using the LES model, shown in Figure 6.15. The positive Y velocity takes a most part of the opening, while the negative Y velocity takes only a very little part of the opening.

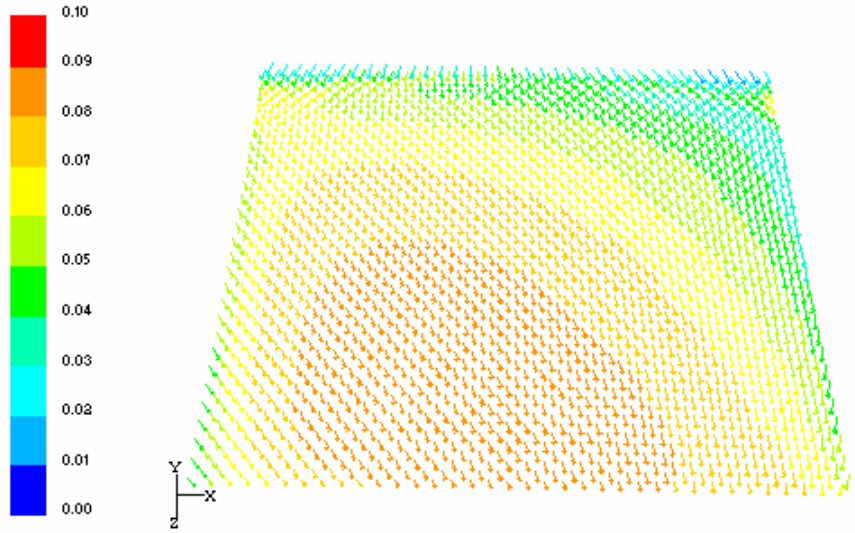

Figure 6.14: The air velocity vector distribution coloured by Y velocity at the horizontal opening calculated by steady state *k-ε* model.

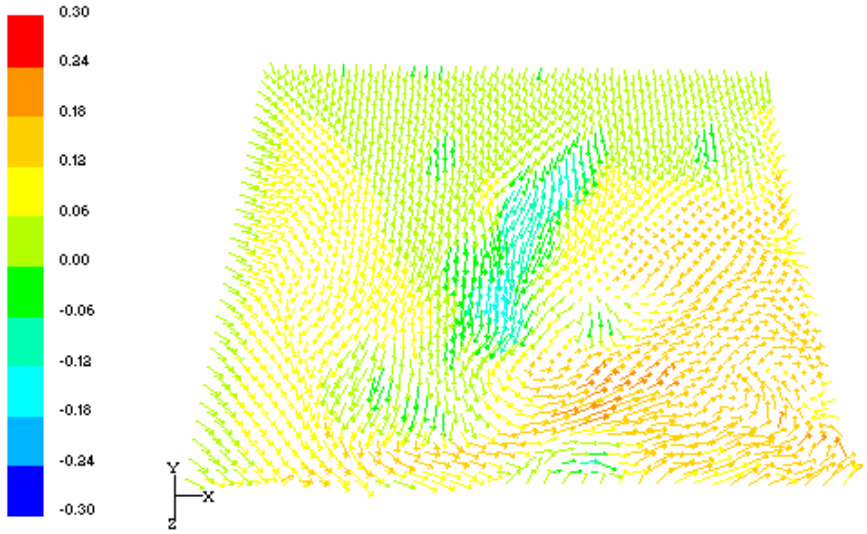

Figure 6.15(A):

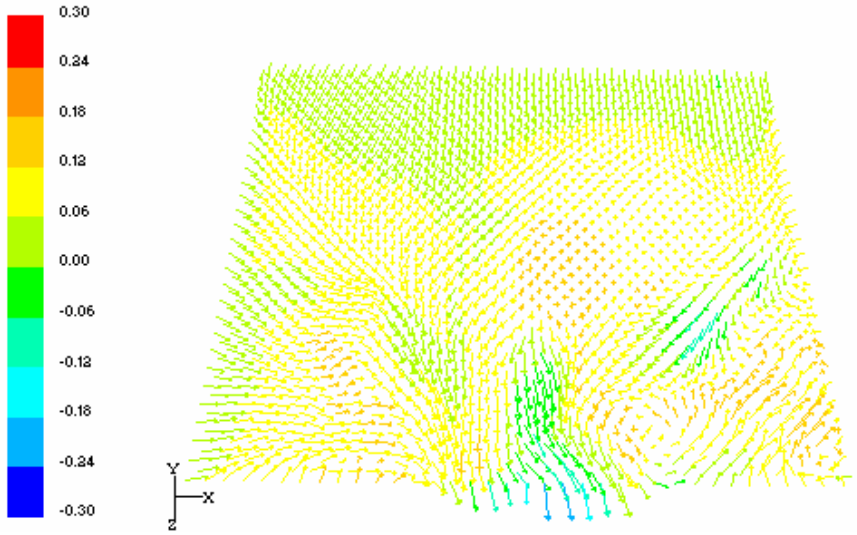

Figure 6.15(B):

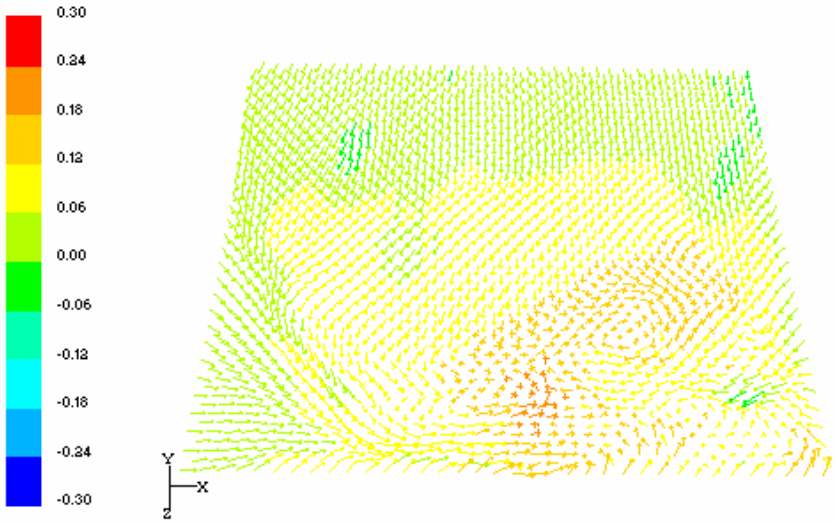

Figure 6.15(C):

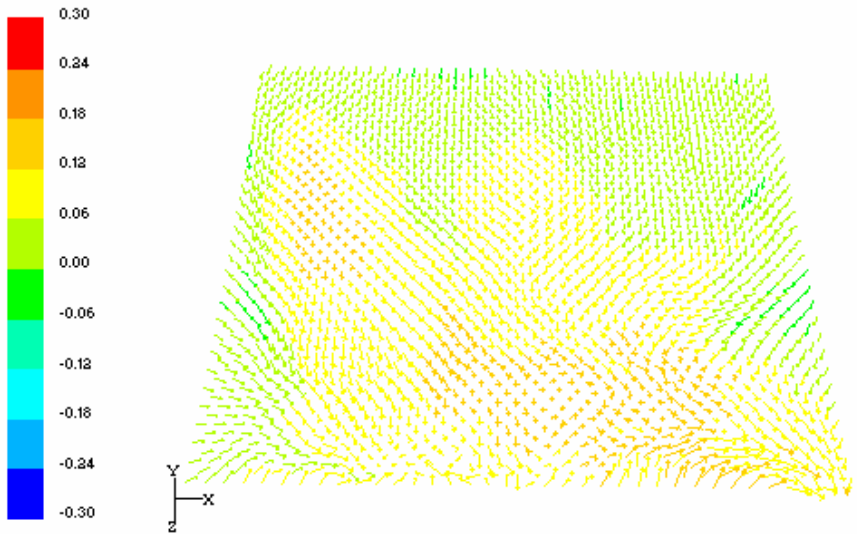

Figure 6.15(D):

Figure 6.15: The air velocity vector distribution coloured by Y velocity at the horizontal opening at four different time instants calculated by LES model, (A) 0.4s, (B) 2.4s, (C) 4.4s and (D) 6.4s.

Figure 6.16(A) and 6.16(B) show the air flow rate history calculated by time-dependent k-ε model and LES model. The time step size Δt is set to be 2s for k-ε model and 0.1s for LES. The temperature difference between the test room and the chamber is 6.1°C that keeps almost stable during the simulation. The air flow rate calculated by the steady state k-ε model is 86.1m^3/h, the average air flow rate calculated by the unsteady state k-ε model is 86.4m^3/h during the simulation time, and the average value by LES model is 92.4m^3/h. Compared with the measured air flow rate 100.5m^3/h at this temperature difference, the LES model gives a better result than the k-ε model.

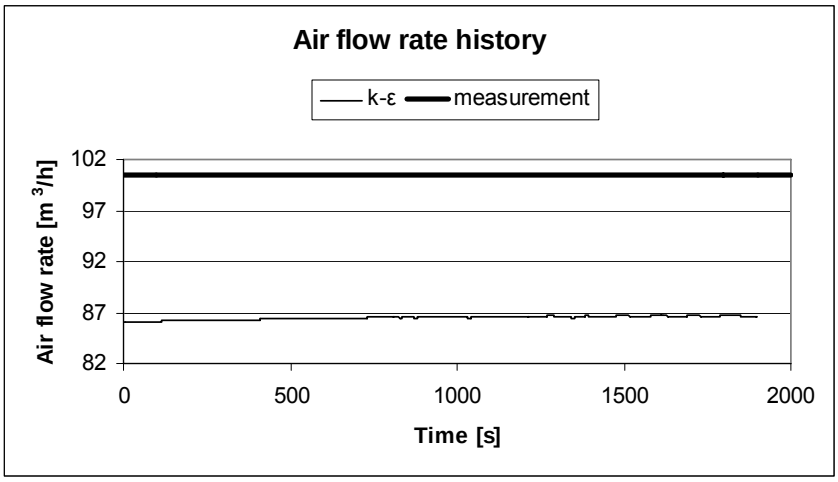

Figure 6.16(A)

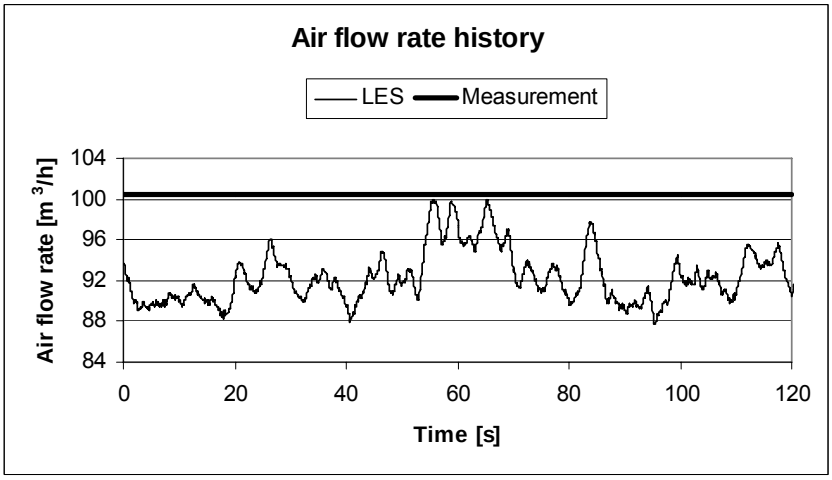

Figure 6.16(B):

Figure 6.16: The air flow rate history, (A) calculated by *k-ε* model (B) calculated by LES model.

The Y velocity histories at the center point of the horizontal opening are illustrated in Figure 6.17(A) by unsteady *k-ε* model and Figure 6.17(B) by LES model. Figure 6.16(B) and Figure 6.17(B) indicate the highly transient and unstable air flow through the horizontal opening. The Y velocity varies between positive value and negative value indicating the bidirectional flow through the horizontal opening.

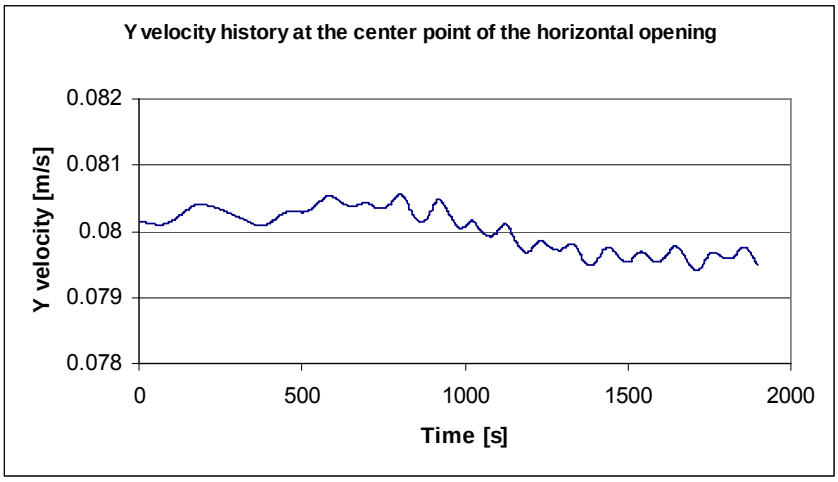

Figure 6.17(A)

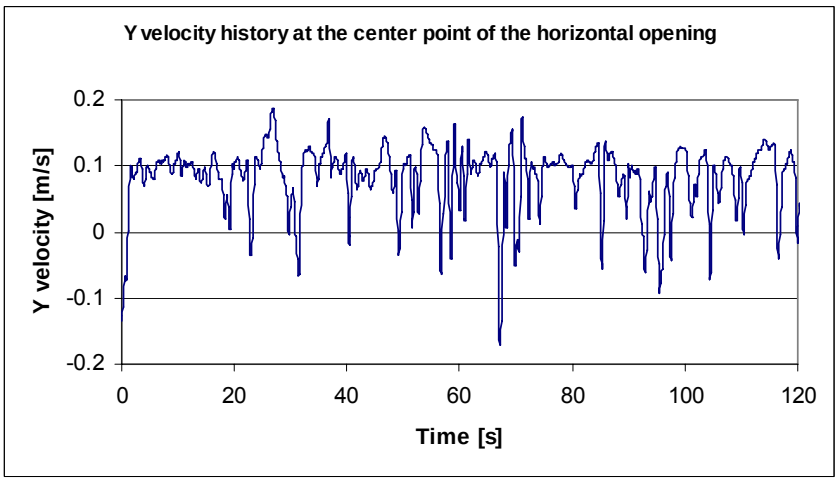

Figure 6.17(B)

Figure 6.17: The Y velocity history at the center point of the horizontal opening, (A) calculated by *k*-*ε* model, (B) calculated by LES model.

6.3 Conclusions

The experimental study indicates that three flow modes exist for one horizontal opening combined with one vertical opening. The displacement air distribution is dominant and the mixing air distribution may contribute to increase the air flow rate depending on the opening ratio value. The new empirical air flow rate calculation formula develops the present formula and the opening ratio is added as a new factor. This formula can be used for both designing a natural ventilation system and multi-zone modelling. Limitations in this study are that only the A_T/A_B range from 0.11 to 25

is investigated; and the exact critical points, where air flow model changes from unidirectional flow to bidirectional flow or the opposite way, have not been found. These issues need further more detail studies.

The air flow rate and air flow pattern of two cases are predicted by k-ε model and LES model. For a quite stable air flow condition such as the displacement ventilation, the LES model can not give much better result than the steady state k-ε model. For a highly transient air flow condition such as the bidirectional flow through a big horizontal opening, the case calculated by the LES model agrees well with the measurement; however, the case simulated by the k-ε model is not so accurate. The k-ε model simulation requires less computing time than the LES, and it can provide general airflow field distribution. The LES model seems to be a suitable tool to study highly transient natural ventilation case by providing detailed and accurate air flow information.

7 Conclusions

This Ph.D. project contains two cases of full-scale measurements and CFD simulations for buoyancy driven natural ventilation through horizontal openings: one horizontal opening, and one horizontal opening combined with one vertical opening.

Buoyancy driven natural ventilation through one horizontal opening:

1. The bidirectional flow through one horizontal opening is highly transient, unstable and complex, and the air flow rates oscillate with time. The air velocity and airflow direction vary all the time through different part of the opening
2. Due to downflow of cooled air, the temperature gradient inside the room becomes negative value at a certain height, where the position is influenced by air flow rate.
3. Correlations between the Froude number *Fr* and the opening ratio *L/D* are obtained, which is reasonable agreement with Epstein's formula derived from brine-water measurements, but the obtained *Fr* values show considerable deviations for a range of *L/D* ratios.
4. The correlations between the Archimedes number *Ar* and the opening ratio $L/\sqrt{A}$ are also determined for Epstein's formula.
5. The developed formulas are established both correlations *Fr* versus *L/D* and correlations *Ar* versus $L/\sqrt{A}$.
6. Using CFD tools, the highly transient phenomenon can not converge when simulated by a steady state *k-ε* model. The cases calculated by the LES model agree well with the measured data, however, the cases simulated by the time-dependent *k-ε* model are inaccurate compared to the measured data. For the highly transient and unstable flow of the case of buoyancy driven natural ventilation through one horizontal opening, the LES model is a suitable tool to predict detailed and accurate air flow.

Buoyancy driven natural ventilation through one horizontal opening combined with one vertical opening:

1. Three flow modes can be identified depending on the A_T/A_B value: bidirectional flow through the bottom opening of Mode I, unidirectional flow

through the two openings of Mode II and bidirectional flow through the top opening of Mode III.

2. The bidirectional flow through the horizontal opening of Mode III shows that the flow patterns are highly transient and unstable.
3. The temperature gradients of Mode I and Mode II is different with that of Mode III, because of the bidirectional air flow motion through the top opening.
4. A new empirical model for calculation of the air flow rate is developed by introducing a new opening area ratio factor.
5. For a quite stable air flow condition such as the displacement ventilation, the LES model can not give significantly better results than the steady state k-ε model.
6. For a highly transient air flow condition such as the bidirectional flow through a larger horizontal opening, the case calculated by the LES model agrees well with the measurement; however, the case simulated by the k-ε model is not so accurate.

Both buoyancy driven natural ventilation cases:

1. The research work is quite useful in relation to natural ventilation systems. The measurement results can be used in both simple calculation tools for design of a ventilation system, and can be implemented in more detailed models, especially multi-zone models, for simulation of the performance of natural ventilation systems.

References

[1] H.B.Awbi, Ventilation of Buildings, 33, ISBN 0-419-15690-9, E&FN SPON, 1991.

[2] P.Heiselberg, Natural ventilation design. International Journal of Ventilation, vol. 2, No. 4, 295-312, 2004.

[3] L. Shao and S. B. Riffat, CFD Investigation of Unstable Airflow due to Temperature Difference via Horizontal openings, Proceedings of the Second International Conference, Indoor Air Quality, Ventilation and Energy Conservation in Buildings, vol. 1, pp419-427

[4] W. G. Brown, Natural Convection through Rectangular Openings in Partitions-2: Horizontal Partitions, Int. J. Heat Mass Transfer, vol. 5, pp. 869-878, 1962

[5] A. Mercer and H. Thompson, An Experimental Investigation of Some Further Aspects of the Buoyancy-Driven Flow Between Carbon Dioxide and Air Following a Depressurization Accident in a Magnox Reactor-Part I: The Exchange Flow in Inclined Ducts, J. Br. Nucl. Energy Soc., vol. 14, pp. 327-334, 1975

[6] Cooper, L. Y., Calculation of the Flow through a Horizontal Ceiling/Floor Vent, NIST Tech. Report, Rep. No. NISTIR-89-4052, 1989

[7] M. Epstein, Buoyancy-Driven Exchange Flow Through Small Openings in Horizontal Partitions, J. Heat Transfer, vol. 110, pp. 885-893,1988

[8] Q. Tan and Y. Jaluria, Flow through a Horizontal Vent in an Enclosure Fire, HTD-Vol. 199, Heat Transfer in Fire and Combustion Systems, pp.115-122, 1992

[9] Y. Jaluria, S. H. K. Lee, G. P. Mercier and Q. Tan, Visualization of Transport across a Horizontal Vent due to Density and Pressure Differences, HTD-Vol. 252, Visualization of Heat Transfer Processes, pp. 65-81,199

[10] T. A. Conover and R. Kumar, LDV Study of Buoyant Exchange Flow through a Vertical Tube. 5th International Conference on Laser Anemometry: Advances and Applications, Veldohoven, Netherland. 1993

[11] T. A. Conover, R. Kumar and J. S. Kapat, Buoyant Pulsating Exchange Flow through a Vent. Journal of Heat Transfer Vol.117, pp. 641-648, 1995

[12] A. J. Reynolds, The scaling of flows of energy and mass through stairwells. Building and Environment 21, pp.149-153, 1986

[13] A. J. Reynolds, M. R. Mokhtarzadeh-Dehghan and A. S. Zohrabian, The modelling of stairwell flows, Building and Environment 23, pp. 63-66, 1988

[14] D. Blay and B. Gautier. Fluid Flow through a Horizontal Aperture between Two Enclosures at Different Temperatures, Roomvent'94, Cracovie, Poland, 1994

[15] D. Blay and P. Le Quéré. Fluid Flow through a Horizontal Aperture between Two Enclosures at Different Temperatures, Int. Turbulent Heat Transfer Conference, Manchester, UK, 1998

[16] D.Blay, J. L. Tuhault and S. Pinard, Heat Transfer through a Horizontal Aperture Connecting Two Non Isothermal Rooms, Roomvent'98 Vol. 2. pp 533-538, 1998

[17] C. Blonqvist and M. Sandberg, A Note on Air Movements through Horizontal Openings in Buildings, Roomvent'2002, 2002

[18] K. Klobut and K. Siren, Air Flows Measured in Large Openings in a Horizontal Partition, Building and Environment, Vol. 29. No. 3, pp. 325-335, 1994

[19] K. Klobut, Preliminary Results from Laboratory Measurements on Vertical Air Flows in a Large Horizontal opening

[20] Takeyoshi Tanaka, Experiments on Smoke Behaviour in Cavity Spaces, Fire Safety Science-Proceedings of the Fourth International Symposium, pp. 289-300

[21] Gary R. Hunt and Joanne M. Holford, The Discharge Coefficient-Experimental Measurement of a Dependence on Density Contrast, Innovations in Ventilation Technology, Proceedings 21st AIVC Annual Conference, 2000

[22] J. Halldorsson et al, Experimental and Theoretical Studies of a Solar Chimney with Uniform Heat, Roomvent'2002

[23] Andrew W. Woods, Some Theoretical Insights into Solar Driven Natural Ventilation, Roomvent'2002

[24] J. S. Kohal, S. B. Riffat and L. Shao, An Experimental and Theoretical Investigation of Airflow through Large Horizontal Openings. The Role of Ventilation, 15th AIVC Conference, Buxton, Great Britain, 1994

[25] S. B. Riffat and L. Shao, Characteristics of buoyancy-driven interzonal airflow via Horizontal Openings, Building Serv. Eng. Res. Technol. 16(3), pp. 149-152, 1995

[26] Robert E. Spall and Elgin A. Anderson, A Numerical Study of Buoyant Pulsating Exchange Flows through a Vent in a Thin Horizontal Partition, Numerical Heat Transfer, Part A, 36 pp. 263-272, 1999

[27] Linden P.F., G.F.Lane-Serff and D.A. Smeed, Emptying filling boxes: the fluid mechanics of natural ventilation, J. Fluid Mech. vol. 212, 309-335, 1990

[28] Bruce J.M., Natural ventilation by stack effect, Farm Building Progress, 32, 23-8, 1973

[29] Bruce J.M., Natural convection through openings and its application to cattle building ventilation, Journal of Agricultural Engineering Research, 23, 151-67, 1978

[30] Andersen K.T., Theory for natural ventilation by thermal buoyancy in one zone with uniform temperature, Building and Environment 38, 1281-1289, 2003

[31] Li Y., Buoyancy-driven natural ventilation in a thermally stratified one-zone building, Building and Environment 35, 207-214, 2000

[32] Heiselberg P., Natural and Hybrid Ventilation Notes, Aalborg University, 2003
[33] David Etheridge and Mats Sandberg. Building Ventilation Theory and Measurement. ISBN 0-471-96087-X, John Wiley & Sons Ltd. 1996, P598-600
[34] Joel H. Ferziger and Milovan Peric. Computational Methods for Fluid Dynamics. Springer-Verlag Berlin Heidelberg New York. 1999. ISBN 3-540-65373-2
[35] H.K.Versteeg and W.Malalasekera. An introduction to computational fluid dynamics. Longman Group Ltd. 1995. ISBN 0-582-21884-5
[36] FLUENT 6. Fluent Incorporated.
[37] Launder B.E. and Spalding D.B, The numerical computation of turbulent flow. Computer Methods in Applied Mechanics and Engineering, 3, 269-289, 1974
[38] P.V.Nielsen, The selection of turbulence models for prediction of room airflow. ASHRAE Transactions, Vol. 104, Part 1B, 1119-1127, 1998
[39] Sørensen D.N. and P.V. Nielsen, Quality control of computational fluid dynamics in indoor environments. Indoor Air, 13, 2-17, 2003
[40] Murakami S, Visualization of turbulent flowfield generated by numerical simulation. Proc. International Symposium on Refined Flow Modelling and Turbulence Measurements, University Academy Press, Tokyo, 177-188, 1988
[41] Smagorinsky J. General circulation experiments with the primitive equations. Monthly Weather Review 91, 99-165, 1963
[42] Lilly D.K. On the application of the eddy viscosity concept in the inertial subrange of turbulence. NCAR Manuscript 123, 1966
[43] Moin P. and Kim J. Numerical investigation of turbulent channel fbw. J. Fluid Mech. 118, 341-377, 1982
[44] Jones W. and Wille M. Large eddy simulation of a jet in a cross-fbw. 10^{th} Symp. on Turbulent shear flows (The Pennsylvania State University), 4:1-4:6, 1995
[45] Issa R.I., Solution of implicitly discretized fluid flow equations by operator splitting. J. Comput. Phys., 62, 40-65, 1986
[46] Nielsen P.V., S. Murakami, S. Kato, C. Topp, J.-H. Yang, Benchmark tests for a computer simulated person, ISSN 1395-7953 R0307, 2003

Scientific Publications at the Department of Civil Engineering

Technical Reports are published for timely dissemination of research results and scientific work carried out at the Department of Civil Engineering (DCE) at Aalborg University. This medium allows publication of more detailed explanations and results than typically allowed in scientific journals.

Technical Memoranda are produced to enable the preliminary dissemination of scientific work by the personnel of the DCE where such release is deemed to be appropriate. Documents of this kind may be incomplete or temporary versions of papers—or part of continuing work. This should be kept in mind when references are given to publications of this kind.

Contract Reports are produced to report scientific work carried out under contract. Publications of this kind contain confidential matter and are reserved for the sponsors and the DCE. Therefore, Contract Reports are generally not available for public circulation.

Lecture Notes contain material produced by the lecturers at the DCE for educational purposes. This may be scientific notes, lecture books, example problems or manuals for laboratory work, or computer programs developed at the DCE.

Theses are monograms or collections of papers published to report the scientific work carried out at the DCE to obtain a degree as either PhD or Doctor of Technology. The thesis is publicly available after the defence of the degree.

Latest News is published to enable rapid communication of information about scientific work carried out at the DCE. This includes the status of research projects, developments in the laboratories, information about collaborative work and recent research results.

Published 2007 by
Aalborg University
Department of Civil Engineering
Sohngaardsholmsvej 57,
DK-9000 Aalborg, Denmark

Printed in Denmark at ZZZ

ISSN 1901-7294
DCE Thesis No. 008

Recent publications in the DCE Thesis Series

ISSN 1901-7294
DCE Thesis No. 008